UNIVERSITÀ
DI PAVIA

Dipartimento di Biologia e Biotecnologie
“Lazzaro Spallanzani”

Novel Molecular Insights and New Therapeutic Strategies in Neuroendocrine Tumors

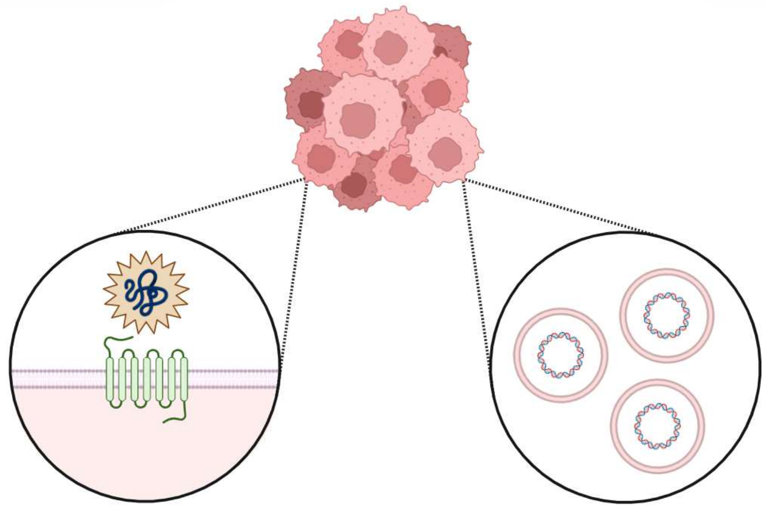

Francesco Fedeli

Dottorato di Ricerca in
Genetica, Biologia Molecolare e Cellulare
Ciclo XXXVIII – A.A. 2022-2025

Table of Contents

Abstract

Introduction: Neuroendocrine tumors (NETs) are a heterogeneous group of rare neoplasms characterized by wide variability in tissue of origin, hormone secretion, molecular features, differentiation status, and clinical behavior. Their increasing incidence and biological complexity pose significant challenges for diagnosis, prognostic stratification, and therapeutic management. A prominent feature of many NETs is the high expression of somatostatin receptors (SSTRs), which has enabled the development of targeted therapies based on somatostatin analogs (SSAs). These compounds exploit the inhibitory effects of somatostatin on hormone secretion and tumor growth; however, their clinical efficacy is often limited by the marked heterogeneity in SSTR subtype expression across different NET types and patients, highlighting the need for novel SSAs with improved receptor targeting and antitumor activity.

Beyond SSTR-dependent therapeutic challenges, specific molecular mechanisms have been associated with aggressive NET behavior. In pancreatic neuroendocrine tumors (PanNETs), inactivating mutations in the *ATRX* and *DAXX* genes are frequently linked to activation of the alternative lengthening of telomeres (ALT) pathway, a telomerase-independent mechanism of telomere maintenance. The ALT phenotype is associated with genomic instability, tumor progression, and poor clinical prognosis. The identification of reliable molecular markers of ALT activity, such as circular extrachromosomal telomeric DNA (C-circles), may therefore provide valuable tools for prognostic assessment and therapeutic stratification.

The present study addresses both the development of novel somatostatin analogs and the molecular characterization of ALT activity as complementary strategies to improve personalized treatment approaches for NET patients.

Materials and Methods: To assess the pharmacological potential of novel SSAs, five dual-target compounds (SMTR-001 to SMTR-005) were evaluated *in vitro* using pituitary (AtT-20) and pancreatic (NT-3) neuroendocrine tumor cell lines. Functional characterization was performed using both two-dimensional (2D) monolayer cultures and three-dimensional (3D) cell culture models, allowing a more physiologically relevant assessment of drug response. Cellular effects were analyzed by measuring hormone secretion, cell viability, and activation of signaling pathways downstream of somatostatin receptor engagement. Octreotide and pasireotide, both currently employed in clinical practice, were included in the study as reference compounds.

To characterize ALT activity in pancreatic NET models, two *DAXX*-mutated cell lines (NT-18P and NT-18LM) were investigated. Detection of C-circles, a highly specific molecular marker of ALT activity, was optimized using rolling circle amplification (RCA) and qPCR-based assays. In addition, ALT-positive models were treated with the cell cycle and DNA damage response inhibitors Adavosertib (WEE1 inhibitor) and Ceralasertib (ATR inhibitor) to explore their effects in the context of ALT-associated molecular features. ALT-positive SaOS-2 cells and ALT-negative human foreskin fibroblasts (HFF) were used as positive and negative controls, respectively.

Results: In AtT-20 pituitary NET cells, the novel dual SSAs modulated ACTH secretion and cell viability in a compound-dependent manner. Selected analogs (SMTR-001, SMTR-003, SMTR-004) showed more pronounced inhibitory effects, consistent with the high expression of SSTR2 and SSTR5 in this model. The observed responses were comparable to those elicited by clinically used somatostatin analogs under the same experimental conditions.

In NT-3 pancreatic insulinoma cells, the biological effects of the novel analogs differed from those observed in AtT-20 cells, reflecting differences in somatostatin receptor expression profiles between the two models. As observed in AtT-20 cells, a specific subset of compounds (SMTR-001, SMTR-002, SMTR-004, SMTR-005) effectively modulated insulin secretion and reduced cell viability.

Evaluation in both two-dimensional (2D) and three-dimensional (3D) culture systems revealed differences in responsiveness, indicating an influence of cellular spatial organization on the efficacy of SSAs.

Analysis of telomere maintenance mechanisms demonstrated the presence of ALT activity in the *DAXX*-mutated PanNET cell lines NT-18P and NT-18LM, as evidenced by detectable C-circle formation. Treatment of ALT-positive cell lines with Adavosertib and Ceralasertib proved effective, while eliciting cell line- and compound-specific differences in cellular responses. These findings support the relevance of ALT as a molecular feature of aggressive pancreatic NETs and indicate the vulnerability of ALT-positive models to targeted therapeutic interventions.

Conclusions: This study demonstrates that the newly developed dual SSAs exert significant biological effects on NET cell models and may offer improved therapeutic opportunities, particularly for tumors with complex SSTR expression patterns. Additionally, the detection of C-circles in *DAXX*-mutated PanNET lines validates ALT as a relevant biomarker of aggressive behavior. The optimized molecular approach for ALT detection provides a tool with potential translational application for stratifying PanNET patients and guiding therapeutic decisions.

Collectively, these findings support the development of novel SSAs and the implementation of ALT-targeted strategies to advance personalized medicine in NETs.

Abbreviations

- 53BP1: p53 binding protein 1
- Ab: antibody
- AC: adenylyl cyclase
- ACTH: adrenocorticotropic hormone
- ADA: Adavosertib
- AKT: protein kinase B
- ALT: alternative lengthening of telomeres
- ANOVA: analysis of variance
- APBs: ALT-associated PML bodies
- ATM: ataxia-telangiectasia mutated protein
- ATP: adenosine triphosphate
- ATR: ataxia-telangiectasia Rad3-related protein
- ATRX: α thalassemia/mental retardation syndrome X-linked chromatin remodeler
- AtT-20: anterior pituitary tumor cell line 20
- B2m: β-2 microglobulin
- BCA: bicinchoninic acid
- BFCA: bifunctional chelating agent
- BIR: break-induced replication
- BSA: bovine serum albumin
- cAMP: cyclic adenosine monophosphate
- CC assay: C-circle assay
- ccfDNA/RNA: circulating cell-free DNA/RNA
- cDNA: complementary DNA
- CER: Ceralasertib
- CHO-K1: Chinese hamster ovary-K1 cell line
- CNS: central nervous system
- Ct: cycle threshold

- D2R: dopamine receptor D2
- DAPI: 4',6-diamidino-2-phenylindole
- DAs: dopamine receptor agonists
- dATP: deoxyadenosine triphosphate
- DAXX: death-domain associated protein
- dCTP: deoxycytidine triphosphate
- ddH_2O: double-distilled water
- DDR: DNA damage response
- DEP: density-enhanced phosphatase
- DFS: disease-free survival
- dGTP: deoxyguanosine triphosphate
- DMEM: Dulbecco’s Modified Eagle Medium
- DMSO: dimethyl-sulfoxide
- dNTP: deoxynucleotide triphosphate
- DOTA: 1,4,7,10-tetraazacyclododecane-1,4,7,10-tetraacetic acid
- DPBS: Dulbecco’s phosphate-buffered saline
- dsDNA: double-stranded DNA
- DSS: disease-specific survival
- DTPA: diethylenetriaminepentaacetic acid
- DTT: dithiothreitol
- dTTP: deoxythymidine triphosphate
- ECL: enhanced chemiluminescence
- ECTRs: extrachromosomal telomeric repeats
- EDTA: ethylenediaminetetraacetic acid
- EGF: epidermal growth factor
- ELISA: enzyme-linked immunosorbent assay
- EtOH: ethanol
- FANCA: Fanconi anemia complementation group A
- FANCD2: Fanconi anemia complementation group D2
- FBS: fetal bovine serum

- Fc: fragment crystallizable region
- FDA: Food and Drug Administration
- FEN1: flap endonuclease 1
- FGF: fibroblast growth factor
- FSH: follicle-stimulating hormone
- G2 phase: gap 2 phase
- G4: G-quadruplex DNA structures
- GAPDH: glyceraldehyde 3-phosphate dehydrogenase
- GEP-NETs: gastroenteropancreatic neuroendocrine tumors
- GH: growth hormone
- GI: gastrointestinal
- GNAT3: guanine nucleotide binding protein, α transducing 3
- GPCRs: G protein-coupled receptors
- H3.3: histone variant 3.3
- HCl: hydrochloric acid
- HDR: homology-dependent repair
- HFF: human foreskin fibroblasts cell line
- HRP: horseradish peroxidase
- hTERT: human telomerase reverse transcriptase
- hTR: human telomerase RNA component
- IB: induction buffer
- IBMX: isobutyl-1-methylxanthine
- IC50: half-maximal inhibitory concentration
- IFN: interferon
- IGF-1: insulin-like growth factor 1
- IgG: immunoglobulin G
- IHC: immunohistochemistry
- IU: International Unit
- KCl: potassium chloride
- LAR: long-acting release

- LH: luteinizing hormone
- MAPK: mitogen-activated protein kinase
- MEN: multiple endocrine neoplasia
- MetOH: methanol
- $MgCl_2$: magnesium chloride
- MLL: mixed-lineage leukemia
- MMS21: methyl methanesulfonate sensitive 21 protein
- MRE11: meiotic recombination 11 homolog A
- MRN complex: MRE11-RAD50-NBS1 complex
- mRNA: messenger RNA
- mTORC1: mammalian target of rapamycin complex 1
- MUS81: MUS81 structure-specific endonuclease subunit
- MW: molecular weight
- NBS1: Nijmegen breakage syndrome 1
- NECs: neuroendocrine carcinomas
- NETs: neuroendocrine tumors
- NP-40: Nonidet P-40
- NT: non-treated
- NT-18LM: neuroendocrine tumor 18 liver metastasis cell line
- NT-18P: neuroendocrine tumor 18 primary cell line
- NT-3: neuroendocrine tumor cell line 3
- NTCs: no template controls
- OD: optical density
- P/S: penicillin-streptomycin
- PanNETs: pancreatic neuroendocrine tumors
- PBS: phosphate buffered saline
- PDGF: platelet derived growth factor
- PET: positron emission tomography
- PFS: progression-free survival
- PI3K: phosphatidylinositol-3 kinase

- PIK3CA: phosphatidylinositol-4,5-bisphosphate 3-kinase catalytic subunit α
- PitNETs: pituitary neuroendocrine tumors
- PKA: protein kinase A
- PML: promyelocytic leukemia
- pNENs: pancreatic neuroendocrine neoplasms
- POT1: protection of telomeres 1
- PRCRT: peptide receptor chemo-radionuclide therapy
- PRI: peptide receptor imaging
- PRL: prolactin
- PRRT: peptide receptor radionuclide therapy
- PTEN: phosphatase and tensin homolog
- PTPs: protein tyrosine phosphatases
- QCP buffer: quick C-circle preparation buffer
- qPCR: quantitative PCR
- RAD50: radiation sensitive 50 protein
- RAD51: radiation sensitive 51 protein
- RAD52: radiation sensitive 52 protein
- RAP1: repressor/activator protein 1
- RCA: rolling circle amplification
- RCF: relative centrifugal force
- RFU: relative fluorescence units
- RIPA buffer: radioimmunoprecipitation assay buffer
- Ro 20-1724: 4-(3-butoxy-4-methoxybenzyl) imidazolidone
- RPM: revolutions per minute
- RPMI-1640: Roswell Park Memorial Institute 1640 Medium
- RT: room temperature
- RT-qPCR: quantitative reverse transcription PCR
- S phase: synthesis phase
- SaOS-2: sarcoma osteogenic-2 cell line
- SCE: sister chromatid exchange

- SD: standard deviation
- SHPs: Src-homology 2 domain (SH2)-containing PTPs
- SMC5/6: structural maintenance of chromosomes 5/6
- SNF2: sucrose non-fermenting 2
- SPECT: single photon emission computed tomography
- SR: sustained-release
- SSAs: somatostatin analogs
- SST: somatostatin
- SSTRs: somatostatin receptors
- $t_{\frac{1}{2}}$: half-life time
- T3: triiodothyronine
- T4: thyroxine
- TAE buffer: Tris-acetate EDTA buffer
- TBP: TATA-binding protein
- TBS: Tris-buffered saline
- TBS-Tween: Tris-buffered saline – Tween 20
- t-circles: telomeric circles
- t-complex: telomeric DNA complex
- TE buffer: Tris-EDTA buffer
- TEL: telomerase
- TIFs: telomere dysfunction-induced foci
- TIN2: TRF1- and TRF2-interacting nuclear protein 2
- T-loop: telomere loop
- TMMs: telomere maintenance mechanisms
- TPP1 (ACD): adrenocortical dysplasia protein homolog
- TRF1/2: telomeric repeat-binding factor 1/2
- TSC2: tuberous sclerosis complex 2
- T-SCEs: telomeric sister chromatid exchanges
- TSH: thyroid stimulating hormone
- UV: ultraviolet

- VEGF: vascular endothelial growth factor
- VEGFRs: vascular endothelial growth factor receptors
- VIP: vasoactive intestinal peptide
- WEE1i: WEE1 inhibitor
- WHO: World Health Organization
- WST-1 assay: water-soluble tetrazolium salt 1 assay
- βFGF: basic fibroblast growth factor
- γH2AX: phosphorylated H2A histone family member X

1. Introduction

Section 1.1: Neuroendocrine Tumors, Somatostatin Receptors and Somatostatin Analogs

1.1.1 Neuroendocrine Tumors (NETs)

Neuroendocrine tumors (NETs) represent a heterogeneous group of neoplasms that arise from a wide spectrum of neuroendocrine cell populations, present in many organs of the body, that undergo tumorigenic mutational events (Rogoza et al., 2022; Cakir et al., 2010).

The worldwide incidence and prevalence of NETs are estimated to be 6/100˙000 and 35/100˙000, respectively (Durma et al., 2023). NETs are generally rare, comprising ~ 2% of all malignant tumors diagnosed in the western world (Basu et al., 2010).

Based on their histology, clinical features, rate of growth and presence of metastasis, the World Health Organization (WHO) classified NETs in three distinct categories:

- Well-Differentiated NETs (low-grade);
- Well-Differentiated (intermediate grade), which can be either benign or malignant;
- Poorly-Differentiated (high-grade), which include aggressive neuroendocrine carcinomas (NECs).

This classification (2022 WHO Classification of Endocrine and Neuroendocrine Tumors (Endocrine 5th Ed.)) is relevant in the clinical setting to define a prognosis and to choose the most appropriate therapeutic option (Kulke et al., 2012; Oronsky et al., 2017).

NETs are generally slow-growing neoplasms of epithelial origin, with variable prognosis, clinical behavior and ultimate outcome. They originate from hormonally programmed neuroendocrine precursor cells and mostly consist of well-differentiated neuroendocrine cells. NETs can arise in virtually any location of the body, but they most commonly occur in the gastrointestinal (GI) tract, pancreas, and lungs (Figure 1) (Rogoza et al., 2022; Cakir et al., 2010; Basu et al., 2010).

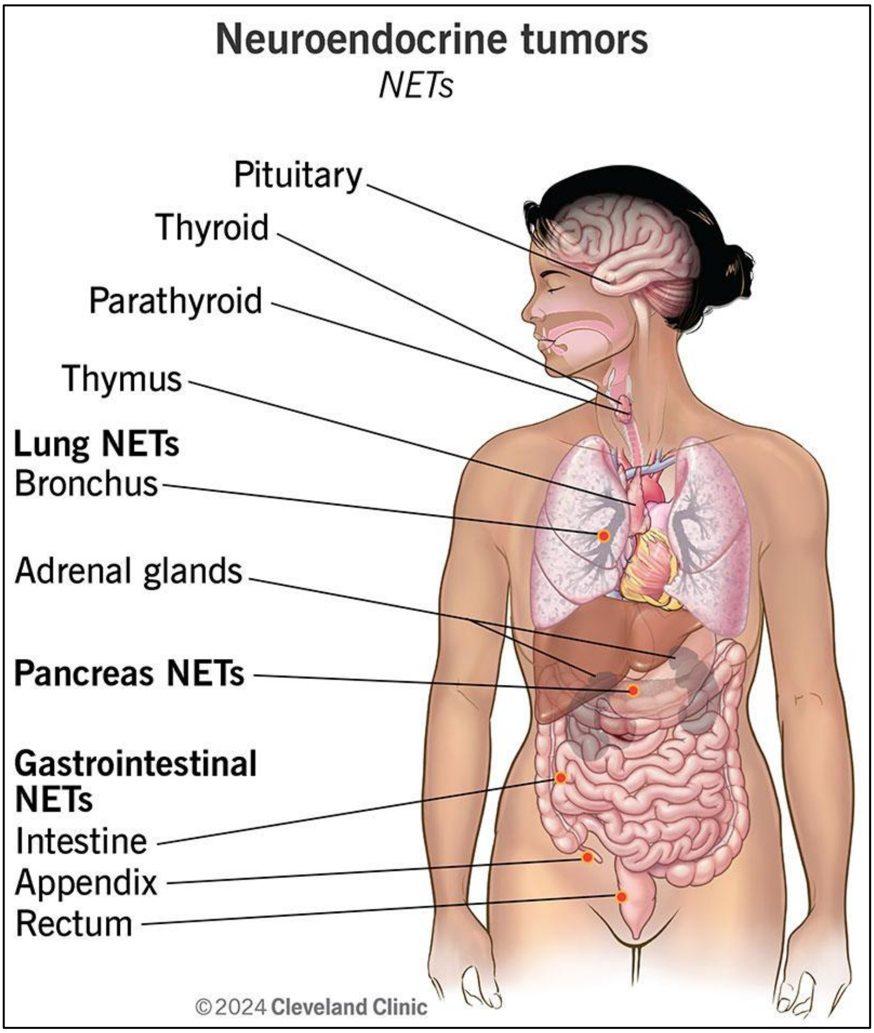

Figure 1. *Biodistribution of NETs in the human body. The most common sites are shown in bold. Reproduced from Cleveland Clinic (clevelandclinic.org). Used for academic purposes.*

Due to their cellular origins, these tumors can be subdivided in two distinct categories: non-functioning NETs and functioning NETs. Non-functioning NETs are not associated with hormone hypersecretion and related symptoms; as a result, they are often diagnosed in later stages after the occurrence of symptoms related to tumor mass effect or metastases.

Functioning NETs, on the contrary, are characterized by the active synthesis and secretion of cell-type-specific peptide hormones and neuroamines, which typically lead to elevated hormone concentrations in the circulation and to the appearance of hormonal dysregulations and characteristic clinical symptoms.

Among functioning NETs, different types of pituitary NETs are included, characterized by the active secretion of a plethora of pituitary hormones, such as ACTH (corticotropinomas), GH (somatotropinomas), and PRL (prolactinomas). Functioning pancreatic NETs are rare, but they are similarly characterized by the excessive secretion of various hormones such as insulin, gastrin, ghrelin, vasoactive intestinal peptide (VIP), glucagon, and somatostatin (SST) (Rogoza et al., 2022).

Compared with more common epithelial cancers, NETs are associated with a relatively inert behavior, but they retain a tendency to become more aggressive over time ultimately leading to death. All NETs have the potential to form metastases. Common sites of metastatic spread include lymph nodes and liver, while bone, lung and brain are typically less involved (Basu et al., 2010).

The overall survival rates for all NETs are approximately 55% and 45% at five and ten year after diagnosis, respectively (Rogoza et al., 2022). The life expectancy of patients with NETs is strictly influenced by several factors, with a worse prognosis in the case of poorly differentiated tumors or in the presence of unresectable distant metastases (Basu et al., 2010).

NETs may occur sporadically or in association with germline mutations. The most common inherited forms include the Multiple Endocrine Neoplasia (MEN) syndromes (MEN1, MEN2, MEN3 and MEN4 in human) as well as von Hippel-Lindau syndrome, neurofibromatosis type 1, and tuberous sclerosis. These hereditary conditions are typically driven by dysregulating mutations in oncogenes, proto-oncogenes, tumor suppressor genes, or genes involved in cell cycle regulation, and are characterized by the development of tumors in two or more endocrine glands following an autosomal dominant pattern of inheritance (Lee and Pellegata, 2013).

NETs are highly vascularized tumors, often exhibiting elevated expression of vascular endothelial growth factor (VEGF) and its receptor subtypes (VEGFRs), and share the expression of somatostatin receptors (SSTRs) (Rogoza et al., 2022).

1.1.2 Somatostatin (SST) and Somatostatin Receptors (SSTRs)

Somatostatin (SST) is a regulatory cyclic polypeptide hormone able to exert inhibitory effects on both exocrine (gastric acid production, pancreatic enzyme, bile and colonic fluid secretion) and endocrine (pituitary, pancreatic, and gastrointestinal hormones) hormone secretion. It is produced in various locations of the body, primarily in the gastrointestinal tract, pancreas, central nervous system (CNS), and hypothalamus (Rogoza et al., 2022; Cakir et al., 2010).

Somatostatin is synthesized from the *SST* gene, which is located on the long arm of human chromosome 3 (Shen and Rutter, 1984). Its biosynthesis leads to the generation of a preprohormone (preprosomatostatin) composed of 116 amino acids, which is cleaved into the 92 amino acid long prohormone (prosomatostatin). The precursor peptide then undergoes C-terminal post-translational processing, generating the two biologically active SST isoforms: SST-14 and amino-terminus extended SST-28 (Rogoza et al., 2022; Cakir et al., 2010).

Both SST isoforms are stored in secretory granules in the cells and, once released into the circulation, have typically a short bioactive half-life time (t½) of about 1 min. Their biological roles strongly overlap: at the cellular level, they exhibit inhibitory effects on cell survival and angiogenesis, inhibit hormone secretion, and show anti-proliferative activity on both normal and cancer cells (Rogoza et al., 2022; Cakir et al., 2010).

The biological activity of somatostatin is mediated by its binding to the corresponding receptors (somatostatin receptors or SSTRs). There are 5 different subtypes of SSTRs (SSTR1-5), each encoded by a different gene. These receptors belong to the seven transmembrane, G protein-coupled receptor (GPCR) superfamily. Two different isoforms of SSTR2 exist (SSTR2A and SSTR2B), which are produced via alternative splicing and may activate alternative signal transduction pathways. Several body tissues exhibit extensive expression of SSTRs (pituitary and hypothalamus, GI tract peripheral organs, pancreas, kidneys, thyroid, lungs, and immune cells), and similarly many tumor types.

Under physiological conditions, the effect of SST is generally determined by the types of SSTRs expressed on the surface of the target tissue cells. Generally, the activation of SSTRs results in the inhibition of the secretion of signaling molecules and hormones, such as inhibition of the release of ACTH, GH, and TSH from the pituitary gland, and the suppression of cell proliferation.

In normal tissues, the distribution and abundance of the different subtypes of SSTRs vary significantly. The most abundantly expressed receptor is SSTR2, followed by SSTR1, SSTR5 and SSTR3, whereas SSTR4 is the least expressed subtype (Figure 2).

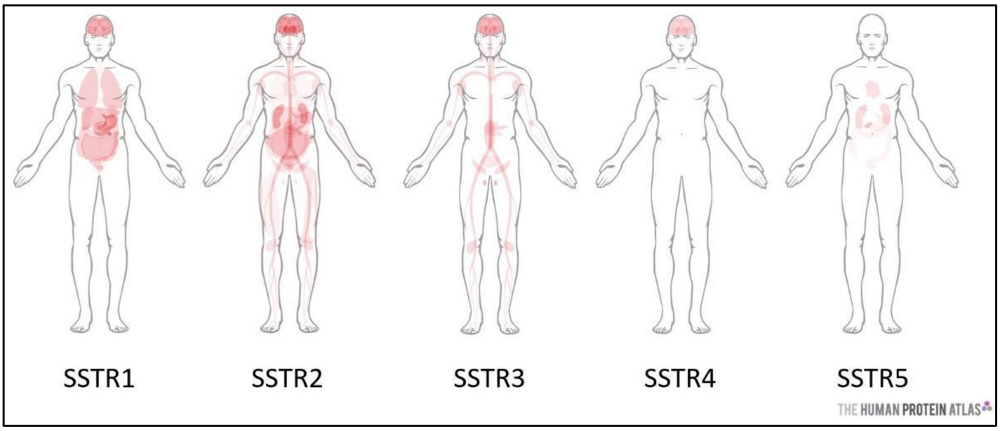

Figure 2. *Biodistribution of somatostatin receptors (SSTRs) in the human body. SSTR2 is the most expressed subtype, while SSTR4 is found only in the central nervous system (reproduced under CC BY 4.0 from Romain Eychenne et al., "Overview of Radiolabeled Somatostatin Analogs for Cancer Imaging and Therapy", 2020).*

SSTRs can form homo- and heterodimers with other SSTR subtypes, but also with dopamine receptors, opioid receptors, or epidermal growth factor (EGF) receptors, generating receptor oligomers with unique pharmacological profiles (Figure 3).

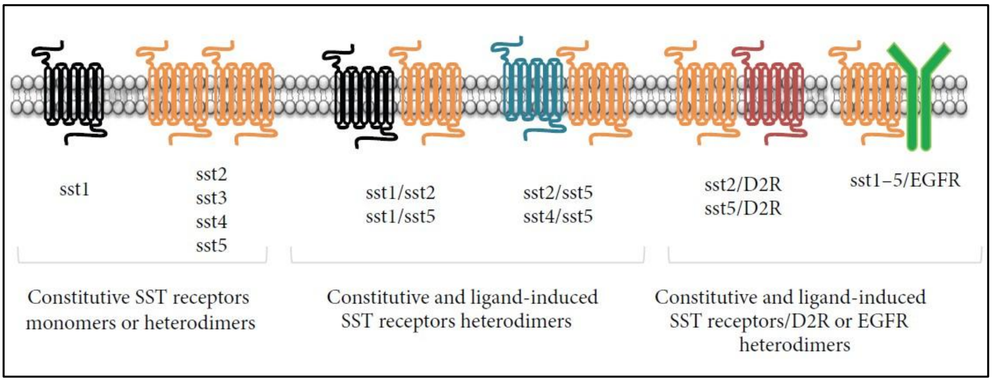

Figure 3. *Dimerization pattern of somatostatin receptors. SSTR1 exists as a monomer, while SSTR2, 3, 4, and 5 can homodimerize, both constitutively and after somatostatin binding. These receptors can also form heterodimers with other members of the SSTR family or with receptors of other GPCR (e.g., D2R) or non-GPCR families (such as tyrosine kinase receptors, like EGFR), either in resting conditions or upon ligand binding (reproduced under CC BY 3.0 from Federica Barbieri et al., "Peptide Receptor Targeting in Cancer: the Somatostatin Paradigm", 2013).*

In neuroendocrine tumors, the expression pattern of SSTRs generally resembles that of normal tissues, with SSTR2 being the most widely expressed and SSTR4 the least. However, a high degree of heterogeneity is often observed, with significant variability in the levels and expression patterns of these receptors across different tumor types and even among individuals with the same tumor type (Cakir et al., 2010; Veenstra et al., 2013).

As in normal tissues, SSTRs are predominantly localized on the surface of tumor cells. This localization, combined with their inhibitory functions, makes SSTRs both important diagnostic markers and potential targets for tailored therapeutic strategies (Rogoza et al., 2022; Cakir et al., 2010; Barbieri et al., 2013).

1.1.3 Somatostatin Signaling

Somatostatin signaling plays an important role in many regulatory circuits involved in the inhibition of tumorigenesis; therefore, shifts in SST signal transduction pathways can significantly promote the development of NETs expressing SSTRs.

SST signaling is involved in the regulation of the cell cycle by promoting the activation of protein tyrosine phosphatases (PTPs), in particular SHP-1, SHP-2, and DEP-1, which in turn upregulate the cell cycle inhibitors p21 and p27. This leads to the inhibition of the MAPK and PI3K/AKT signaling pathways, thereby decreasing cell proliferation and attenuating cell division (Figure 3).

SST controls cell growth also by the induction of apoptotic mechanisms, both directly through the engagement of pro-apoptotic (extrinsic and intrinsic) pathways, and indirectly through inhibition of proliferation and survival pathways (Figure 4).

Importantly, the binding of SST to SSTRs inhibits the activity of adenylyl cyclase (AC), determining the reduction of the cytoplasmic concentration of cAMP and following intracellular Ca^{2+}, leading to a decreased hormone secretion. This effect is also achieved through the activation of different types of K^+ channels, including delayed rectifier, inward rectifier and ATP-dependent, which induce hyperpolarization of the cell membrane and the closure of voltage-gated calcium channels (Figure 3) (Theodoropoulou and Stalla, 2013).

In addition, SST is able to regulate other hallamarks of tumorigenesis, such as angiogenesis and cell migration, by acting in particular at endothelial cell level, inhibiting monocyte activation, and blocking the release of proangiogenic factors (VEGF, PDGF, IGF-1, and βFGF) (Rogoza et al., 2022; Barbieri et al., 2013).

Generally, different SSTRs are associated with the activation of distinct downstream pathways (Figure 4). Specifically:

- Pro-apoptotic pathways are mediated by SSTR2 and SSTR3;
- Antiproliferative activity is mainly mediated by SSTR2 and SSTR5, and to a lesser extent by SSTR1;

- Inhibition of hormone secretion is mediated by SSTR2 and SSTR5, with a lesser involvement of SSTR1 and SSTR3 (Milewska-Kranc et al., 2023).

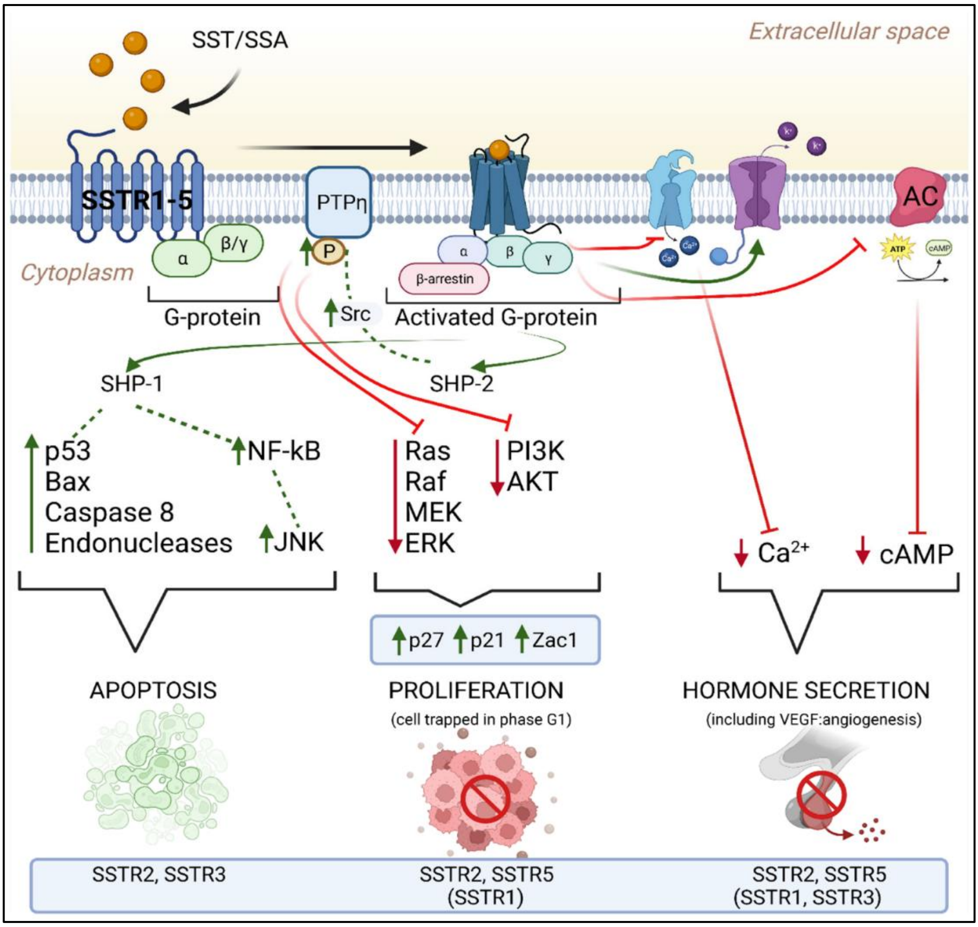

Figure 4. *Schematic representation of the downstream signaling pathways induced by somatostatin receptors activation. The binding of somatostatin to SSTRs inhibits adenylyl cyclase and leads to downregulation of intracellular* Ca^{2+}*, resulting in a decreased hormone secretion. The induction of protein tyrosine phosphatases upregulates cell cycle inhibitors leading to a decreased cell proliferation, and promotes apoptosis (reproduced under CC BY 4.0 from Agnieszka Milewska-Kranc et al., "The Role of Receptor–Ligand Interaction in Somatostatin Signaling Pathways: Implications for Neuroendocrine Tumors", 2023).*

1.1.4 Therapies for NETs

Since NETs are extremely heterogeneous tumors in terms of genetics, tissue of origin, clinical presentation, localization, differentiation, aggressiveness, and hormone secretion capability, the development of specific therapies aimed at their treatment is particularly challenging. Additionally, the low incidence of these tumors leads to a relative scarcity of research and development of clinical trials (Kunz et al., 2013). The complexity of this group of malignancies often requires the use of a multimodal approach, combining surgery, drug therapy, and radiotherapy.

Generally, the choice of the most appropriate initial and subsequent therapies is evaluated on the basis of the key characteristics of the tumor, the potential side effects of the treatment and the probability of a positive outcome (Figure 5) (Kunz, 2015).

For localized tumors, surgical resection is the first-line treatment with a curative intent. However, NETs frequently present as unresectable or metastatic (20% of cases of differentiated NETs, 50% of cases of undifferentiated NETs), and in this case the treatment selection is guided by degree of differentiation (Yao et al., 2008; Kunz, 2015).

Cytoreductive surgery is a viable option for patients with metastatic well-differentiated tumors, but in the case of symptomatic and/or progressive disease systemic therapies represent the treatment of choice. The selection of the systemic treatment is further determined by primary site, typically pancreatic versus nonpancreatic, since these subgroups of patients require different therapeutic approaches because of underlying differences in biology, response rates, and prognosis (Kunz, 2015).

The degree of tumor differentiation is another critical parameter to consider when determining the most suitable therapeutic approach.

For well-differentiated metastatic NETs, SSAs, traditionally used to manage symptoms caused by hormone hypersecretion, have recently been employed as antiproliferative agents, primarily due to their antimitotic properties that result in cell cycle arrest and inhibition of growth factors such as growth hormone, insulin-like growth factor-1, insulin, epidermal growth factor, gastrin, etc. Octreotide and lanreotide, in their long-acting release (LAR) formulations, are among the most widely used compounds in clinical practice (see Paragraph 1.1.5). Poorly differentiated neuroendocrine carcinomas typically arise in any primary anatomic site and exhibit a highly aggressive clinical behavior. First line therapy for these tumors is represented by cytotoxic chemotherapy (usually with platinum-based compounds and the topoisomerase II inhibitor etoposide). A prompt response to this chemotherapy is commonly observed in these tumors, but it tends to be short-lasting in most cases (Kunz, 2015).

Somatostatin analogues can also be administered as radiolabeled peptides in a treatment approach known as peptide receptor radionuclide therapy (PRRT) (see Paragraph 1.1.6). The PRRT approach relies on the binding of the radiolabeled analogue to its target receptor, which is then internalized by the cell. The attached radioactive isotope delivers a localized antitumor effect directly to the tumor site. This methodology has proven to be particularly effective for the treatment of SSTR-positive metastatic NETs (Kunz, 2015; Heppeler et al., 2000).

Among the latest therapeutic developments is the use of a range of biological agents. These encompass a wide array of inhibitors targeting various signaling pathways, including everolimus, an mTORC1 inhibitor, and sunitinib, a VEGF tyrosine kinase inhibitor, which administration have demonstrated prolongation of progression-free survival (PFS) in advanced pancreatic NET patients. Treatment with interferon (IFN) has also been extensively studied, both as a single agent and in combination with SSAs, but its routine use is currently limited by toxicity (Kunz, 2015).

Finally, cytotoxic chemotherapy can also be used in patients with well-differentiated pancreatic NETs characterized by large tumor burden, rapid progression, and/or significant symptoms, aiming to reduce tumor mass and improve symptom management. Chemotherapy is also administered to patients with progressive well-differentiated, nonpancreatic NETs when no other treatment options are available; however, this patient population often shows a limited objective response to therapy (Kunz, 2015).

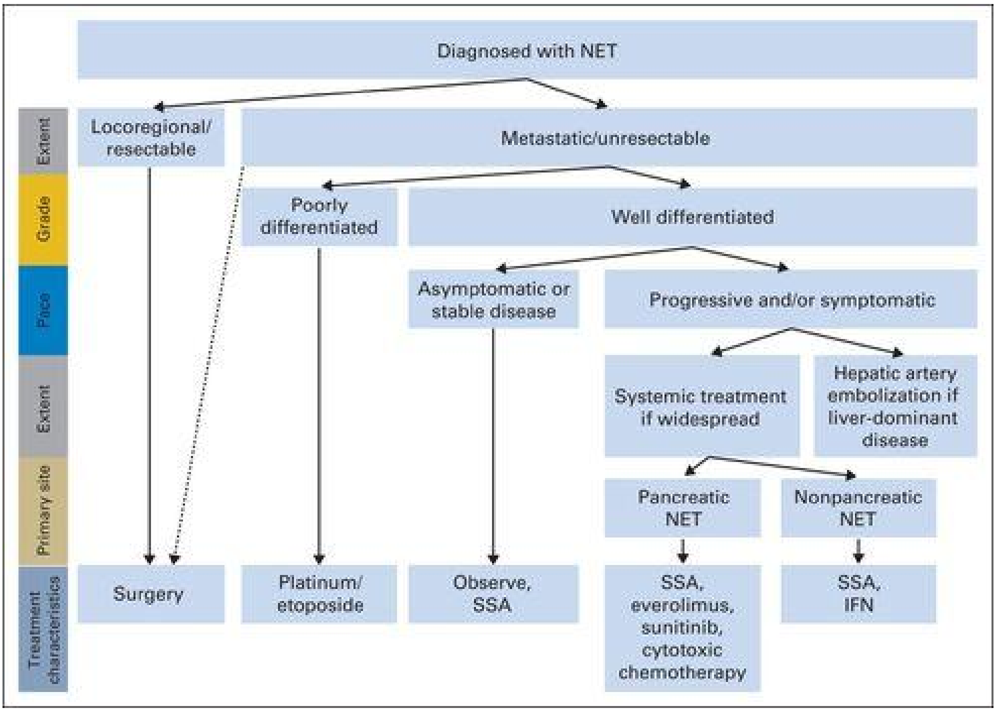

Figure 5. *Schematic representation of therapeutic approaches for tumor control in NETs. The choice of the most suitable approach depends on both tumor characteristics and treatment nature (reproduced with permission from Wolters Kluwer Health Inc.: Journal of Clinical Oncology, "Carcinoid and Neuroendocrine Tumors: Building on Success", Pamela L. Kunz, 2015).*

1.1.5 Somatostatin Analogs (SSAs) for NETs Therapy

The development of somatostatin analogs (SSAs) for cancer treatment has been encouraged by the extremely short half-life of native SST, as well as the impact of rebound hypersecretion upon SST discontinuation. Today, several clinically relevant SSAs, with longer biological half-lives, are available for therapy.

SSAs have been produced by shortening the polypeptide chain and substituting specific amino acids that are resistant to peptidase activity in the circulating serum. The first SSAs to be clinically approved constitute the "first generation" SSAs, and are:

- **Octreotide** (Sandostatin®): it was the first SSA to receive FDA approval. It is an octapeptide that reaches a half-life of 90-120 minutes after subcutaneous administration and is available in a long-acting release formulation (Sandostatin® LAR).

- **Lanreotide** (Somatuline®): it is a cyclic octapeptide with a half-life of 90 minutes. It is available also as lanreotide sustained-release (SR) that reaches a half-life of 4.5 days.

The binding characteristics of these agents are very similar: they exhibit high affinity for SSTR2, a lower affinity for SSTR3 and SSTR5, and no affinity for SSTR1 and SSTR4 (Figure 6). These analogs are currently approved for the treatment of GH-secreting pituitary adenomas.

Despite their clinical relevance, the therapeutic efficacy of these agents is strictly dependent on the expression of SSTR2 at the tumor level. The absence of expression of this receptor is often associated with resistance to the response to these peptides. This limitation prompted the development of novel, multi-receptor binding compounds (pan-SSTR agonists) with higher affinity for two or more SSTRs other than SSTR2, which are known as "second generation" SSAs. Among them the most relevant is:

- **Pasireotide** (Signifor®): it exhibits a prolonged half-life, and binds with higher affinity to SSTR1 (30-fold), SSTR3 (5-fold), and SSTR5 (39-fold), and with the same affinity to SSTR2 (3-fold) when compared with octreotide; and with higher affinity to SSTR1 (19-fold), SSTR3 (9-fold), and SSTR5 (106-fold), but with the same affinity to SSTR2 (2-fold) when compared with lanreotide (Figure 6). A long-acting release formulation (Signifor® LAR) is available.

These analogs typically exhibit good clinical effectiveness, with favorable anti-secretory and anti-proliferative actions. However, not all patients respond to the treatment with the second generation SSAs. This is probably caused by two main factors: 1) the considerable heterogeneity in the expression pattern of the different SSTRs in each tumor type and even among patients with the same tumor type; and 2) the ability of SSTRs to form homo- and heterodimers, also with other types of receptors, which may influence SSAs clinical response.

For all these reasons, further studies are needed to fully uncover the pathophysiological role of SSTR functions and to develop more efficacious and selective drugs (Rogoza et al., 2022; Cakir et al., 2010; Barbieri et al., 2013).

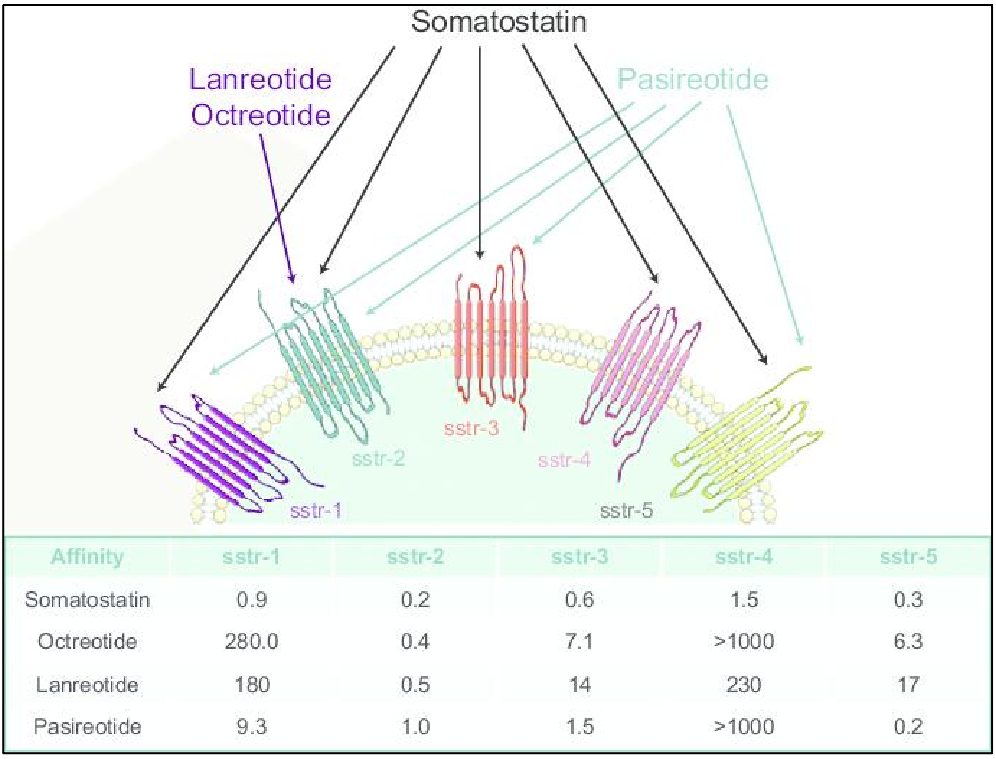

Affinity	sstr-1	sstr-2	sstr-3	sstr-4	sstr-5
Somatostatin	0.9	0.2	0.6	1.5	0.3
Octreotide	280.0	0.4	7.1	>1000	6.3
Lanreotide	180	0.5	14	230	17
Pasireotide	9.3	1.0	1.5	>1000	0.2

Figure 6. *Schematic representation of first- and second-generation somatostatin analogs that have been approved in clinical practice. Octreotide and lanreotide show high affinity to SSTR2 and lower affinity for the other SSTR subtypes. The novel, multi-receptor somatostatin analog pasireotide has the same affinity to SSTR2, but a higher affinity to SSTR1, SSTR3, and SSTR5 than both drugs (reproduced under CC BY 3.0 from Anne-Gaëlle Poullot and Nicolas Chevalier, "New options in the treatment of Cushing's disease: a focus on pasireotide", 2013).*

1.1.6 Radiolabeled SSAs

The use of radiopharmaceuticals, an approach known as nuclear medicine, has become increasingly significant in the field of oncology. It can be used for two distinct purposes: imaging, to visualize the distribution of a radioactive element within the body; and therapy, to selectively irradiate abnormal cells, thereby limiting harm to nearby healthy tissues.

Specifically, radiolabeled peptides, including those derived from SSAs, are usually based on a triple structure, involving:

- A radionuclide, whose radiation enables either the localization or the destruction of targeted cells;
- A bifunctional chelating agent (BFCA), with the role of binding the radiometal in a stable manner, to minimize its dissociation *in vivo*, and conjugate it to the target moiety;
- A targeting moiety – in this case, the peptide analog – that conveys this set in a specific way to a well-defined target.

To reduce the influence of the chelating group, a linker (or spacer) is typically inserted between the BFCA and the biomolecule (Figure 7). The choice of the radionuclide is essential, as it significantly affects the design of the chelating structure. This choice is based on several criteria, including the nature of the radiation emitted, the half-life, the isotope decay profile, and the means of production. The primary objective is to enable the compound's diagnostic or therapeutic use while minimizing harm to the body from excessive radiation exposure or harmful decay byproducts.

Numerous SSAs have already been labeled with various radioisotopes, either for imaging – using probes currently applied in clinical practice – or for therapeutic purposes, with many compounds undergoing clinical evaluation (Eychenne et al., 2020). Peptide receptor imaging (PRI) and radionuclide therapy (PRRT) can be merged into a single probe, known as a "theranostic" tool (de Jong et al., 2009).

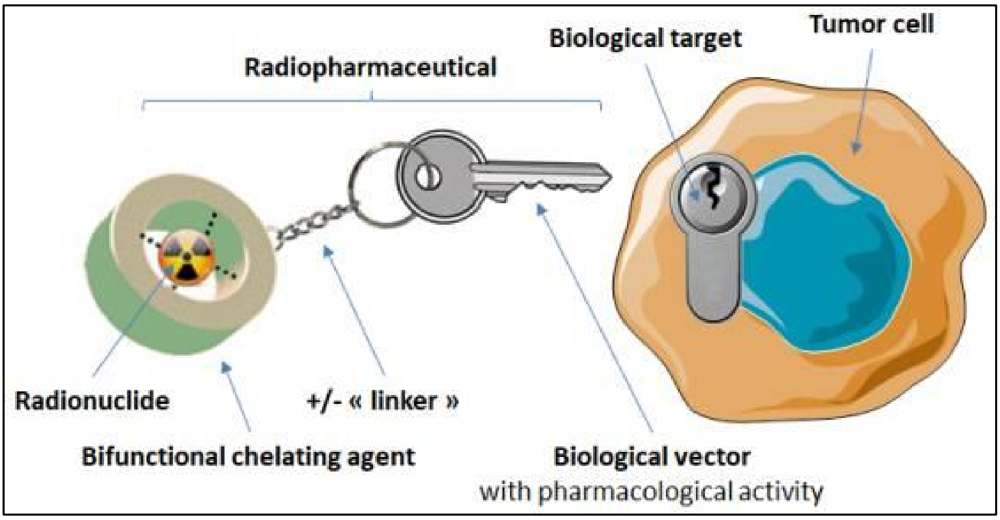

Figure 7. Schematic representation of the structure of a radiopharmaceutical. The biological vector, such as a somatostatin analogue, is conjugated to a radionuclide via a bifunctional chelating agent that promotes stability. The targeting moiety binds to its molecular target and delivers the radiometal into the target cell, enabling its use for diagnostic and/or therapeutic purposes (reproduced under CC BY 4.0 from Romain Eychenne et al., "Overview of Radiolabeled Somatostatin Analogs for Cancer Imaging and Therapy", 2020).

Radiolabeled SSAs for Diagnostics Imaging

Diagnostic SST radioisotopes enable the localization of tissues expressing SST receptors and help identify patients who may benefit from subsequent radionuclide therapy. For imaging, radiolabeling is performed using isotopes that emit highly penetrating but low-ionizing radiation, which helps minimize damage to surrounding tissues (Eychenne et al., 2020).

The first compound that was used for imaging tumors expressing SSTRs was [^{123}I-Tyr^{3}]-octreotide, resulting from an electrophilic iodination reaction of tyrosine. Although the compound showed biological activity and receptor affinity similar to that of native somatostatin, its application was limited by several factors, including the difficulty of the radiolabeling procedure, the high costs, and the hepatic clearance mechanism – which was problematic when interpreting the obtained images (Bakker et al., 1991).

These critical issues were overcome following the replacement of iodine-123 with indium-111, coupled with octreotide via the chelating agent DTPA (diethylenetriaminepentaacetic acid). This compound, named [^{111}In-DTPA^{0}]-

octreotide ([^{111}In]-pentetreotide), allowed *in vivo* imaging of SSTR-expressing tumors and associated metastases, as well as showing rapid clearance through the kidneys (Bakker et al., 1991). Due to its effectiveness, it became the first radiopharmaceutical approved by the FDA, marketed under the name Octreoscan®, and it has long been considered the "gold standard" for the visualization of neuroendocrine tumors.

However, since [^{111}In-DTPA^0]-octreotide still has limitations in its use (requires a high tumor/noise intensity ratio, shows low spatial resolution, has a moderate affinity for receptors, exposes the patient to high radioactivity), research in the field of radiopharmaceuticals has increasingly focused on alternative radioelements, such as technetium-99m for single photon emission computed tomography (SPECT) imaging and gallium-68 for positron emission tomography (PET) scans.

Currently, another chelating agent, DOTA (1,4,7,10-tetraazacyclododecane-1,4,7,10-tetraacetic acid), is extensively used for the synthesis of radiolabeled analogues due to its ability to confer greater binding affinity for SSTRs. This chelating agent has been utilized to develop new radiolabeled analogues, such as[^{111}In-DOTA-Tyr^3]-octreotide ([^{111}In]-DOTATOC) and [^{111}In-DOTA-Tyr^3]-octreotate ([^{111}In]-DOTATATE), which exhibit similar pharmacokinetic profiles and, notably, a high affinity for SSTR2 and SSTR5 – receptors that are frequently overexpressed in tumors. By contrast, the compound [^{111}In-DOTA-1-NaI^3]-octreotide (DOTANOC) was synthesized with the aim of obtaining a probe capable of binding all SSTR subtypes; it shows a higher affinity towards SSTR3, resulting in a higher rate of internalization and biodistribution, leading to a greater accumulation of the probe in the tumor (Forrer et al., 2004; Wild et al., 2003; Virgolini et al., 2001).

Radiolabeled SSAs for Therapy

In the context of PRRT, radioactivity is used with the aim of destroying target cells. While the structure of radiopharmaceuticals remains unchanged compared to those used in imaging, the nature of the associated radionuclide is modified, favoring in this case elements with less penetrating and more energetic radiation – and therefore, more ionizing. When these compounds are directly delivered to the cancer cell, radiation emitted by radioactive decay causes irreversible DNA ionization, leading to cell apoptosis.

Even in the context of therapeutic application, analogues conjugated with DOTA (DOTA-SSAs) are the most commonly used, while the selection of radioelements typically includes iodine-131, yttrium-90, lutetium-177, and, less often, rhenium-188, being strong emitters of β^- radiation (Uccelli et al., 2019).

[^{90}Y]-DOTATOC (Octreother®) was the first analogue to be investigated, demonstrating favorable efficacy and tolerability, with limited side effects. However, it also exhibited some toxicity to the kidneys and bones, with these two factors representing the main dose-limiting concerns for the patient (Otte et al., 1999).

Another relevant compound, [^{90}Y]-DOTATATE, has shown positive results, with a higher affinity for SSTR2 compared to [^{90}Y]-DOTATOC.

Compounds of the same analogues labeled with lutetium-177 were later developed. [^{177}Lu]-DOTATOC has shown positive results when used in case of relapse of neuroendocrine tumors, but [^{177}Lu]-DOTATATE (Lutathera®) proved to be more promising as it showed a longer retention time in tumor tissue (Bodei et al., 2012). No cases of nephrotoxicity have been reported following the administration of these radiopharmaceuticals (Eychenne et al., 2020).

Recent studies have also indicated that SSTR antagonists can be as effective as agonists, even without internalization of the ligand-receptor complex. The strong tumor uptake of the compound, leading to prolonged radiation retention, appears to be caused by the receptors possessing a greater number of binding sites for antagonists compared to agonists, as well as by a slower rate of dissociation. Studies investigating the use of antagonists labeled with DOTA and either indium-111 or lutetium-177 have yielded promising results in terms of efficacy (Freda et al., 2005; Cescato et al., 2006).

To enhance radiation-induced damage to tumor cells and improve their killing, various radiosensitizers can be administered alongside PRRT. The most extensively studied approach to achieve this outcome is the combination of PRRT with chemotherapy, known as peptide receptor chemo-radionuclide therapy (PRCRT). Studies employing this approach have demonstrated a favorable safety profile and manageable toxicity (Ambrosini et al., 2022).

1.1.7 Pancreatic NETs: Characteristics, SSTR Expression Patterns and Therapeutic Approaches

The gastroenteropancreatic tract, along with the lungs, is one of the main sites of origin for neuroendocrine tumors. Pancreatic neuroendocrine neoplasms (pNENs, or PanNETs) represent a subtype of gastroenteropancreatic neuroendocrine tumors (GEP-NETs) and are differentiated from carcinoid tumors based on their primary site of origin. Although the incidence of PanNETs has been increasing over the past four decades, these tumors remain relatively rare, accounting for only 1%–2% of all pancreatic malignancies. According to the WHO classification, GEP-NETs are categorized into grade 1 (NET G1), grade 2 (NET G2), and neuroendocrine carcinoma (NEC) based on the Ki-67 proliferation index and mitotic count (Ohmoto et al., 2017).

As with other types of NETs, PanNETs can be classified as either functioning or non-functioning, depending on their ability to secrete hormones that produce distinct clinical symptoms. Most of them (60% to 90%) are non-functioning and largely asymptomatic. Functioning tumors, on the other hand, are defined by the secretion of various hormones depending on the cell type of origin. These hormones may include insulin, gastrin, vasoactive intestinal peptide (VIP), glucagon, somatostatin, and serotonin (Ma et al., 2020).

Five primary subtypes of PanNETs are identified based on their originating cell population (Figure 8) and their distinct secretory profiles:

- Insulinomas: originate from pancreatic β cells and secrete large amounts of insulin; commonly associated with hypoglycemia and hypokalemia (Wolf et al., 2015);
- Gastrinomas: characterized by acid hypersecretion and associated with peptic ulcer disease and Zollinger-Ellison syndrome (Yang and Chu, 2015);
- Glucagonomas: originate from pancreatic α cells and secrete high levels of glucagon; often associated with symptoms such as diabetes mellitus, anemia, and venous thrombosis, and show a high tendency to metastasize (Castro et al., 2011);
- Somatostatinomas: arise from pancreatic δ cells and produce excessive amounts of somatostatin; commonly linked to the suppression of pancreatic, biliary, gastric, and intestinal secretions (Soga and Yakuwa, 1999);
- VIPomas: secrete high levels of vasoactive intestinal peptide (VIP) and are associated with syndromes characterized by hypokalemia and achlorhydria or hypochlorhydria (Krejs, 1987).

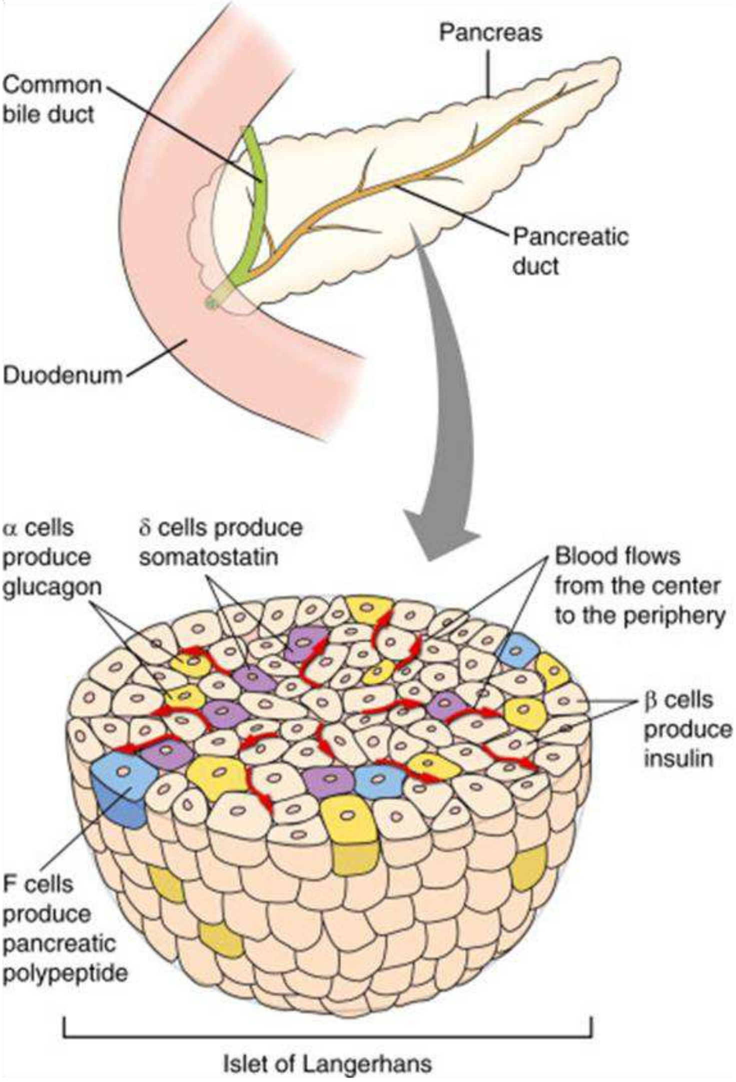

Figure 8. *Pancreas anatomy. The islets of Langerhans contain distinct cell populations from which PanNETs originate: insulinomas arise from β cells, glucagonomas from α cells, and somatostatinomas from δ cells (reproduced and adapted with permission from Elsevier: Elsevier Books, "Goodman's Basic Medical Endocrinology", 203-237, Elizabeth H. Holt et al., 2022).*

One of the key genetic characteristics of PanNETs is the high occurrence of somatic inactivating mutations in the *MEN1* gene (~ 44% of cases), a tumor suppressor linked to multiple endocrine neoplasia (MEN) type 1 syndrome. The menin protein produced by this gene is part of the MLL/SET1 histone methyltransferase complex and plays a crucial role in regulating gene transcription through chromatin remodeling.

Somatic inactivating mutations in the *ATRX* (α thalassemia/mental retardation syndrome X-linked) and *DAXX* (death-domain associated protein) genes are also frequently observed (~ 43% of cases). These mutations are typically mutually exclusive within the same tumor, suggesting that the proteins they encode function within the same biological pathway. Both proteins are closely involved in telomeric chromatin remodeling and exert their effects through direct interaction with each other. The inactivation of *ATRX* or *DAXX* is strongly associated with the telomerase-independent telomere maintenance mechanism known as alternative lengthening of telomeres (ALT) (see Paragraph 1.2.1).

Lastly, somatic mutations affecting the mammalian target of rapamycin (mTOR) signaling pathway are also common (~ 18% of cases). These often include inactivating mutations in the *PTEN* (phosphatase and tensin homolog) and *TSC2* (tuberous sclerosis complex 2) genes, as well as oncogenic mutations in the *PIK3CA* (phosphatidylinositol-4,5-bisphosphate 3-kinase catalytic subunit α) gene (Ohmoto et al., 2017; Jiao et al., 2011).

SSTR Expression in Pancreatic NETs (PanNETs)

PanNETs display high expression of SSTRs, with a general predominance of SSTR2 and SSTR5, while SSTR1, SSTR3, and SSTR4 are present at lower levels (Barbieri et al., 2013). However, receptor subtype expression profiles can differ significantly depending on the specific type of pancreatic NET under evaluation. Consequently, the most effective therapeutic strategy must be individually tailored to each case.

SSAs have been recommended for the treatment of functioning PanNETs (Cakir et al., 2010). Specifically:

- Insulinomas exhibit a heterogeneous expression of SSTRs. SSAs are considered a second-line treatment for managing hypoglycemia, particularly in cases of malignant insulinomas. Octreotide is commonly used, while pasireotide may be employed in tumors resistant to other therapies. However, in insulinomas lacking SSTR expression, SSAs may exacerbate hypoglycemia by inhibiting counter-regulatory hormones such as glucagon and growth hormone (GH).
- Gastrinomas are characterized by elevated SSTR2 expression. Treatment with long-acting somatostatin analogs, such as octreotide LAR and lanreotide, is frequently employed to inhibit gastrin release and control tumor growth.

- Glucagonomas also typically exhibit high levels of SSTR2 expression. Treatment with octreotide and lanreotide has been shown to provide rapid symptom relief, particularly for diarrhea and necrolytic migratory erythema; however, these therapies are generally ineffective at significantly lowering serum glucagon levels. In cases where first-generation SSAs are ineffective, pasireotide has been proposed as a potential therapeutic alternative.
- Somatostatinomas typically express high levels of SSTR5. While it may seem counterintuitive to treat a somatostatin-secreting tumor with somatostatin analogs, octreotide has been shown to alleviate associated symptoms and lower circulating somatostatin levels.
- In cases of VIPomas, adjuvant treatment with octreotide has proven effective in managing diarrhea and lowering serum VIP levels (Gomes-Porras et al., 2020).

In addition, a promising and increasingly explored therapeutic strategy is the combination of octreotide or pasireotide with everolimus, an mTOR inhibitor that plays a key role in regulating cell growth and survival (Barbieri et al. 2013).

1.1.8 Pituitary NETs: Characteristics, SSTR Expression Patterns and Therapeutic Approaches

Pituitary neuroendocrine tumors (PitNETs) are the second most prevalent brain tumors, accounting for approximately 10-15% of surgically treated primary tumors of the central nervous system. Most of these are benign and tend to grow slowly, but the progressive increase in mass and hormonal hypersecretion can lead to serious health conditions such as Cushing’s disease and acromegaly (Ezzat et al., 2004; Solari et al., 2019).

PitNETs are classified based on their size and/or hormonal activity. Tumors measuring less than 10 mm in diameter are termed microadenomas, those measuring 10 mm or more are called macroadenomas, and lesions reaching 40 mm or larger are designated as giant adenomas (Solari et al., 2019).

PitNETs can also be categorized as either hormone-secreting (functioning) or non-secreting (non-functioning) tumors. Functioning pituitary neuroendocrine tumors are characterized by autonomous hormone secretion, reflecting the differentiation of the neoplastic cells toward specific adenohypophyseal lineages (Solari et al., 2019). Based on their hormonal profile and cell population of origins (Figure 9), these tumors include:

- Corticotropinomas: arise from pituitary corticotroph cells and are responsible for the development of Cushing’s disease. They are characterized by excessive secretion of adrenocorticotropic hormone (ACTH), which stimulates the adrenal glands to release large amounts of glucocorticoids, primarily cortisol. Corticotropinomas are often associated with clinical complications such as diabetes, obesity, hypertension, weight gain, and neurocognitive disorders (Bertagna et al., 2019; Araya et al., 2022; Lonserr et al., 2017);

- Somatotropinomas: develop from pituitary somatotroph cells and may be associated with pathological conditions such as acromegaly. They are characterized by excessive secretion of growth hormone (GH) and are often linked to cardiovascular, respiratory, musculoskeletal, and neurological complications (Fleseriu et al., 2022; Melmed, 2009);
- Prolactinomas: originate from lactotroph cells of the anterior pituitary. They are associated with elevated prolactin production, which typically correlates with tumor size. Large tumors may cause symptoms such as visual disturbances and cranial nerve palsies (Wildemberg et al., 2021);
- Thyrotropinomas: originate from pituitary thyrotroph cells and are characterized by excessive secretion of thyroid-stimulating hormone (TSH), which in turn leads to uncontrolled production of thyroid hormones (T3 and T4). They are associated with typical hyperthyroidism symptoms such as weight loss, tachycardia, muscle weakness, and gastrointestinal disturbances (Beck-Peccoz et al., 2019);
- Gonadotropinomas: develop from gonadotroph cells of the anterior pituitary. The majority (80–90%) are non-functioning; functioning tumors secrete elevated levels of gonadotropins (FSH and LH) and are typically associated with symptoms such as ovarian hyperstimulation and macroorchidism (Chaidarun and Klibanski, 2002).
- Non-functioning pituitary adenomas: typically originate from gonadotroph cells and cause symptoms related to tumor mass, without hormonal hypersecretion. The most common symptoms include visual disturbances, headaches, and cranial nerve dysfunction (Greenman and Stern, 2009).

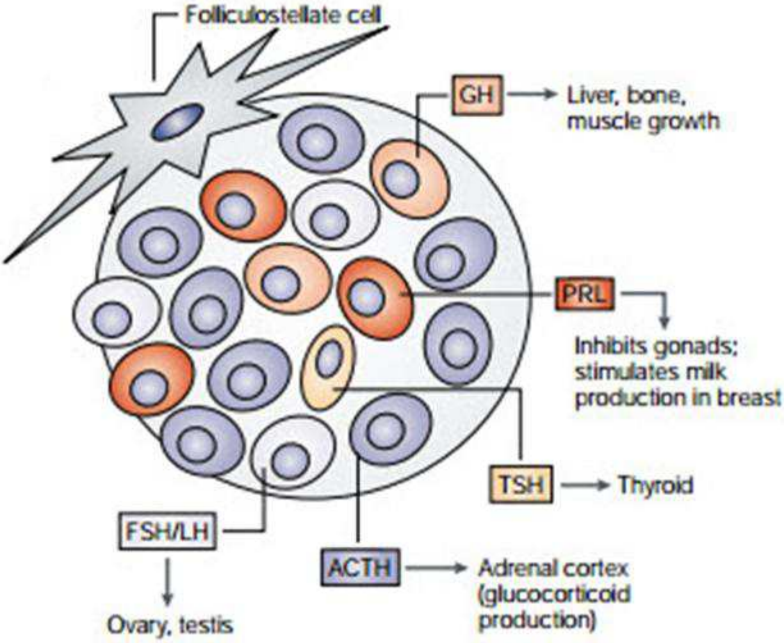

Figure 9. *Characteristics of pituitary cells. Different cell populations secrete different hormones and are associated with the development of adenomas with distinct features: corticotropinomas arise from ACTH-secreting cells, somatotropinomas from GH-secreting cells, prolactinomas from PRL-secreting cells, thyrotropinomas from TSH-secreting cells, and gonadotropinomas from FSH/LH-secreting cells (reproduced and adapted with permission from Springer Nature: Nature Reviews Cancer, "The pathogenesis of pituitary tumors", Sylvia L. Asa and Shereen Ezzat, 2002).*

SSTR expression in pituitary NETs (PitNETs)

Similar to PanNETs, PitNETs also exhibit a highly heterogeneous pattern of SSTR expression. SSTR2 is generally the most commonly expressed receptor subtype in PitNETs; however, the expression profiles of all SSTR subtypes can vary significantly depending on the specific type of pituitary NET. Consequently, also in

this case the most effective therapeutic strategy must be tailored to each individual case.
Specifically:

- In corticotropinomas (ACTH-secreting) adenomas (corticotropiomas), there is a high expression of SSTR5 and D2R, whereas SSTR2, SSTR1, and SSTR3 are expressed at lower levels. Octreotide is not particularly effective in reducing ACTH and serum cortisol levels, while pasireotide is a more promising alternative for the treatment of this kind of tumors.
- In most GH-secreting adenomas (somatotropinomas), SSTR2, SSTR5, and D2R have been found to be coexpressed at both mRNA and protein levels. SSTR3 and SSTR1 coexpression was also found in mixed GH/PRL adenomas. Octreotide represents the standard of care, while pasireotide is typically used in resistant cases due to selective loss of SSTR2 expression.
- The majority of PRL-secreting adenomas (prolactinomas) express high levels of D2R and SSTR1, and lower levels of SSTR5 and SSTR2. Dopamine receptor agonists (DAs) have been successfully used in these tumors, along with SSTR5 agonist treatment in resistant cases.
- TSH-secreting tumors (thyrotropinomas) are very rare, but significantly express SSTR1, SSTR2 and SSTR5. Octreotide showed good efficacy in reducing circulating TSH levels and in achieving significant tumor shrinkage.
- Gonadotropinomas primarily express SSTR2 and SSTR5, along with D2R. SSAs and DAs proved to be effective in reducing tumor mass. When used in combination, they are able to inhibit gonadotropin secretion both *in vitro* and *in vivo*.
- In non-functioning pituitary adenomas, SSTR3 is highly expressed, whereas SSTR2 and D2R are expressed at lower level. They are rarely associated with SSTR1. In this context, SSTR3 selective agonists represent potential treatment candidates.

As reported above, the therapeutic efficacy of the already clinically available SSAs is strongly influenced by the marked variability of the expression pattern of SSTRs. Therefore, further studies are needed to better understand the impact of this heterogeneity on treatment response and resistance, and to develop more specific and effective compounds for NETs therapy (Cakir et al., 2010; Barbieri et al., 2013).

Section 1.2: The ALT Phenotype in Neuroendocrine Tumors

1.2.1 Telomeres and Telomere Maintenance Mechanisms (TMMs)

Telomeres are specialized ribonucleoprotein structures that protect the terminal regions of linear chromosomes. They consist of long stretches of double-stranded, G-rich repeat sequences, which in humans range from 9 to 15 kilobases in length. Human telomeres are made up of multiple kilobases of $(TTAGGG)_n$ repeat sequences, characterized by a G-rich leading strand and a C-rich lagging strand. The G-rich strand extends toward the 3’ end for 50-300 nt, forming a structure known as the G-overhang (Dilley and Greenberg, 2015; O’Sullivan and Karlseder, 2010).

The double and single stranded repeats are bound to a six-protein complex (TRF1, TRF2, RAP1, TIN2, TPP1, and POT1) known as shelterin complex. These factors facilitate the formation of a protective telomeric structure called the telomere loop (T-loop), which is created when the single-stranded G-overhang invades the double-stranded TTAGGG repeat region (Figure 10). This invasion effectively conceals the G-tail, enabling the cell to distinguish natural chromosome ends from double-stranded breaks. Indeed, the closed structure of the T-loop functions as a protective cap, clearly defining the natural end of the chromosome and preventing the DNA damage response (DDR) machinery from recognizing the telomere (O’Sullivan and Karlseder, 2010).

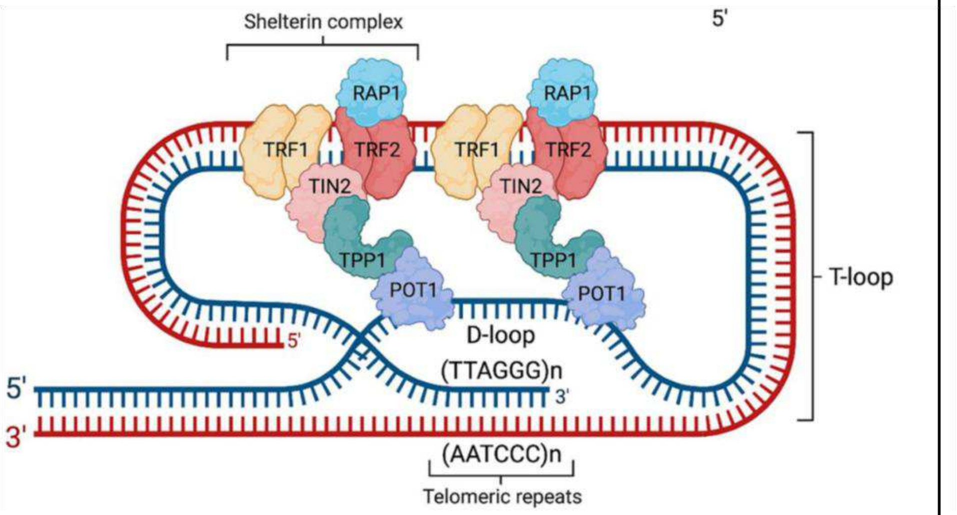

Figure 10. *Telomere structure. The lagging strand ends with a 50–200 nucleotide overhang, which tends to fold back and invade the double-stranded TTAGGG repeat region. Interaction with the shelterin protein complex (TRF1, TRF2, RAP1, TIN2, TPP1, and POT1) stabilizes the structure, known as the T-loop (reproduced under CC BY 4.0 from Daniela Muoio et al., "Functions of ADP-ribose transferases in the maintenance of telomere integrity", 2022).*

In somatic cells, which typically lack a telomere maintenance mechanism (TMM), telomeres shorten with each cell cycle, ultimately resulting in replicative senescence (Dilley and Greenberg, 2015).

One of the main hallmarks of cancer cells is replicative immortality (Hanahan and Weinberg, 2011), which is achieved by activating a TMM pathway. This is crucial for the formation and sustained growth of aggressive tumors (Dilley and Greenberg, 2015).

Neoplastic cells typically engage one of the two TMMs to preserve their telomere length during unchecked proliferation (Figure 11). The first of these mechanisms involves the reactivation of telomerase (TEL+ phenotype), a high-fidelity DNA transferase with reverse transcription activity. This enzyme is composed of a telomerase RNA component, known as hTR, and a protein subunit called human telomerase reverse transcriptase (hTERT), along with several accessory proteins. Telomerase functions by adding TTAGGG repeats one at a time to the shortened telomeric ends, thereby restoring their length. Telomerase upregulation is closely associated with tumorigenic transformation and is observed in approximately 80–90% of all malignancies (MacKenzie et al., 2021).

In a smaller, yet significant, proportion of neoplasms (10–20%), activation of a second TMM is observed, known as alternative lengthening of telomeres (ALT). ALT depends on several DNA damage response (DDR) proteins, particularly those involved in the homology-dependent repair (HDR) pathway. ALT-positive (ALT+) tumors exploit the repetitive nature of telomeric sequences to promote strand invasion, where one telomeric strand invades another. The complementary sequences uncovered through this process act as templates for elongating the invading strand. This homology-directed invasion can occur into the homologous chromosome, a non-homologous chromosome, or even extrachromosomal telomeric repeats (ECTRs). Engaging the ALT pathway gives tumors distinct molecular features, several of which are commonly used as indicators of ALT activity (MacKenzie et al., 2021).

ALT is observed in various common cancers, including breast carcinomas, but it appears more frequently in tumors of mesenchymal origin, though the underlying reasons for this association are not yet well understood. These tumors include glioblastoma multiforme, osteosarcomas, and certain soft tissue sarcomas. Moreover, the ALT+ phenotype is often associated with a particularly poor prognosis (Cesare and Reddel, 2010).

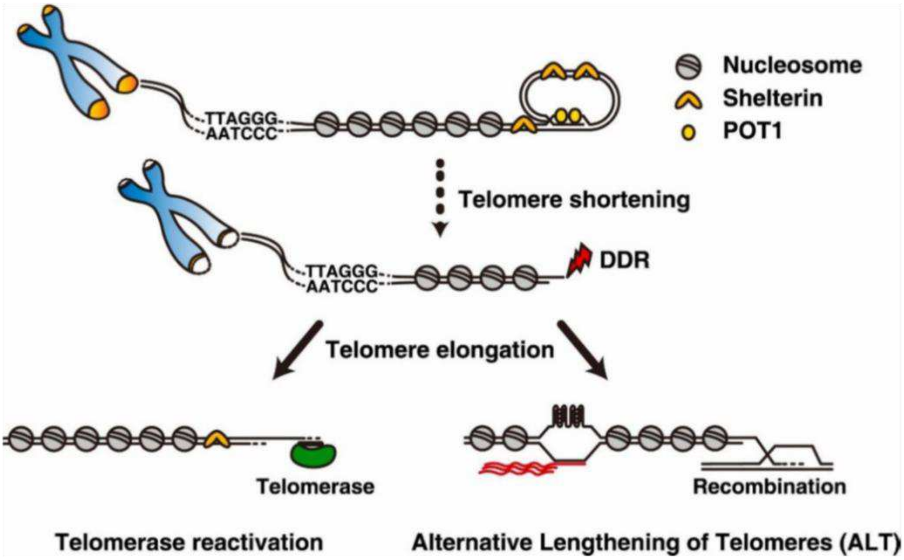

Figure 11. *Telomere maintenance mechanisms (TMMs). During cell division, eukaryotic chromosomes undergo telomere shortening. Critically short telomeres can be recognized as DNA damage sites, triggering a DNA damage response (DDR) that leads to cell cycle arrest and induces cellular senescence. Cancer cells bypass this condition through telomere maintenance mechanisms: either telomerase reactivation or alternative lengthening of telomeres (ALT) (reproduced with permission from Elsevier: Seminars in Cell & Developmental Biology, "Alternative paths to telomere elongation", Jennifer J. Lee et al., 2021).*

1.2.2 Molecular Markers of ALT Activity

While retaining many canonical features of telomeres – such as the presence of TTAGGG duplex repeats, single-stranded G-tails, the shelterin complex and other associated proteins, and the ability to form T-loops – ALT+ tumor cells also exhibit several uncommon characteristics (Cesare and Reddel, 2010; Claude and Decottignies, 2020).

One of the most notable features is the abundant presence of extrachromosomal telomeric DNA repeats (ECTR). These elements may take on multiple forms, such as:

- Predominantly double-stranded telomeric circles (t-circles) (Figure 12);
- Partially single-stranded circles (C-circles or G-circles depending on whether they consist of the C-rich or G-rich strand, respectively) (Figure 12);
- Linear double-stranded DNA;
- High molecular weight "t-complex" DNA containing abnormal, highly branched structures (Cesare and Reddel, 2010; Claude and Decottignies, 2020).

Telomeric DNA (both chromosomal and extrachromosomal) along with associated binding proteins can also be found within a subset of promyelocytic leukemia nuclear bodies (PML nuclear bodies). These structures, known as ALT-associated PML bodies (APBs), are highly characteristic of ALT+ tumors and are thought to represent the sites of ALT-mediated homologous recombination and telomere extension (Cesare and Reddel, 2010; Claude and Decottignies, 2020; Sobinoff and Pickett, 2017).

Additional features of ALT+ cancer cells include highly variable chromosomal telomere lengths, rapid fluctuations in telomere length, and significantly increased levels of telomeric recombination (Cesare and Reddel, 2010; Claude and Decottignies, 2020).

In addition, high levels of telomeric exchange between sister chromatids (T-SCEs) resulting from telomeric crossover events was reported to occur at rates several orders of magnitude higher in ALT+ cells compared to telomerase-positive or normal cells, with no corresponding increase in SCE frequency elsewhere in the genome (Cesare and Reddel, 2010; Claude and Decottignies, 2020; Sobinoff and Pickett, 2017).

Finally, ALT+ cells typically exhibit an increased DNA damage response at telomeres, primarily as a result of replication stress. At the molecular level, this is evidenced by the co-localization of telomeric foci with DNA damage markers such as 53BP1 (p53 binding protein 1) or γH2AX, forming structures known as telomere dysfunction-induced foci (TIFs) (Sobinoff and Pickett, 2017).

These phenotypic features of ALT provide valuable indicators of ALT activity, but they differ in their level of specificity for ALT phenotype (Cesare and Reddel, 2010; Claude and Decottignies, 2020).

C-circles

Unlike t-circles – double-stranded DNA molecules likely formed through enzymatic resolution of t-loop junctions and associated with both ALT and normal telomere biology – C-circles are a much more distinctive and specific feature of ALT+ cells. In fact, it has been demonstrated that the level of ALT activity correlates quantitatively with the abundance of these elements, which are composed of partially double-stranded circular DNA featuring a complete C-rich strand and an incomplete G-rich strand. It was estimated that an individual cell from one ALT+ cell line contains roughly 1˙000 C-circles. ALT+ cells also contain G-circles, but at levels roughly 100 times lower than C-circles (Cesare and Reddel, 2010; Henson et al., 2009).

The origin of C-circles is not fully understood, but it is speculated that they may result from the nucleolytic degradation of the G-rich strand of t-circles (Cesare and Reddel, 2010; Henson et al., 2009).

Studies on these specific structures suggest that C-circles may constitute the most robust biomarker of the ALT phenotype identified to date, as their levels are, on average, approximately 750-fold higher in ALT+ cells compared to TEL+ or non-immortalized cell lines (Cesare and Reddel, 2010; Henson et al., 2009).

Furthermore, the detection of C-circles in blood samples from patients with ALT+ osteosarcomas suggests that measuring C-circle levels could serve as a minimally invasive blood-based assay for diagnosing ALT+ tumors or monitoring treatment efficacy (Cesare and Reddel, 2010; Henson et al., 2009).

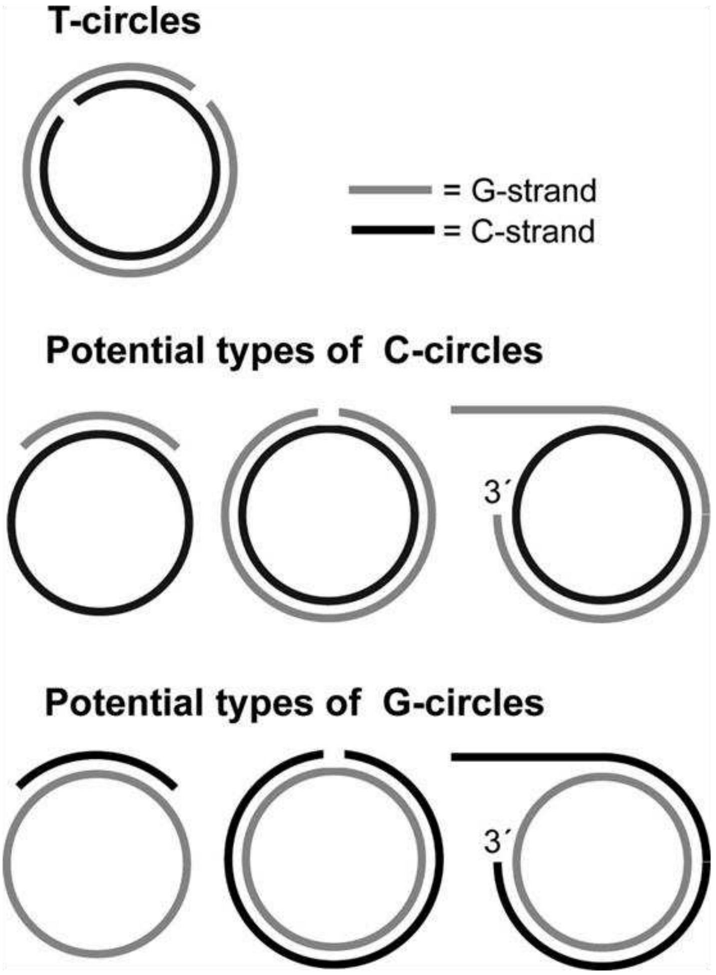

Figure 12. *Representation of different types of circular extrachromosomal telomeric DNA repeats (ECTR). T-circles are fully double-stranded DNA molecules, while C-circles and G-circles are partially single-stranded and differ in the composition of the complete strand (C-rich and G-rich, respectively) (reproduced with permission from John Wiley and Sons: FEBS Letters, "Assaying and investigating Alternative Lengthening of Telomeres activity in human cells and cancers", Jeremy D. Henson and Roger R. Reddel, 2010).*

1.2.3 Genetics of ALT Phenotype

The activation of the ALT mechanism is closely linked to the loss of ATRX (α thalassemia/mental retardation syndrome X-linked chromatin remodeler) and DAXX (death-domain associated protein) function. ATRX and DAXX are implicated in the remodeling of chromatin at telomeric loci; more precisely, they function as a complex that facilitates the incorporation of the non-canonical histone variant H3.3 into pericentromeric and telomeric heterochromatin (Clatterbuck Soper and Meltzer, 2023; Heaphy et al., 2011).

Loss of function of these two protein factors is often associated with mutations in their corresponding genes (*ATRX* and *DAXX*), typically deletions or truncating nonsense mutations. However, loss of protein expression has also been observed in the absence of coding sequence alterations, suggesting that reduced expression may result from promoter-level changes, splicing defects, or epigenetic modifications (Clatterbuck Soper and Meltzer, 2023). Notably, loss-of-function alterations in *ATRX* and *DAXX* are typically mutually exclusive. Such mutations are commonly identified in malignancies including osteosarcomas, gliomas, liposarcomas, and PanNETs, as outlined above (Clatterbuck Soper and Meltzer, 2023).

At the molecular level, ATRX belongs to the SNF2 family of ATP-dependent chromatin remodelers, while DAXX functions as a histone chaperone involved in chromatin regulation. ATRX associates with DAXX to deposit the histone variant H3.3 in a replication-independent chromatin assembly pathway (Lovejoy et al., 2020). The ATRX/DAXX complex accumulates at PML nuclear bodies, which likely function as storage sites for soluble H3.3, primed for deposition by ATRX/DAXX. ATRX/DAXX preferentially binds to repetitive DNA elements, especially G-rich repeats and sequences capable of forming secondary structures, with the TTAGGG telomeric repeat being a prominent target (Figure 10). Upon binding, the complex mediates epigenetic silencing of these regions (Clatterbuck Soper and Meltzer, 2023). ATRX and DAXX are also thought to promote genome stability by facilitating the resolution of G-quadruplex (G4) DNA structures, thereby reducing replication stress. Additionally, they help prevent the accumulation of R-loops during transcription, which in turn protects telomeric regions from DNA double-strand breaks. Lastly, the ATRX/DAXX complex plays a key role in DNA repair synthesis during homologous recombination (van ´t Veld et al., 2025) (Figure 13).

Given the crucial role this complex plays in maintaining telomeric integrity, loss of function in either of its components – most commonly through silencing of ATRX (90% of cases) – leads to a cascade of molecular alterations that ultimately result in genomic instability and tumorigenesis (Figure 10). Specifically, the following effects are observed:

- Alternative lengthening of telomeres (ALT);
- Double-strand breaks;

- Impaired homologous recombination.

(Hou et al., 2022; van ´t Veld et al., 2025).

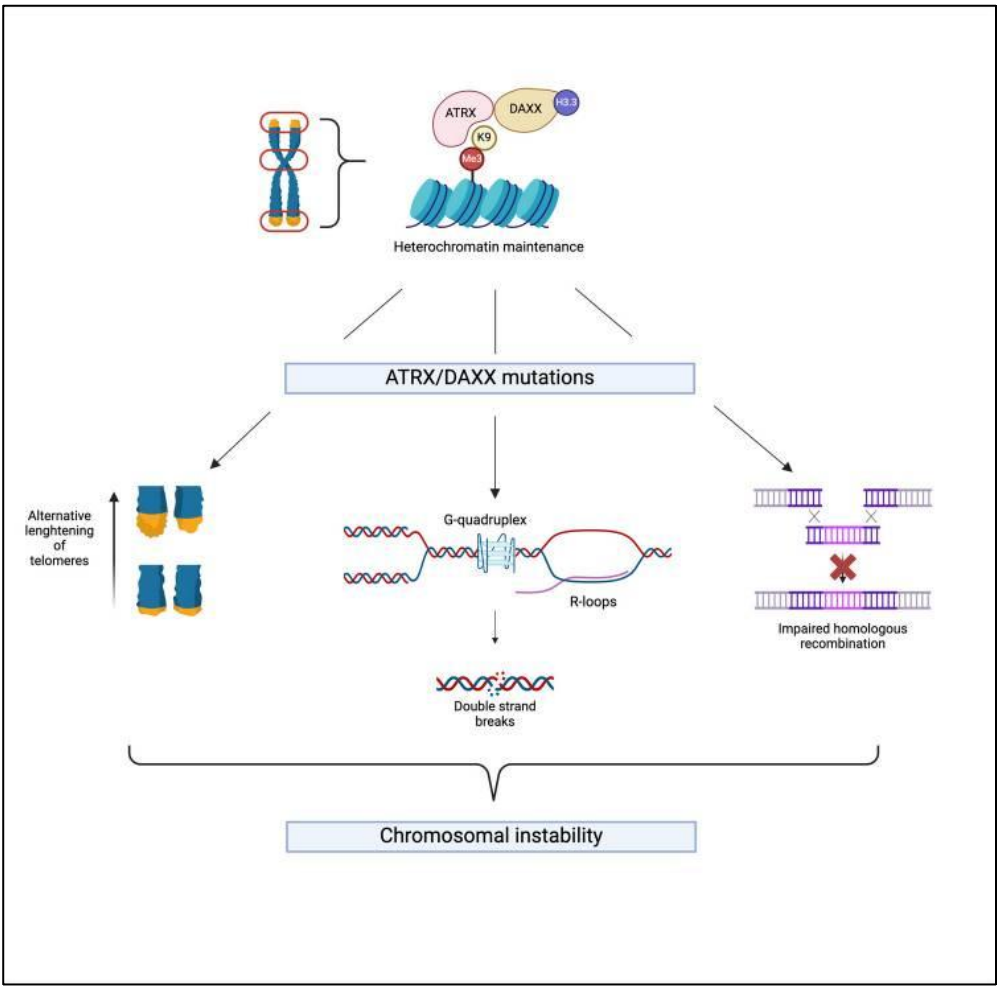

Figure 13. *Consequences of ATRX and/or DAXX mutations. ATRX and DAXX form a histone chaperone complex that deposits the histone variant H3.3 in repetitive heterochromatin regions, such as telomeric and pericentromeric domains. Mutations in these proteins are linked to chromosomal instability and tumorigenesis through several mechanisms: activation of alternative lengthening of telomeres (ALT), accumulation of DNA double-strand breaks due to unresolved G-quadruplexes and R-loops, and impaired homologous recombination (reproduced under CC BY 4.0 from Brenna R. van ´t Veld et al., "Clinical Relevance of ATRX/DAXX Gene Mutations and ALT in Functioning Pancreatic Neuroendocrine Tumors", 2025).*

As already mentioned, mutations in *ATRX* and *DAXX* are frequently observed in PanNETs and play a critical role in their pathogenesis (see Paragraph 1.2.6). However, these mutations do not appear to drive tumor initiation but rather emerge at later stages, correlating with progression to metastatic disease and poorer survival outcomes (van ´t Veld et al., 2025).

1.2.4 Telomere Recombination in ALT+ Cells

Recent studies have shown that ALT operates through recombination-based mechanisms, though the precise elongation step remains unclear. Multiple, non-mutually exclusive models have been proposed (Cesare and Reddel, 2010; Lee et al., 2021). One model involves frequent telomeric sister chromatid exchanges (T-SCEs), where unequal events may result in asymmetric telomere length inheritance, sustaining proliferation in some daughter cells (Nabetani and Ishikawa, 2009; Bailey et al., 2004). Another hypothesis suggests HR-dependent telomere synthesis using other telomeres, extrachromosomal DNA, or t-loops as templates (Figure 14), with RAD51 enabling strand invasion (Cho et al., 2014). Circular DNA structures like C-circles and t-circles may also support telomere elongation through rolling circle amplification (RCA; see Paragraph 1.2.5) (Henson et al., 2002; Cesare and Reddel, 2010).

An alternative model involves a RAD51-independent, break-induced replication (BIR) pathway, where telomeric damage triggers homology-directed synthesis via a break-induced replisome, with RAD52 as a key factor (Dilley et al., 2016; Kramara et al., 2018; Zhang et al., 2019). ALT is thus considered a dynamic and adaptable mechanism during tumor progression (Lee et al., 2021).

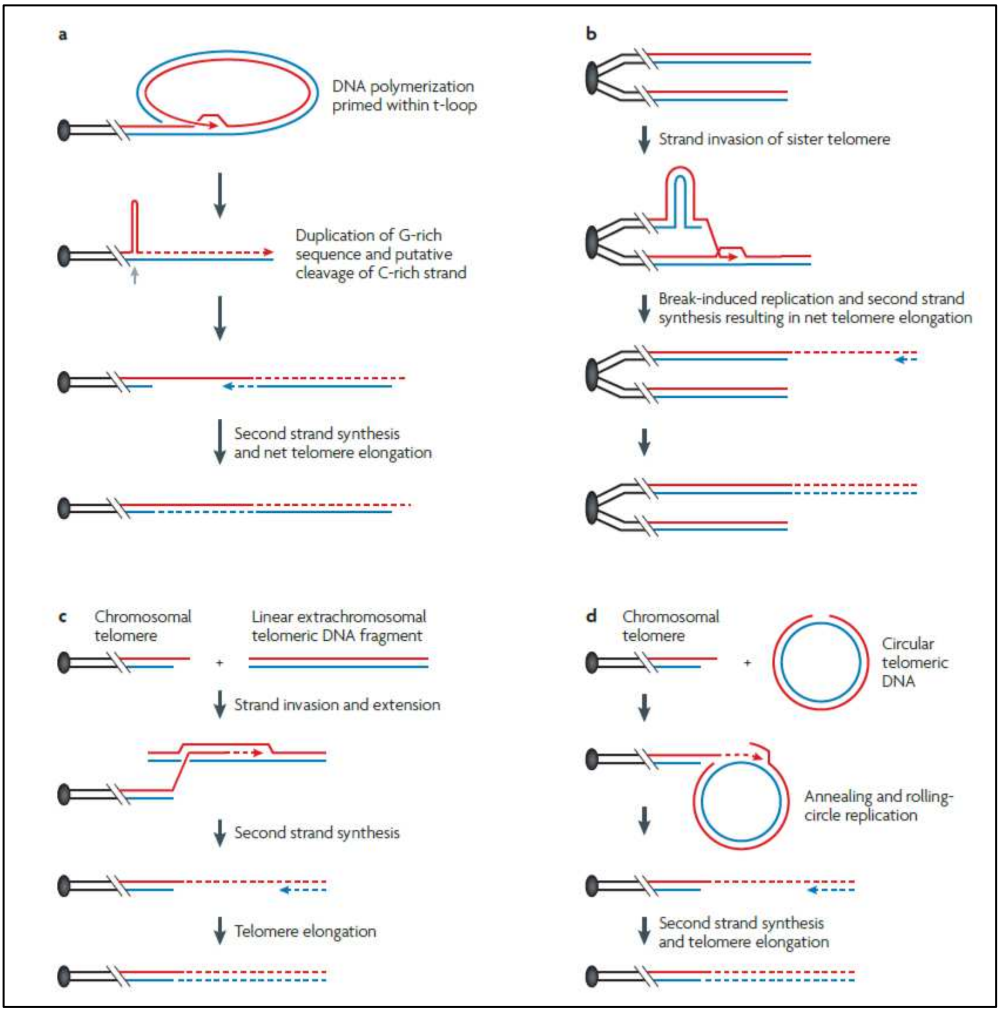

Figure 14. *Alternative copy templates for recombination-mediated synthesis of telomeric DNA. In ALT-mediated telomere elongation, the template for DNA synthesis can derive not only from an adjacent chromosomal telomere, but also from: the same telomere via the t-loop structure (**a**); the sister chromatid telomere (**b**); linear extrachromosomal telomeric DNA (**c**); or circular extrachromosomal telomeric DNA (**d**) (reproduced with permission from Springer Nature: Nature Reviews Genetics, "Alternative lengthening of telomeres: models, mechanisms and implications", Anthony J. Cesare and Roger R. Reddel, 2010).*

Essential to ALT activity is the MRN complex (MRE11, RAD50, NBS1), which senses DNA breaks and promotes ATM recruitment and 5′–3′ DNA end resection to initiate recombination (Jiang et al., 2005; Zhong et al., 2007; Lee and Paull, 2007).

During S/G2 phases, MRN localizes to telomeres via TRF2 interaction (Zhu et al., 2000), enabling strand invasion and telomeric elongation (Verdun et al., 2005; Deng et al., 2009; Dimitrova and de Lange, 2009).

The SMC5–SMC6 complex, particularly through its MMS21 subunit, also supports ALT by promoting sumoylation of shelterin components (TRF1, TRF2, RAP1) and facilitating the formation of ALT-associated PML bodies (APBs) (Potts and Yu, 2007; Potts, 2009; Cesare and Reddel, 2010). Moreover, due to replication stress at critically short telomeres, ALT+ cells rely on repair factors such as FEN1, MUS81, FANCD2, and FANCA to resolve stalled forks and prevent telomere loss (Saharia and Stewart, 2009; Zeng et al., 2009; Fan et al., 2009).

1.2.5 Rolling Circle Amplification (RCA) as a Clinical Tool for ALT+ Cancers

As previously stated, C-circles are one of the most specific markers of the ALT phenotype. They may also participate in telomeric recombination by acting as templates for telomere elongation via a mechanism called rolling circle amplification (RCA). The RCA-mediated elongation model likely involves the annealing of a telomeric G-rich overhang to a single-stranded region of a C-circle, followed by DNA polymerization from the chromosome end, facilitating rapid synthesis of G-rich telomeric DNA (Cesare and Reddel, 2010).

RCA is recognized as a sensitive experimental technique for detecting circulating DNA, including complete or partial double-stranded circular telomeric DNA (t-circles and C-circles) present in ALT+ cells (Dean et al., 2001; Zellinger et al., 2007). In 2009, Henson JD and colleagues developed the C-circle (CC) assay, a method specific for detecting C-circles in ALT+ models. This assay utilizes rolling circle amplification of partially double-stranded C-circles by Φ29 DNA polymerase, which is auto-primed by the partial G-strand ($[TTAGGG]_n$), resulting in the production of long single-stranded telomeric DNA concatemers (Figure 15) (Henson et al., 2009). Φ29 is a highly processive DNA polymerase derived from the *Bacillus subtilis* phage Φ29, typically producing rolling circle amplification products of 70 kb or more. Importantly, this polymerase can carry out amplification under isothermal conditions (Dean et al., 2001).

The authors validated the assay across multiple models, including 18 ALT+ cell lines, 15 telomerase-positive lines, and 5 non-immortalized (mortal) strains. On average, C-circle levels in ALT+ cells were found to be 750 times higher than those in ALT− lines. More broadly, all tumor-derived ALT+ cell lines exhibited C-circle levels at least 100 times greater than the highest level detected in ALT− controls. ALT− cell results were comparable to background levels observed in control reactions lacking either Φ29 DNA polymerase or input DNA (Henson et al., 2009).

The assay also proved effective when applied to whole blood samples from pediatric osteosarcoma patients with previously determined ALT status. C-circle levels were markedly elevated in ALT+ patients, showing approximately a fivefold increase compared to ALT− patients and a sevenfold increase relative to healthy controls (Henson et al., 2009).

The significance of this study lies not only in the authors' confirmation of the specificity of C-circles as a marker of the ALT phenotype, but also in their demonstration of the CC assay's value as an indicator of ALT activity levels. Moreover, the assay shows strong potential for clinical applications, including diagnosis, therapeutic optimization, and monitoring of disease recurrence in ALT+ tumors (Henson et al., 2009).

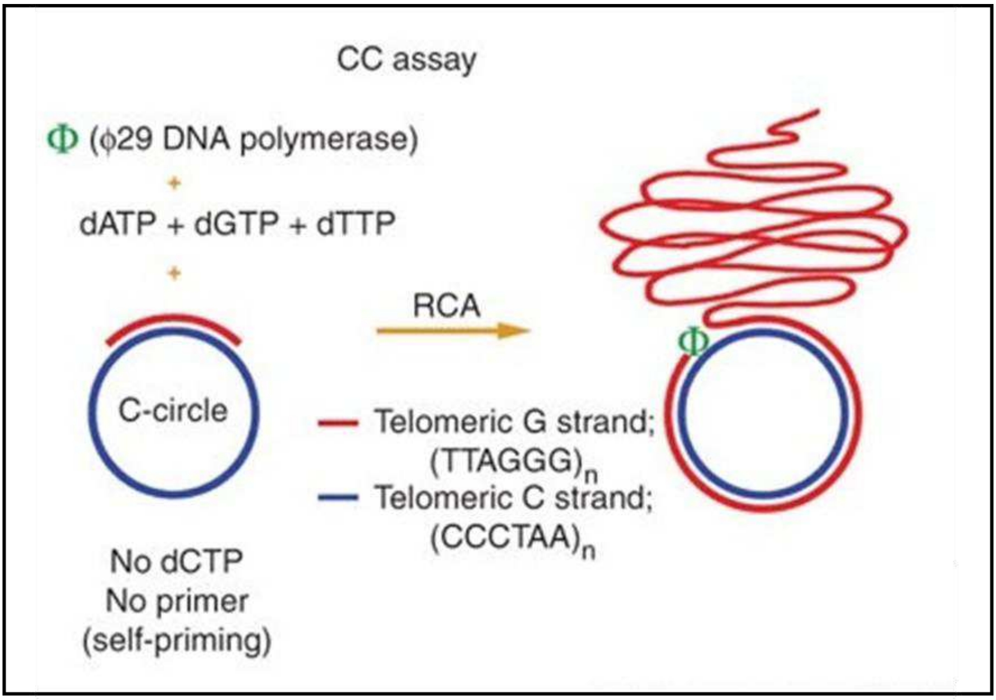

Figure 15. Schematic representation of the C-circle (CC) assay. The use of Φ29 DNA polymerase enables primer-free amplification of C-circles through a mechanism known as rolling circle amplification (RCA). The amplification product consists of single-stranded DNA concatemers (reproduced and adapted with permission from Springer Nature: Nature Biotechnology, "DNA C-circles are specific and quantifiable markers of alternative-lengthening-of-telomeres activity", Jeremy D. Henson et al., 2009).

1.2.6 ALT in Pancreatic Neuroendocrine Tumors

As discussed in Paragraph 1.1.7, PanNETs have been shown to harbor recurrent mutations in the *ATRX* and *DAXX* genes (Jiao et al., 2011), causing loss of nuclear expression of their respective proteins and highly correlating with ALT. These alterations are considered key drivers of PanNETs progression, with alterations occurring in ≥ 40% of cases (Singhi et al., 2017; Konukiewitz et al., 2021).

Alterations in *ATRX*/*DAXX* appear to occur late in tumorigenesis, being detectable only in large, fully developed NETs. Moreover, NETs harboring *ATRX*/*DAXX* mutations are associated with a poorer prognosis compared to those with wild-type *ATRX*/*DAXX* (Konukiewitz et al., 2021; Kim et al., 2017).

The prognostic relevance of *ATRX*/*DAXX* loss in PanNETs was underscored by a 2017 study by Singhi AD and colleagues. Analyzing a cohort of patients with pancreatic neuroendocrine tumors – 31% ALT-positive and 69% ALT-negative – the authors assessed disease-free survival (DFS) and disease-specific survival (DSS) across both groups. Overall, patients with ALT+ tumors showed lower outcomes for both parameters, with a DFS rate of 63% at 3 years and 40% at 5 years, and a DSS rate of 81% at 5 years and 50% at 10 years. In contrast, ALT− patients demonstrated significantly better outcomes, with DFS rates of 99% at 3 years and 96% at 5 years, and DSS rates of 93% at 5 years and 89% at 10 years (Figure 16) (Singhi et al., 2017).

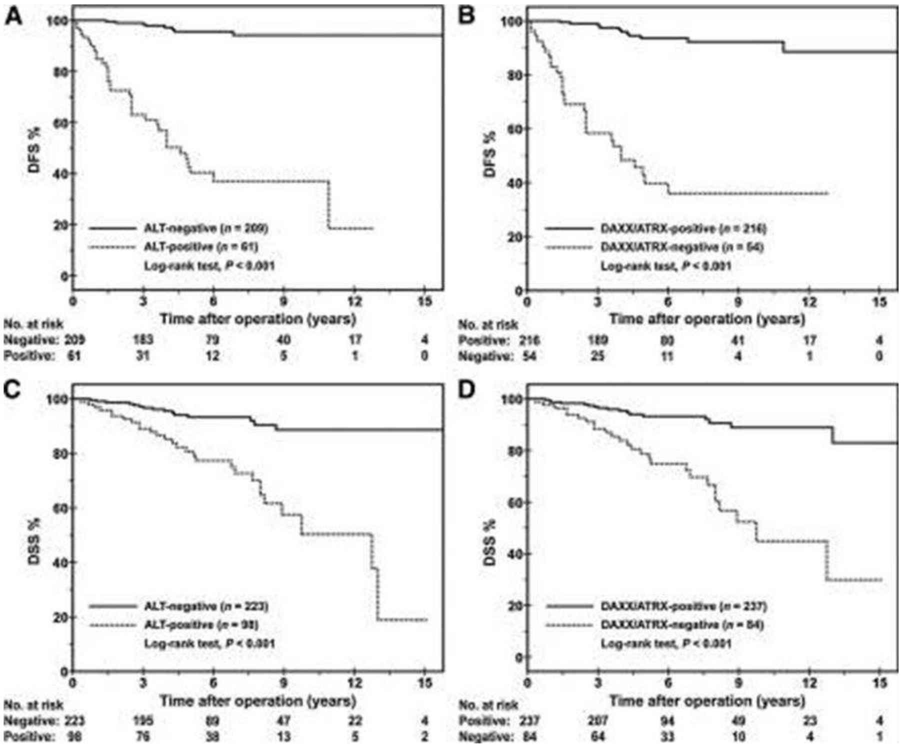

Figure 16. *Kaplan–Meier curves showing cumulative probabilities of disease-free survival (DFS) and disease-specific survival (DSS) after surgical resection in PanNET patients, stratified by ALT and DAXX/ATRX status. ALT-positive and DAXX/ATRX-negative tumors were associated with shorter DFS (A, B) and shorter DSS (C, D) compared to ALT-negative and DAXX/ATRX-positive cases (reproduced with permission from American Association for Cancer Research: Clinical Cancer Research, "Alternative Lengthening of Telomeres and Loss of DAXX/ATRX Expression Predicts Metastatic Disease and Poor Survival in Patients with Pancreatic Neuroendocrine Tumors", Aatur D. Singhi et al., 2017).*

Overall, the late onset of *ATRX*/*DAXX* loss in PanNETs strongly suggests that these mutations act as drivers in the progression toward metastatic disease. Furthermore, detecting *ATRX*/*DAXX* loss in patients with PanNETs may carry important diagnostic implications and contribute to optimizing therapeutic decision-making (Singhi et al., 2017).

1.2.7 Anti-TMM Therapies and New Strategies for ALT+ Tumors

Anti-TMM therapies have long been investigated for their potential use as anticancer treatments in clinical settings. However, such approaches have shown potential limitations and challenges for several reasons.

Specifically, telomerase inhibition has been shown to involve a significant lag phase between enzyme suppression and the telomere shortening required to halt tumor cell proliferation, potentially affecting the overall efficacy of the therapy. Furthermore, this therapeutic approach has raised significant concerns regarding potential side effects on normal cell populations that physiologically express telomerase, such as hematopoietic stem cells. In parallel, there remains the risk of triggering compensatory resistance mechanisms, most notably the activation of the ALT pathway. Finally, the use of telomerase inhibitors may give rise to surviving cell populations characterized by elevated genomic instability, potentially resulting in the development of more aggressive tumors (Shay and Wright, 2002).

Despite these concerns, a specific telomerase inhibitor, Imetelstat, is currently being evaluated in phase 2/3 clinical trials, showing promising results in terms of both therapeutic efficacy and safety (Gutierres and Villanueva, 2020).

As for anti-ALT therapies, no specific pharmacological agent has yet been identified for selectively targeting tumors exhibiting this phenotype (Cesare and Reddel, 2010). However, studies on certain compounds have demonstrated a particularly pronounced cytotoxic effect in ALT+ cells. One of these compounds is Adavosertib, a WEE1 inhibitor (WEE1i) currently under clinical investigation. WEE1 functions as a cell cycle checkpoint kinase activated by the ataxia-telangiectasia Rad3-related protein (ATR) under conditions of replicative stress. It contributes to cell cycle arrest at the S/G2 phase, thereby allowing the activation of various pathways involved in replication fork remodeling and DNA damage repair. Inhibition of WEE1 compromises the S/G2 checkpoint in response to replication stress, leading to the accumulation of extensive DNA damage that ultimately results in mitotic catastrophe and cell death (Figure 14) (Zhang et al., 2024). This mechanism of action makes Adavosertib particularly promising for the cytotoxic treatment of ALT+ tumor cell lines and supports its potential future clinical application.

Another compound currently undergoing clinical evaluation is Ceralasertib. This agent targets the same pathway as Adavosertib but acts upstream of WEE1, functioning as an inhibitor of the ATR kinase (Foote et al., 2018). ATR inhibition appears to disrupt the ALT-dependent homologous recombination-based telomere maintenance mechanism, leading to telomere attrition and ultimately resulting in cell death (Figure 17) (Forment and O’Connor, 2018). For this reason, the clinical use of this compound holds potential for providing therapeutic benefit in the treatment of ALT+ tumors.

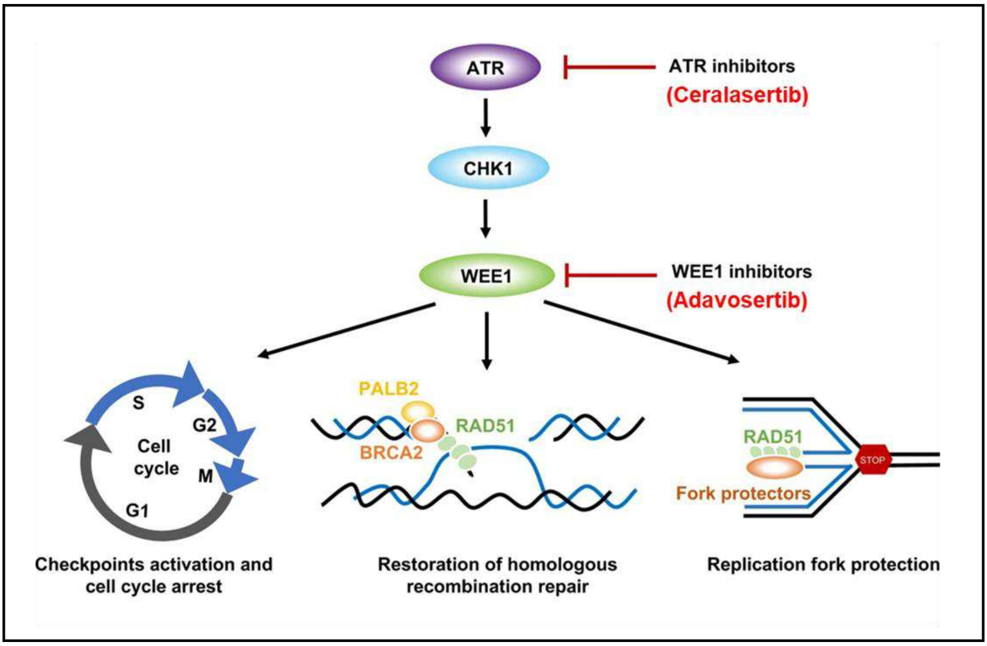

Figure 17. *Mechanism of action of WEE1 and ATR inhibitors. Adavosertib inhibits the WEE1 signaling pathway, inducing cell apoptosis through mitotic catastrophe. Ceralasertib acts further upstream by inhibiting ATR, leading to the same outcome (reproduced and adapted with permission from Elsevier: Pharmacological Research, "Cell cycle checkpoints and beyond: Exploiting the ATR/CHK1/WEE1 pathway for the treatment of PARP inhibitor–resistant cancer", Nitasha Gupta et al., 2022).*

Section 1.3: Experimental Models

1.3.1 Experimental Models for the Characterization of Novel Dual Somatostatin Analogs

For the characterization of novel somatostatin analogs, the following NET cell models were employed:

- AtT-20 cell line: it was isolated from the anterior pituitary gland of a mouse with a corticotroph tumor and characterized in 1962 (Buonassisi et al., 1962). Cells are epithelial-like and loosely adherent and are able to secrete the adrenocorticotropic hormone (ACTH) in the culture medium (Figure 18A). This cell line has a doubling time of ~ 72 hours and is also characterized by high level of expression of SSTR2 and SSTR5 (Cervia et al., 2003).
- NT-3 cell line: it is lymph node–derived and was isolated from a 33-year-old male patient with a well-differentiated, functioning insulinoma. Cells are characterized by slow growth (doubling time of 10.9 ± 0.7 days), active insulin secretion, epithelial-like morphology, and a loosely adherent phenotype (Figure 18B). This cell line exhibits high protein-level expression of SSTR3, followed by SSTR2 and SSTR5 (Benten et al., 2018).

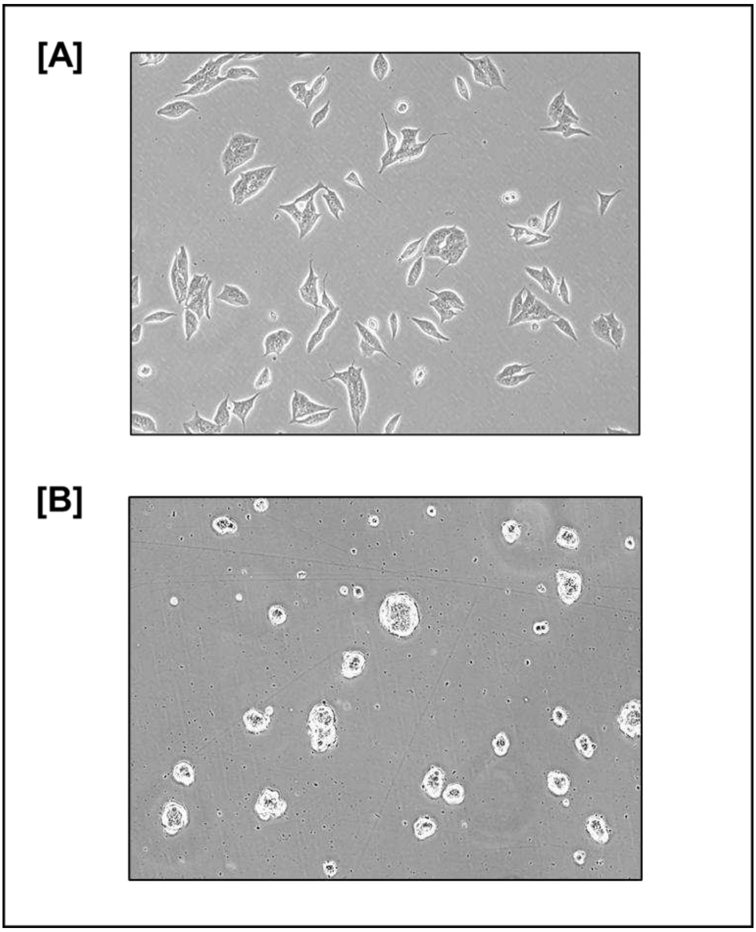

Figure 18. *Cellular models of NETs used for the characterization of novel SSAs. (**A**) AtT-20 cell line; (**B**) NT-3 cell line.*

1.3.2 Experimental Models for the Detection of ALT Activity in Neuroendocrine Tumors

The characterization of ALT activity and the detection of C-circles were performed using the following cell models:

- NT-18P cell line: derived from a 57-year-old male patient with a grade G3 pancreatic neuroendocrine tumor and characterized in 2022 (Viol et al., 2022). The cells exhibit an elongated morphology with a tendency to form clusters, grow in adherence, and have a doubling time of 4.64 days (Figure 19A). Notably, they harbor an inactivating frameshift mutation in the *DAXX* gene, making them an interesting model for studying ALT activity (Viol et al., 2022).

- NT-18LM cell line: Derived from a liver metastasis originating from the same primary tumor as the NT-18P cell line (Viol et al., 2022). The cells retain a tendency to form clusters but exhibit a more rounded morphology (Figure 19B). This cell line has a doubling time of 6.35 days. Like NT-18P, these cells also harbor an inactivating frameshift mutation in the *DAXX* gene, associated with the ALT phenotype (Viol et al., 2022).
- SaOS-2 cell line: it is a human cell line derived from a well-differentiated, osteoblastic osteosarcoma. This line was established from a female adolescent patient and first characterized by Fogh et al. in 1977 (Fogh et al., 1977). The cells exhibit an epithelioid morphology, an adherent phenotype, and a doubling time of approximately 72 hours (Figure 19C). Due to the presence of an *ATRX* mutation, this cell line serves as an optimal model for the study of ALT activity (Lovejoy et al., 2020; Clynes et al., 2015) and was used as a positive control (ALT+) in the present study.
- HFF cell line: it is derived from neonatal foreskin fibroblastic tissue and was characterized in 2003 (Amit et al., 2003). These cells exhibit a spindle-shaped morphology, grow in an adherent manner, and have a doubling time of approximately 48 hours (Figure 19D). This cell line was used as a negative control (ALT−) in the present study.

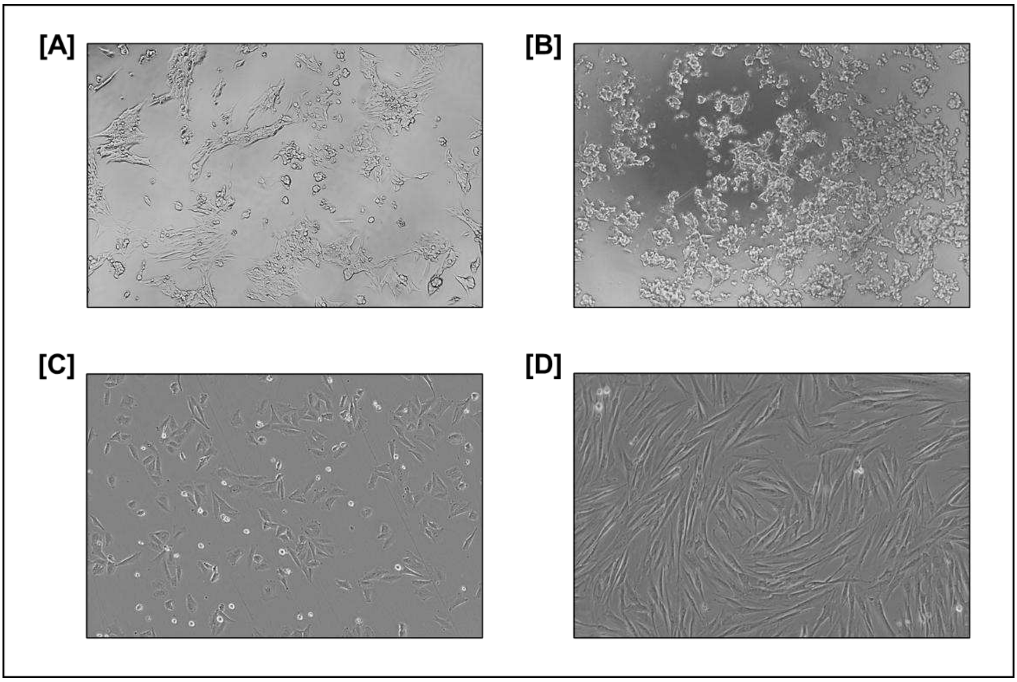

Figure 19. *Cellular models used to study ALT activity in neuroendocrine tumors. (A) NT-18P cell line; (B) NT-18LM cell line; (C) SaOS-2 cell line; (D) HFF cell line.*

2. Aim of the Study

Neuroendocrine tumors (NETs) are a heterogeneous group of relatively rare neoplasms whose incidence is increasing worldwide. They show substantial variability in site of origin, hormone secretion, genetic and molecular features, differentiation, aggressiveness, and clinical behavior, making their management challenging. This heterogeneity, together with their low frequency, hinders the development of effective treatments. Consequently, identifying biomarkers associated with poor prognosis and developing targeted therapeutic strategies for aggressive NETs is a key priority.

High somatostatin receptor (SSTR) expression in NETs has enabled targeted therapies using somatostatin analogs (SSAs). SSTRs (SSTR1–5) are GPCRs that, when bound by somatostatin, regulate cell growth, hormone secretion, apoptosis, angiogenesis, and migration. Clinically, SSAs such as octreotide, lanreotide, and pasireotide exploit these anti-secretory and anti-proliferative effects while overcoming somatostatin's short half-life. Although effective, their benefit varies due to heterogeneous SSTR subtype expression among tumors.

Early and accurate diagnosis of aggressive NETs would also prolong patients' survival. In pancreatic NETs (PanNETs), the activation of alternative lengthening of telomeres (ALT) mechanisms is associated with progressive disease and poor prognosis. The identification of markers of the ALT phenotype in these patients could help identifying more effective therapeutic strategies ultimately improving patients' outcome. The development of therapies targeting the ALT mechanism could represent a promising and innovative strategy for the treatment of NETs with a more aggressive clinical behavior.

This study originates from the growing need to characterize new SSAs with the potential to provide improved therapeutic efficacy and enable a higher degree of personalized treatment for NETs. It also addresses the need to identify molecular biomarkers associated with aggressive behavior in NET patients.

This work has two main objectives:

- **First objective**: to characterize five novel dual SSAs and evaluate their *in vitro* efficacy in comparison with standard-of-care compounds (octreotide and pasireotide) on pituitary (AtT-20) and pancreatic (NT-3) NET cell lines, by analyzing key cellular parameters such as hormone secretion, cell viability, and activation of receptor downstream pathways.
- **Second objective**: to characterize pancreatic NET cell lines (NT-18P and NT-18LM) for the presence of an ALT phenotype by optimizing molecular methods for the detection of circular extrachromosomal DNA (C-circles),

which are specific to this phenotype and may serve as potential diagnostic and therapeutic biomarkers.

3. Materials and Methods

3.1 Cell Cultures

The AtT-20, SaOS-2, and HFF cell lines were provided by the Helmholtz Munich institute (Germany). The NT-3, NT-18P, and NT-18LM cell lines were kindly provided by Dr. Jörg Schrader (University of Hamburg).

Cells were cultured in cell culture flasks (Greiner Bio-One, Germany, #690175, #658175, #661175; EuroClone, Italy, #ET7026, #ET7076, #ET7181) of different dimensions (25 cm^2, 75 cm^2, 182 cm^2) and were maintained at standard incubator conditions (37° C, 5% CO_2). For NT-3, NT-18P and NT-18LM cells, flasks were coated with collagen type IV from human placenta (50µg/ml in ddH_2O; Sigma-Aldrich, Germany, #C7521) to promote adhesion by adding 3 mL per flask, incubating for 30 minutes at room temperature and subsequently for 2 hours after removal under the same conditions to allow complete drying prior to seeding.

The compositions of the culture media used for each cell line were the following:

- Dulbecco's Modified Eagle Medium – high glucose (DMEM; Sigma-Aldrich, Germany, #D5796) supplemented with 10% Fetal Bovine Serum (FBS; Sigma-Aldrich, Germany, #F7524) and 1% Penicillin-Streptomycin (P/S; EuroClone, Italy, #ECB3001) for the AtT-20 and HFF cell lines;
- RPMI-1640 Medium (Sigma-Aldrich, Germany, #R5886) supplemented with 10% FBS, 1% P/S, 1% L-Glutamine 200 mM (Sigma-Aldrich, Germany, #G7513), 20 ng/mL Epidermal Growth Factor (EGF; Sigma-Aldrich, Germany, #E4127) and 10 ng/mL Fibroblast Growth Factor (FGF; Sigma-Aldrich, Germany, #01-106) for the NT-3, NT-18P and NT-18LM cell lines;
- McCoy's 5A Medium (Sigma-Aldrich, Germany, #M4892) supplemented with 15% FBS, 1% P/S, and 1% L-Glutamine for the SaOS-2 cell line.

Sub-culturing was performed when cells reached approximately 80% confluence. Cells were rinsed with Phosphate Buffered Saline (PBS; Sigma-Aldrich, Germany, #P4417) and incubated with 0.05% Trypsin/EDTA (Sigma-Aldrich, Germany, #T4174) for 3-5 minutes at 37° C, allowing them to detach. Cells were split by a ratio between 1:2 and 1:10 depending on the cell line and the confluence of the cells. Sub-culturing was performed at different time intervals depending on the doubling times of the different cell lines.

Cells were counted with a Burker chamber (BRAND, Germany, #719505) and an optical inverted microscope (Optika IM-3; Optika, Italy, #IM-300) or with an automated cell counter (Corning Cell Counter; Corning, USA, #6749). To discriminate living cells from dead cells, they were resuspended in Trypan Blue (Sigma-Aldrich, Germany, #93595) vital stain with a 1:2 cells/stain ratio.

For cell cryopreservation, cells were pelleted and resuspended in a freezing medium composed of FBS supplemented with 10% Dimethyl-Sulfoxide (DMSO; Sigma-

Aldrich, Germany, #472301). The cell suspensions were aliquoted in cryovials (Sigma-Aldrich, Germany, #V4757) and stored in a cell freezing container (Mr. Frosty; Thermo Fisher Scientific, USA, #C1562) filled with isopropyl alcohol (Sigma-Aldrich, Germany, #190764) at -80 °C for at least 48 hours. Long-term storage was carried out in liquid nitrogen at a maintained temperature of -196 °C.

All cell lines were maintained in culture for no more than 10–15 passages, and no maximum passage number was imposed for functional assays.
Cells were routinely tested for mycoplasma contamination, either by PCR using the N-GARDE Mycoplasma PCR Reagent Set (EuroClone, Italy, #EMK090020), or through a colorimetric reaction with the Mycolor One-Step Mycoplasma Detector kit (Vazyme, China, #EUR105), following the manufacturers' instructions.

3.2 Drugs

For the novel SSAs characterization project, the reference drugs octreotide and pasireotide were provided by D.B.A. Italia (Italy) and Italfarmaco (Italy), respectively. The experimental drug group included five novel SST analogs representing the object of our study, which were provided by the Grafton Therapeutics company (Switzerland), labeled as follows:

- B0012388 (working name SMTR-001)
- B0012387 (working name SMTR-002)
- B0012386 (working name SMTR-003)
- B0012385 (working name SMTR-004)
- B0012384 (working name SMTR-005)

All these drugs are peptides with a distinct molecular structure and show different affinities for the different types of SSTRs (Table 1). Binding data were provided by Grafton Therapeutics and generated through a competitive radioligand binding assay. Briefly, human SSTR 2 and SSTR5 were heterologously expressed in CHO-K1 cells, and competition binding experiments were performed using [^{125}I]-somatostatin-14 as the radiotracer and somatostatin-28 as the reference competitor. Test peptides were evaluated over a concentration range of 0.03 nM – 100 nM. Nonspecific binding was determined in the presence of a 200-fold excess of unlabeled competitor.

CODE	WORKING NAME	hSSTR2 (IC50, nM)*	hSSTR5 (IC50, nM)*
B0012388	SMTR-001	0,37	1,22
B0012387	SMTR-002	0,74	0,73
B0012386	SMTR-003	0,48	0,86
B0012385	SMTR-004	2,60	3,41
B0012384	SMTR-005	0,54	0,79

*Radioligand [^{125}I]-SST-14

Table 1. *Affinities of the experimental drugs SMTR-001 – 005 for SSTR2 and SSTR5. The lower the IC50 value, the higher the affinity of the analogue for the corresponding receptor. Data were provided by Grafton Therapeutics, Switzerland.*

Drugs were received in powder formulation and reconstituted with DMSO to obtain a 10 mM stock solution, then further diluted to obtain 1 mM working solutions. The aliquots, each with a volume of 50 µL, were stored at -20° C. Each aliquot was subjected to a maximum of four freeze–thaw cycles and used within 90 days.
In the experimental settings, drugs were administered as monotherapies. To reach the desired final concentration, the stock solutions were serially diluted in cell culture media. The working concentration at which cells were treated ranged from 1 nM to 100 nM. The maximum DMSO percentage in the treatments was 0.01%, and matched vehicle controls (non-treated, NT) with the same percentage were included in the experiments.

For the ALT phenotype characterization project, Adavosertib and Ceralasertib were provided by MedChemExpress (USA, #HY-10993 and #HY-19323, respectively). Adavosertib was received in a liquid formulation at a concentration of 10 mM in DMSO. Ceralasertib was received in powder form and was reconstituted with DMSO to obtain a 10 mM stock solution. The stock solutions of both compounds were further diluted to obtain working solutions at a concentration of 1 mM. To reach the desired final concentration, the stock solutions were serially diluted in cell culture media. The working concentration at which cells were treated ranged from 12.2 nM to 12.5 µM. The maximum DMSO percentage in the treatments was 0.125%, and matched vehicle controls (non-treated, NT) with the same percentage were included in the experiments.

3.3 Western Blot

The Western blot technique was applied to quantify the level of protein expression of the different SSTR subtypes in our experimental models.

To produce the cell pellets for the analysis, cells were seeded in 10 cm^2 dishes (Corning Costar, USA, #CLS430165) in amounts ranging from 500˙000 to 1x10^6 per dish and maintained at standard incubator conditions to promote cell division. Upon reaching a high level of confluence (≥80%), cells were rinsed with 5 mL PBS. After that, another 5 mL PBS were added, and cells were collected using a cell scraper (Corning Costar, USA, #CLS3010) keeping the dishes on ice to preserve the integrity of proteins, and deposited into 15 mL test tubes (Sigma-Aldrich, USA, #CLS430791). Cells were centrifuged at 13˙400 rpm for 5 minutes at 4° C. The supernatants were discarded; the pellets were resuspended in 1 mL PBS and then transferred into 1.5 mL test tubes (Eppendorf, Germany, #0030121023). Cells were centrifuged again at 13˙400 rpm for 5 minutes at 4° C. Finally, the supernatant was aspired, and the dry pellets were frozen at -80° C until the time of analysis.

Protein extraction was performed by using a specific lysis buffer composed of RIPA buffer (Sigma-Aldrich, Germany, #R0278), a protease inhibitor cocktail (cOmplete Mini, EDTA-free, 1X; Roche, Switzerland, #4693159001) and a phosphatase inhibitor cocktail (PhosSTOP 1X; Roche, Switzerland, #4906837001). The protein dosage of the obtained lysates was performed through the bicinchoninic acid (BCA) colorimetric assay (Pierce BCA Protein Assay; Thermo Fisher Scientific, USA, #23225), using bovine serum albumin (BSA; Sigma-Aldrich, Germany, #23209) as standard and by measuring the absorbance at 560 nm with a microplate reader (Fluostar Omega; BMG Labtech, Germany, #KBS-0024-002). The protein lysates were stored at -80° C until use.

To load the proteins on the gel, an equal volume of lysates and Laemmli 2X buffer (Bio-Rad, USA, #161-0737) (1:1 ratio) were mixed in a 1.5 mL test tubes and heated at 95° C for 5 minutes in a heater block (MPM Instruments, Italy, #M501-HBD) or, alternatively, incubated at room temperature (RT) for 30 minutes, to promote protein denaturation. The solutions were then mixed with a vortexer (Velp ZX3; Velp Scientifica, Italy, #399045) to remove condensation and subsequently loaded onto the gel. An amount of 50 μg of protein per sample was loaded onto the gel, in a volume ranging from 10 to 50 μL, depending on the initial concentration of the lysates.

The electrophoretic run was performed with an 4-12% acrylamide precast gel (mPAGE 4-12% Bis-Tris Precast Gel; Millipore, Sigma-Aldrich, Germany, #MP8W10), with the use of a specific running buffer 1X (mPAGE MOPS SDS Running Buffer Powder; Millipore, Sigma-Aldrich, Germany, #MPM0PS) solubilized in 1 L of distilled water, and a protein molecular weight marker (Prestained Protein SHARPMASS VII Protein MW Marker, 6.5-270 kDa; EuroClone, Italy, #EPS026500). The run was carried out at 80 V for 20 minutes and then at 120 V for ~ 1 hour.

At the end of the electrophoretic run, protein transfer was performed by using a nitrocellulose blotting membrane (Amersham Protran 0.45 µm NC; GE Healthcare, USA, #GE10600002) and a specific transfer buffer 1X (mPAGE Transfer Buffer Powder; Millipore, Sigma-Aldrich, USA, #MPTRB) solubilized in 900 µL of distilled water and 100 mL of methanol (MetOH; Sigma-Aldrich, USA, #34860). The transfer was performed at 4° C overnight, setting a current of 30 V and leaving the transfer tank in ice.

To verify the correct occurrence of protein transfer, the nitrocellulose membrane was colored with the Ponceau S red stain (Thermo Fisher Scientific, USA, #A40000279) to visualize the bands. The stain was then removed by rinsing the membrane in distilled water. At the same time, the gel was colored with the Coomassie Brilliant Blue stain (Brilliant Blue R; Sigma-Aldrich, Germany, #B6529) to verify the absence of protein bands. The gel was then rinsed in an appropriate de-staining buffer (40% MetOH, 10% Acetic Acid) and discarded.

For antibody incubation, the nitrocellulose membrane was first rinsed in Tris-Buffered Saline (TBS; 150 mM NaCl, 10 mM Tris, pH 8.0) – Tween (Tween 20; Sigma-Aldrich, Germany, #P9416) 0.1% buffer. The membrane was then saturated with a blocking solution composed of 5% BSA (Sigma-Aldrich, Germany, #A9647) in TBS-Tween. Then, the membrane was incubated with the primary antibody (7TM Antibodies, Germany) solution (1:1˙000 in 5% BSA) in overnight at 4° C. The primary antibodies we used are the following:

- SST2 (IHC-grade), Somatostatin Receptor 2 Antibody (#7TM0356N-IC)
- SST5 (IHC-grade), Somatostatin Receptor 5 Antibody (#7TM0359N-IC)

After the incubation, the membrane was recovered, rinsed 3 times in TBS-Tween, and incubated with the horseradish peroxidase (HRP) – labeled secondary antibody (Amersham ECL Rabbit IgG, HRP-linked whole Ab (from donkey); Cytiva, UK, #NA934) solution (1:3˙000 in 5% BSA) for 1 hour at RT. After the incubation, the membrane was rinsed 4 times in TBS-Tween.

To normalize the expression levels of target proteins, the expression of the housekeeping protein glyceraldehyde 3-phosphate dehydrogenase (GAPDH) was assessed. Detection was performed by incubating the membrane with an HRP-conjugated primary monoclonal antibody (Santa Cruz Biotechnology, USA, #sc-365062) diluted 1:1˙000 in 5% BSA. The membrane was incubated overnight at 4°C, followed by four washes with PBS-Tween 0.1% before signal development.

To develop the membrane, an enhanced chemiluminescence (ECL) solution (SuperSignal West Pico PLUS Chemiluminescent Substrate; Thermo Fisher Scientific, USA, #34580) was prepared by mixing the two reagents (Stable Peroxide and Luminol Enhancer) in a 1:1 ratio. The membrane was exposed to the solution and incubated protected from light at RT for 5 minutes. The signal revelation was performed using the ChemiDoc MP Imaging System (Bio-Rad, USA, #12003154).

When necessary, the antibody incubation and membrane development procedure was repeated after treating the membrane with a specific stripping buffer (Restore Western Blot Stripping Buffer; Thermo Fisher Scientific, USA, #21059) at 37° C.

3.4 Immunofluorescence

The immunofluorescence assay was applied to identify the expression and localization of SSTRs in our experimental models.

Cells were seeded in 6-well plates (Corning Costar, USA, #3516) in which a glass slide (Biosigma, Italy, #VBS634) was previously positioned in each well, and incubated overnight. Cells were then rinsed with DPBS containing calcium and magnesium (Biowest, USA, #X0520) which helped prevent cell detachment. Cell fixation was carried out with 4% paraformaldehyde (Sigma-Aldrich, Germany, #158127), incubating the samples for 20 minutes at RT. Cells were then rinsed 3 times with PBS.

The anti-SSTRs primary antibody (7TM Antibodies, Germany; see Paragraph 3.3) solutions were prepared by diluting the stock solutions in a milk solution (5% in TBS-Tween 0,1%; see Paragraph 3.3) in a 1:60 ratio. The solutions were pipetted on a piece of parafilm (Pechiney Plastic Packaging, France, # HS234526A) to form single drops. The slides were removed from the plate with the aid of a scalpel and were placed sample-side down in contact with the drops of primary antibody solution. To promote the binding of the primary antibody to its target, the samples were incubated overnight at 4° C. Moist paper was used to maintain humidity conditions during incubation. After the incubation, the slides were repositioned in the 6-well plate and rinsed 3 times with TBS-Tween 0.1% (see Paragraph 3.3) in agitation for 5 minutes each.

The secondary antibody solution (Alexa Fluor 488 goat anti-rabbit IgG Fc; Invitrogen, Thermo Fisher Scientific, USA, #A78953) was prepared by diluting the stock solution in the milk solution with a 1:100 ratio. Maintaining a dark environment, the samples were placed in contact to the secondary antibody solution, similarly to the primary antibody, and incubated for ~ 1.5 hours at RT. After the incubation, the slides were again repositioned in the wells of the 6-well plate and rinsed 3 times with TBS-Tween 0.1% in agitation for 5 minutes each.

The slides were mounted on labeled coverslips (Biosigma, Italy, #VBS653/A) with the aid of a mounting medium containing DAPI (4',6-diamidino-2-phenylindole) DNA stain (ProLong Gold antifade reagent with DAPI; Invitrogen, Thermo Fisher Scientific, USA, #P36931) and incubated with the same procedure carried out for the antibodies, to counterstain the nuclei of the cells. The incubation was performed at RT in the dark for 24 hours. Finally, the slides were observed under a fluorescence microscope (Leica DM6 B; Leica Microsystems, Germany, #630-3466) to visualize the target proteins. Photographs were acquired and analyzed with the ImageJ software (National Institutes of Health, USA).

3.5 Quantitative Reverse Transcription PCR (RT-qPCR) Assay

The quantitative reverse transcription PCR (RT-qPCR) technique was applied to validate our experimental models in terms of expression of different SSTRs subtypes. To produce the cell pellets for the analysis, cells were seeded in 10 cm^2 dishes in amounts ranging from 500˙000 to $1x10^6$ per dish and maintained at standard incubator conditions to promote cell division. At ~ 72 hours after plating, cells were rinsed with 5 mL PBS. After that, another 5 mL PBS were added, and cells were collected using a cell scraper and deposited into 15 mL test tubes. Cells were counted and then an amount corresponding to a maximum of $3x10^6$ cells was centrifuged at 13˙400 rpm for 5 minutes at room temperature (RT). The supernatants were discarded; the pellets were resuspended in 1 mL PBS and then transferred into 1.5 mL test tubes. Cells were centrifuged again at 13˙400 rpm for 5 minutes at RT. Finally, the supernatant was aspired, and the dry pellets were frozen at -80° C until the time of analysis.

RNA extraction from cell pellets was performed either with the RNeasy Mini Kit (QIAGEN, Holland, #74104) or the RNeasy Micro Kit (QIAGEN, Holland, #74004) depending on the number of total cells, according to the manufacturer’s instructions. RNA concentration and quality was determined by measuring the absorbance using the Nanodrop 2˙000 (Thermo Fisher Scientific, USA, #ND-2000). To assess RNA quality, an A260/280 ratio of 1.8 – 2.2 and an A260/230 ratio of 2.0 – 2.2 were considered in this study. RNA was stored at -80 °C until the time of analysis.

The reverse transcription and cDNA generation was performed with the High-Capacity RNA-to-cDNA Kit (Thermo Fisher Scientific, USA, #4387406) following the manufacturer’s instructions, with 500 ng of total RNA input. The reaction was carried out with the Eppendorf Mastercycler X50i (Eppendorf, Germany, #6301000012) at 37° C for 60 minutes, 95° C for 5 minutes, and held at 4° C. The cDNA samples produced were stored at -20° C until further use.

To analyze gene expression levels of specific genes of interest, the TaqMan Real Time PCR Assays (Thermo Fisher Scientific, USA) were used on QuantStudio 7 Flex (Thermo Fisher Scientific, USA, #4485701), with specific TaqMan probes (Thermo Fisher Scientific, USA).

The following TaqMan Gene Expression Assays were used:

- *SSTR2*: Hs00265624_s1
- *SSTR3*: Hs00265633_s1
- *SSTR5*: Hs00265647_s1
- *Sstr2*: Rn01464950_g1

- *Sstr3*: Rn02134439_s1
- *Sstr5*: Rn02535169_s1
- *TBP*: Hs00427620_m1
- *B2m*: Rn00560865_m1

Each reaction had a final volume of 10 µL, consisting of 5 µL of TaqMan Fast Advanced Master Mix (Thermo Fisher Scientific, USA, #4444557), 2 µL cDNA template, 0.5 µl TaqMan assay, and 2.5 µL nuclease-free water (Sigma-Aldrich, USA, #W4502). qPCR was performed with an initial enzyme activation step at 95°C for 20 seconds, followed by 40 cycles of denaturation at 95°C for 1 second and annealing/extension at 60°C for 20 seconds.

All experiments were performed in three independent biological replicates, each analyzed in technical triplicates. No-RT controls were included to exclude genomic DNA contamination.

Data analysis was performed on Microsoft Excel (Microsoft 365) by normalizing the data to endogenous reference genes (TATA-binding protein (*TBP*) for NT-3 cells, β-2-microglobulin (*B2m*) for AtT-20 cells), and fold changes were determined by using the $2^{(-\Delta\Delta Ct)}$ method.

3.6 WST-1 Viability Assay

The WST-1 viability assay was used to measure cell viability following treatment. The WST-1 reagent is composed of a tetrazolium salt with a slightly red color that is cleaved by the mitochondrial succinate-tetrazolium reductase system of metabolically active cells to produce a dark red formazan dye, which is soluble in aqueous solutions. This colorimetric reaction is directly measurable using a scanning multi-well spectrophotometer, thus allowing to quantify the amount of living cells in the solution, that is directly proportional to the color intensity.

Cells were seeded in a flat-bottom 96-well plate (Corning Costar, USA, #10695951) in different amounts depending on the cell line (3˙500 cells/well for AtT-20 cells; 10˙000 cells/well for NT-3 cells; 4˙000 cells/well for SaOS-2 cells; 1˙000 cells/well for HFF cells; 15˙000 cells/well for NT-18LM and NT-18P cells) in a final volume of 100 µL/well, and a blank control consisting of culture medium was added.

Cells were incubated at standard incubator conditions. Drugs were administered to the cells after adhesion at defined final concentrations. A non-treated (NT) control was added for each experiment. A biological triplicate was reproduced for each condition.

The WST-1 assay was performed at different time points after treatment depending on the cell line (72 hours for AtT-20 cells; 5 days for NT-3 cells; 48 hours for SaOS-2, HFF, NT-18LM, and NT-18P cells). 10 µL/well of the WST-1 reagent (Cell Proliferation Reagent WST-1; Roche, Switzerland, #96992) were added to each well, then the cells were incubated again at standard conditions to allow the reaction to occur.

At different time points after the addition of the reagent, depending on the cell line (3 hours for AtT-20 cells, 4 hours for NT-3, NT-18P, NT-18LM and HFF cells), the OD at 450 nm corrected to 690 nm was measured for each well with a microplate reader (Fluostar Omega; BMG Labtech, Germany, #KBS-0024-002). Data analysis was carried out by normalizing the data for the values of the blank controls and was performed with Microsoft Excel (Microsoft 365) and GraphPad Prism ver. 8.0.2 for Windows (GraphPad Software, USA).

3.7 cAMP-Glo Assay

The cAMP-Glo assay was performed to measure variations in the levels of intracellular cyclic AMP (cAMP) in AtT-20 cells subjected to treatment. The cAMP-Glo assay is a bioluminescent test that monitors cAMP production in cells in response to the effects of an agonist or test compound on G protein-coupled receptors (GPCRs), which couple with adenylate cyclase and alter intracellular cAMP levels. The assay is based on the principle that cAMP stimulates protein kinase A (PKA) holoenzyme activity, decreasing available ATP and leading to decreased light production in a coupled luciferase reaction. Thus, there is a reciprocal relationship between cAMP concentration and the light output observed.

Specifically, this assay was applied to evaluate the ability of the novel SSAs to reduce intracellular cAMP levels in cells subjected to treatment.

AtT-20 cells were seeded in white-walled 96-well plates (Corning Costar, USA, #3610) in the amount of 3˙500 cells/well (final volume per well: 100 µL). Cells were incubated at standard incubator conditions for 24 hours to allow cell adhesion. Drugs were then administered to the cells by replacing the culture medium with fresh complete medium supplemented with the test compounds. The samples were incubated for 72 hours at standard incubator conditions before performing the assay. A non-treated control (NT) was added for each experiment. For each drug concentration and for the NT control a biological triplicate was reproduced.

Before performing the assay, the samples were induced with 10 µM forskolin (Sigma-Aldrich, USA, #93049) in induction buffer (IB), which had the following composition: serum-free culture medium, 500 µM isobutyl-1-methylxanthine (IBMX; Sigma-Aldrich, USA, #I7018), 100 µM 4-(3-butoxy-4-methoxybenzyl) imidazolidone (Ro 20-1724; Sigma-Aldrich, USA, #B8279). Forskolin is a compound that is able to activate the enzyme adenylyl cyclase (AC) and increase the intracellular levels of cAMP. IBMX and Ro 20-1724 are broad-range phosphodiesterase inhibitors able to inhibit cAMP hydrolysis. The induction was performed 3 hours prior to performing the assay. Forskolin induction timing was determined empirically through optimization.

The assay was performed by using a specific cAMP-Glo Assay kit (Promega Corporation, USA #V1501) following the manufacturer's instructions. Briefly, the cells were first lysed by adding a suitable lysis buffer, then a proper detection solution containing PKA was added and after a brief incubation (~ 20 minutes) at RT a specific reagent for the luciferase reaction was added. After another incubation (~ 10 minutes) at RT, the luminescent signal was measured directly with a microplate-reading luminometer (Fluostar Omega; BMG Labtech, Germany, #KBS-0024-002) with an integration time of 0.5 s per well and standard gain settings. Data analysis was performed with Microsoft Excel (Microsoft 365) and GraphPad Prism ver. 8.0.2 for Windows (GraphPad Software, USA).

3.8 CellTiter-Glo 3D Viability Assay

The CellTiter-Glo 3D viability assay was used to determine the level of cell viability in AtT-20 and NT-3 3D cultures subjected to drug treatment. The assay kit (Promega Corporation, USA, #G9681) provides a single ready-to-use reagent (CellTiter-Glo 3D Reagent) that is added directly to cells cultured in complete or serum-free medium, generating their lysis and the release of ATP molecules into the medium. The presence of luciferin and the luciferase enzyme in the reagent triggers a luminescence reaction for which the light intensity is directly proportional to the amount of ATP in the sample. Since the ATP released is in turn proportional to the number of live cells, the measurement of the luminescence generated allows to reliably estimate the level of cell viability in the sample of interest.

Cells were seeded in opaque-walled round-bottom 96-well Ultra Low Attachment plates (Corning Costar, USA, #4515) or in the Akura PLUS Hanging Drop System (InSphero, Switzerland, #CS-PF24) in different amounts depending on the cell line (750 cells/well for AtT-20 cells, 2˙000 cells/well for NT-3 cells). Opaque vessels were used for this assay in order to avoid dispersion and contamination of the luminescent signal generated by the individual samples. In the case of the Ultra Low Attachment plates, the vessels were centrifuged after seeding with a ROTINA 380 R centrifuge (Hettich, Germany, #472265) at 500 rcf for 20 minutes at room temperature (RT). Cells were incubated at standard incubator conditions for 5 days to obtain spheroids of optimal size for the treatment. After the incubation, drugs were administered to the cells by discarding the culture medium and adding the equivalent of fresh medium supplemented with drugs at the desired final concentration. Since NT-3 cells required a longer exposure time to the treatment, the culture medium containing drugs was refreshed every 72 hours. A non-treated control (NT) was added for each experiment.

For each drug concentration and for the NT control a biological triplicate was reproduced.

The assay was performed by using a specific CellTiter-Glo 3D kit following the manufacturer’s instructions. Briefly, at different time-points after treatment depending on the cell line (72 hours for AtT-20 cells, 14 days for NT-3 cells), the plates and the CellTiter-Glo 3D Reagent were equilibrated at RT (the latter by placing it in a 22° C water bath) for ~ 30 minutes. Then, a volume of reagent equal to the volume of cell culture medium present in each well was added after thorough mixing. The plates were then incubated at RT for 5 minutes in agitation on a rocker (Thermo-Lab 711; Thermo-Lab, Italy, #AS29970012) to induce cell lysis, and then for additional 25 minutes without agitation to stabilize the luminescent signal.

Finally, the luminescent signal was recorded with a microplate-reading luminometer (Fluostar Omega; BMG Labtech, Germany, #KBS-0024-002) with an integration time of 0.5 s per well and standard gain settings. Data analysis was performed with Microsoft Excel (Microsoft 365) and GraphPad Prism ver. 8.0.2 for Windows (GraphPad Software, USA).

3.9 Enzyme-Linked Immunosorbent Assay (ELISA)

The Enzyme-Linked Immunosorbent Assay (ELISA) technique was applied to detect and quantify the presence of secreted hormones in the conditioned media of cells exposed to treatment, for both two-dimensional and three-dimensional cultures. Specifically, this assay was performed to measure the levels of ACTH secreted by AtT-20 cells and insulin secreted by NT-3 cells.

For 2D cultures, cells were seeded in 24-well plates (Corning Costar, USA, #CLS3527) at a density of 20˙000 cells/well for both cell lines. The day after seeding, cells were treated with the drugs at defined final concentrations (5, 10, 50, and 100 nM) in complete culture medium for the AtT-20 cells and serum-free medium for the NT-3 cells. A non-treated control (NT) was included, and a biological duplicate was reproduced for each condition.

At different time-points after treatment depending on the cell line (72 hours for AtT-20 cells, 5 days for NT-3 cells) cell supernatants were collected and deposited into 1.5 mL test tubes and centrifuged at 13˙400 rpm for 5 minutes at RT to remove any cell debris. The samples were then stored at -80 °C until the time of analysis.

For 3D cultures, the same seeding and treatment procedure described in Paragraph 3.8 was applied, with the only variation being that clear-walled round-bottom 96-well Ultra Low Attachment plates (Corning, USA, #7007) were used as vessels.

The ELISA assay was performed with the Sandwich ELISA setup. Specific ELISA kits were employed according to the manufacturers’ instructions. The kits used were as follows:

- Abcam Mouse/Rat ACTH SimpleStep ELISA Kit (Abcam, UK, #ab263880); sensitivity: 6 pg/mL; detection range: 7,81 pg/mL – 500 pg/mL;
- Human Insulin (INS) ELISA Kit (Elabscience, USA, #E-EL-h2665); sensitivity: 0.47 µIU/mL; detection range: 0.78-50 µIU/mL.

To fall within the detection range of the kit, the supernatants from AtT-20 cells were diluted at a 1:100 ratio for 2D cultures and 1:500 for 3D cultures. At the end of the experiments, the optical density (OD) at 450 nm was measured for each well of the plates with a microplate reader (Fluostar Omega; BMG Labtech, Germany, #KBS-0024-002). Data analysis was performed with Microsoft Excel (Microsoft 365) and GraphPad Prism ver. 8.0.2 for Windows (GraphPad Software, USA). ACTH and insulin secretion were assessed without normalization to cell number or viability, since an optimal normalization method could not be determined.

3.10 DNA Extraction and Purification for C-Circles Quantification

To assess ALT activity in PanNET cell lines, DNA was extracted from both cell pellet samples and supernatants of NT-18P and NT-18LM cells. The control cell line SaOS-2 was also included in the analyses.

Genomic DNA purification from cell pellets was performed by adapting the protocol described by NJ Robinson and WP Schiemann in 2023 (Robinson et al., 2023). A lysis buffer, referred to as Quick C-circle Preparation (QCP), was prepared with the following 1X composition: 10 mM Tris-HCl (pH 8.5), 50 mM KCl (Sigma-Aldrich, USA, #P9541), 2 mM $MgCl_2$ (Sigma-Aldrich, Germany, #930970), 0.5% (v/v) NP-40 (Sigma-Aldrich, Germany, #542334), 0.5% (v/v) Tween-20, and ddH_2O. The QCP lysis buffer was pre-warmed to 56° C in a heat block and subsequently supplemented with Proteinase K (Roche, Switzerland, #RPROTK-RO) at a 1:20 ratio. Cell pellets containing 200˙000 cells were resuspended in 50 µL of QCP lysis buffer each and briefly centrifuged for 15 seconds at 2˙000 RPM at room temperature. The suspension was then incubated at 56° C for 1 hour in a heat block, followed by a 20-minute incubation at 70° C to inactivate the protease. Samples were subsequently cooled to room temperature, briefly centrifuged at 2˙000 RPM for 15 seconds to collect any evaporated liquid, and either used immediately for DNA quantification or stored at -80° C until further use.

Cell-free DNA was purified from cell culture supernatants using the QIAamp ccfDNA/RNA Kit (QIAGEN, Holland, #55184). Samples were obtained by seeding an amount of 400˙000 cells/well and collecting the supernatants at a 48-hour time point post-seeding. The samples were centrifuged at 13˙000 RPM for 15 minutes to remove cellular debris. DNA purification was then performed according to the manufacturer's instructions. Briefly, 1 mL of each supernatant sample was mixed with

300 µL of Buffer RPL, vortexed for 5 seconds, and incubated at room temperature for 3 minutes to lyse extracellular vesicles and denature proteins. Subsequently, 100 µL of Buffer RPP was added to each solution, followed by vortexing for 20 seconds and incubation on ice for 3 minutes. Samples were then centrifuged at 3˙000 RCF for 10 minutes at 4° C to pellet the proteins. The resulting supernatants were collected and mixed with an equal volume of ice-cold isopropanol (Sigma-Aldrich, Germany, #190764). The solutions were then loaded onto RNeasy Midi columns and centrifuged at 5˙000 RCF for 1 minute at room temperature. Washing steps were performed using 4 mL of Buffer RWT per sample, followed by centrifugation at 5˙000 RCF for 1 minute at room temperature, and then 2.5 mL of Buffer RPE per sample, followed by a 5-minute centrifugation under the same conditions. DNA elution was performed by adding 200 µL of RNase-free H_2O, incubating for 1 minute at room temperature, and centrifuging at maximum speed for 1 minute at room temperature.

Finally, a clean-up step was performed to improve the purity of the extracted DNA. Each eluate was mixed with 200 µL of Buffer RPL and 800 µL of 96–100% ethanol (EtOH; Carlo Erba Reagents, Italy, #414607). The mixtures were then loaded onto RNeasy MinElute columns in 700 µL increments and centrifuged at 10˙000 RPM for 15 seconds at room temperature. Washing steps were carried out using 500 µL of Buffer RPE and 500 µL of 80% ethanol, each followed by centrifugation under the same conditions. Following an additional centrifugation step at maximum speed for 5 minutes with open tube caps to allow evaporation of residual alcohol, DNA was eluted using 14 µL of RNase-free H_2O and centrifuged for 1 minute at maximum speed at room temperature. The resulting samples were either used immediately for quantitative PCR experiments or stored at -80° C for future use.

3.11 Quantification of Purified DNA

Quantification of genomic DNA purified from cell pellet samples was performed using the QuantiFluor ONE dsDNA System kit (Promega Corporation, USA, #E4871) following the manufacturer's instructions. To generate a standard calibration curve, a serial dilution of the kit's internal standard (400 ng/µL) was prepared to obtain dsDNA standards at known concentrations: 400, 200, 50, 12.5, 3.1, 0.8, and 0.2 ng/µL. In a black 96-well fluorescence assay plate, 1 µL of each standard and sample was added to 200 µL of QuantiFluor ONE dsDNA dye. Each analyte was tested in technical duplicate, and a blank control containing 1 µL of TE buffer 1X was included in the assay to enable normalization of raw data. The plate was incubated for 5 minutes on a shaker, and fluorescence was then measured using a plate reader set to an excitation wavelength of 504 nm and an emission wavelength of 531 nm. Raw data were analyzed using Microsoft Excel (Microsoft 365).

Cell-free DNA samples purified from cell culture supernatants using the QIAamp ccfDNA/RNA kit were quantified directly by quantitative PCR, as recommended by the manufacturer.

3.12 Rolling Circle Amplification (RCA) of Extrachromosomal Circular DNA

As described in the literature by Henson et al. (2009), the rolling circle amplification (RCA) mechanism was employed to amplify extrachromosomal circular DNA from previously purified samples, following the methodology outlined by NJ Robinson and WP Schiemann in 2023. This methodology involves the use of Φ29 DNA polymerase, an enzyme derived from the *Bacillus subtilis* phage Φ29, which enables isothermal amplification of the target DNA.

For initial validation experiments, both Φ29-amplified (Φ29+) and non-amplified (Φ29−) reactions were performed for each sample to confirm assay specificity. In subsequent experiments, Φ29 polymerase was used for C-circle enrichment prior to qPCR analysis.

First, the master mix for Φ29 DNA polymerase was prepared with the following composition (2.16X): 2.16X Φ29 reaction buffer (New England Biolabs, USA, #B0269S); 432 µg/mL BSA (New England Biolabs, USA, #B9200S); 0.216% (v/v) Tween 20 in ddH_2O; 2.16 mM of each dNTP (dATP, dGTP, dTTP, dCTP; New England Biolabs, USA, #N0447S); 8.65 mM dithiothreitol (DTT; Sigma-Aldrich, Germany, #D9779); and ddH_2O. DNA samples were thawed and vortexed at 2˙000 RPM for 15 seconds. To reduce the amount of QCP lysis buffer in the solutions – which could impair amplification efficiency – each sample was diluted 1:10 in 10 mM Tris buffer (pH 7.6). The Φ29 master mix was aliquoted into 0.2 mL tubes at 9.25 µL per reaction. To each tube, 0.75 µL of Φ29 DNA polymerase (New England Biolabs, USA, #M0269S) was added and gently mixed. In initial validation experiments, for each sample a negative control reaction (Φ29−) was also prepared by adding 0.75 µL of ddH_2O to the master mix instead of the enzyme. Finally, 10 µL of the diluted DNA samples were added to both reaction mixes (Φ29+ and Φ29−), and the amplification reaction was carried out using a thermal cycler (QIAquant 96 2plex; QIAGEN, Holland, # 9003001) set to the following temperature profile:

- 30° C, 8 hours (amplification step)
- 70° C, 20 minutes (Φ29 DNA polymerase inactivation)
- 4° C, ∞ (hold)

Following isothermal amplification, the samples were either used immediately for the subsequent quantitative PCR step or stored at −20°C until further use.

3.13 Quantitative Polymerase Chain Reaction (qPCR)

Quantitative PCR was used to assess the abundance of C-circle DNA both in genomic DNA samples amplified by RCA and in cell-free DNA samples purified from cell culture supernatants. The reaction was carried out using the QuantiNova SYBR Green kit (QIAGEN, Holland. #208052), following the manufacturer's instructions. For data normalization and as internal control, the housekeeping gene *GNAT3* was included in the reaction. *GNAT3* encodes the G protein α-gustducin, which is expressed in taste receptor cells, and was chosen as a reference gene for genomic DNA qPCR normalization because it is present as a single copy and is stable in the human genome. The primer sequences used for each target are listed in Table 2.

TARGET	PRIMER SEQUENCE
GNAT3	**Forward:** 5’-GGGAGGAGCATTGGTGACTA-3’
	Reverse: 5’-GGTGACCATGTGATCAGAGC-3’
C-circles	**Forward:** 5′-ACTAATCCCGCCAAAGCAACC-3′
	Reverse: 5’-GTAGCGGTTTTGCTTTTTCATCCT-3’

Table 2. *Primer sequences used for quantitative PCR.*

The reaction master mix was prepared with the following composition: 1X SYBR Green Master Mix, 300 nM Forward Primer, 300 nM Reverse Primer, and ddH$_2$O. The mix was aliquoted at 19 µL per reaction into the wells of a 96-well qPCR plate. Then, 1 µL of target DNA sample was added to each well. In negative controls (No Template Controls, NTCs), 1 µL of ddH$_2$O was added instead of DNA.

After loading, amplification was carried out using the QIAquant 96 2plex thermal cycler (QIAGEN, Holland, #9003001) with the following thermal profile:

- 95° C, 15 minutes (polymerase activation phase)
- 95° C, 15 seconds
- 54° C, 2 minutes 35 cycles (amplification phase)
- 72° C, 1 minute
- 55° C, 1.5 minutes (melt phase)
- 90° C, 1° C/5 seconds

Background fluorescence was subtracted from all reactions before Ct determination. Relative ALT signal was calculated using the $2^{(-\Delta Ct)}$ method, where ΔCt represents the difference between the Ct of the C-circle target and the Ct of *GNAT3*, and is reported as relative normalized abundance.

3.14 Agarose Gel Electrophoresis

To confirm the quality of the DNA amplicons obtained by qPCR, they were visualized on a 2% agarose gel. The gel was prepared by dissolving 1 g of agarose powder (Promega Corporation, USA. #V3121) in 50 mL of 1X Tris-Acetate EDTA (TAE) buffer (40 mM Tris-Acetate, 1 mM EDTA). The solution was heated until the agarose was completely dissolved, then poured into a casting tray to solidify, with the addition of 5 µL of an intercalating dye (SYBR Safe DNA Gel Stain; Invitrogen, Thermo Fisher Scientific, USA, #S33102). A comb was used to form the wells in the gel during the cooling phase.

1 µL of each DNA amplicon was mixed with 6 µL of loading dye (6X TriTrack DNA Loading Dye; Thermo Fisher Scientific, USA, #R1161) and then loaded onto the gel. A molecular weight marker (GeneRuler 100 bp DNA Ladder; Thermo Fisher scientific, USA, #SM0241) was included in the assay. Electrophoresis was carried out at 120 V for approximately 40 minutes. At the end of the run, DNA bands were visualized using a UV transilluminator (ECX-20.M; Euroclone, Italy, #22.7410.92).

3.15 Statistical Analysis

The experiments were performed three times independently (biological replicates), with at least three technical replicates, unless otherwise stated. Statistical analyses were performed using GraphPad Prism ver. 8.0.2 for Windows (GraphPad Software, USA). For experiments comparing multiple treatment groups, one-way ANOVA was applied, followed by Dunnett's post-hoc test to compare each treatment to the control. Data were assumed to meet the assumptions of ANOVA (normality and equal variance). No further correction for multiple testing was applied beyond Dunnett's test. A p-value of < 0.05 was considered statistically significant. Results are presented as mean ± standard deviation (SD).

4. Results

Section 4.1: Characterization of Novel Dual Somatostatin Analogs

To accurately characterize the efficacy of the novel SSAs, different dose ranges were used across the various assays due to differences in assay sensitivity and concentrations empirically optimized in our laboratory to reliably detect biological effects in hormone secretion, cell viability, and intracellular signaling assays.

4.1.1 AtT-20 and NT-3 Cells Express the relevant Somatostatin Receptors

To characterize our cell lines for somatostatin receptor expression, several molecular analyses were performed. The studies focused primarily on SSTR2 and SSTR5 receptors, as they represent the main targets of the experimental peptides.

Protein expression of the two receptors was initially determined by Western blotting. The results indicated a high expression of the SSTR2 receptor in both AtT-20 and NT-3 cell lines, with slightly higher levels observed in AtT-20 cells. Expression of the SSTR5 receptor was detectable in both cell lines (Figure 20).

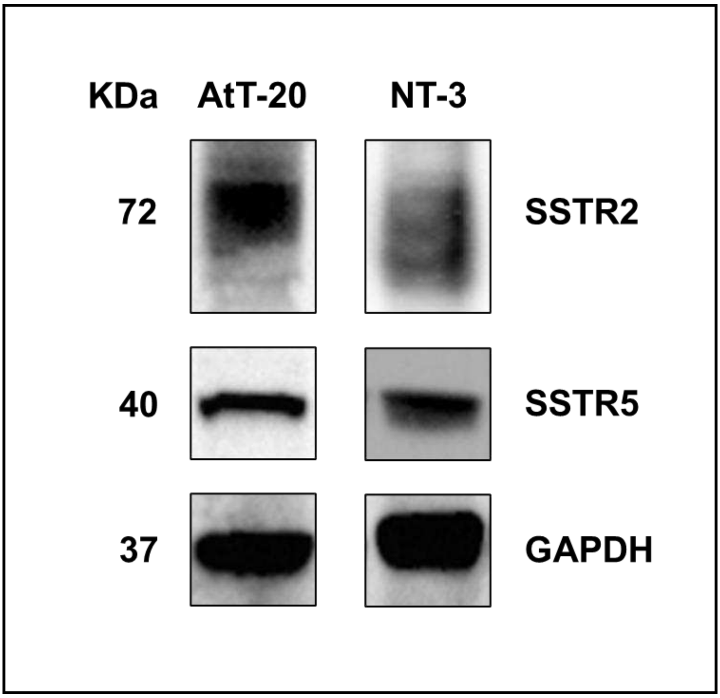

Figure 20. *Western blot analysis of SSTR2 and SSTR5 protein expression in AtT-20 and NT-3 cell models. High SSTR2 expression was detected in the AtT-20 cell line, while a weaker signal was observed in NT-3 cells. SSTR5 was abundantly expressed in both cell lines. GAPDH was used as an internal loading control.*

Protein receptor expression in both cell lines was additionally examined via immunofluorescence. While Western blot analysis indicated robust SSTR2 protein expression in both cell lines, immunofluorescence analysis revealed a stronger membrane-localized SSTR2 signal in AtT-20 cells compared to NT-3 cells, which showed a detectable but less intense staining. This difference may reflect variations in receptor membrane trafficking, epitope accessibility, or cell morphology rather than overall protein abundance (Figure 21).

Detection of SSTR5 using this assay did not yield appreciable results. Immunofluorescence staining was performed without permeabilization, thus primarily detecting membrane-localized receptors. Consequently, the lack of SSTR5 signal may reflect limited antibody performance in immunofluorescence and/or a predominantly intracellular receptor distribution not accessible under the fixation conditions used.

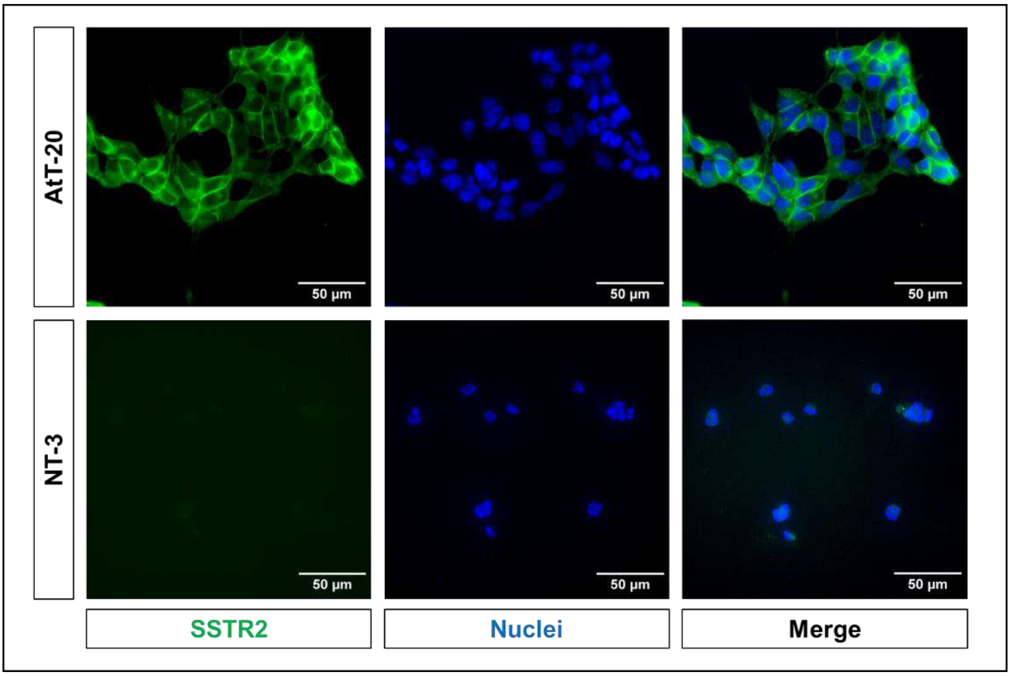

Figure 21. *Immunofluorescence staining of the SSTR2 receptor in AtT-20 (top) and NT-3 (bottom) cell lines. Strong receptor expression was observed in AtT-20 cells, primarily localized at the cell membrane. In NT-3 cells, the observed expression levels were significantly lower.*

Finally, SSTR expression was also detected at the mRNA transcript level using RT-qPCR. The analysis revealed appreciable transcript levels in both cell lines, with particularly high levels of *SSTR5* mRNA (Figure 22).

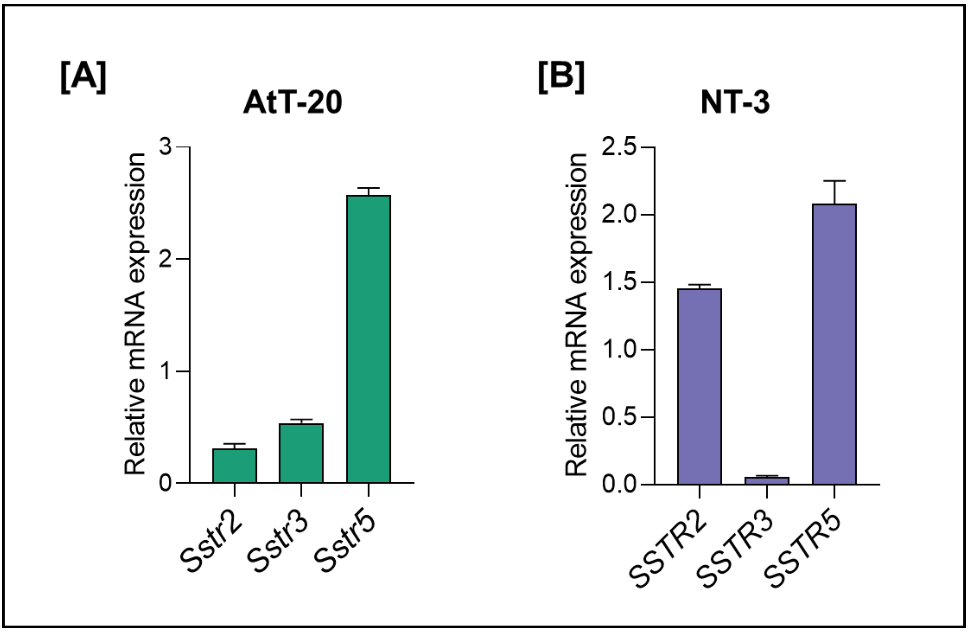

Figure 22. *RT-qPCR analysis of SSTR transcript expression levels. Both AtT-20 (**A**) and NT-3 (**B**) cell lines displayed detectable SSTR2 mRNA expression, with notably high transcript levels of SSTR5 observed in both models.*

In conclusion, these analyses revealed the presence of SSTR2 and SSTR5 at both the transcript and protein levels in our cell models, albeit with marked differences between the two lines. Both models were identified as appropriate for evaluating the efficacy of the novel experimental compounds.

4.1.2 Effect of Novel Somatostatin Analogs on Hormone Secretion in 2D Cell Cultures

The impact of novel somatostatin analogs (SSAs) on hormone secretion represented a key aspect of this study. Treatment with clinically relevant pharmacological concentrations of the test compounds in 2D cultures of AtT-20 and NT-3 cells revealed promising anti-secretory effects.

Modulation of ACTH Secretion in AtT-20 Cells

Preliminary tests performed on 2D cultures of AtT-20 cells showed a stable level of ACTH secretion over time, unaffected by the presence of serum in the culture medium. Consequently, the effect of the experimental peptides was assessed in cells grown in complete medium 72-hour after treatment. Octreotide and pasireotide were used as reference compounds and administered to the cells in parallel with our test agents at identical concentrations.

Among the reference compounds, pasireotide exhibited a more pronounced effect (reduction in ACTH secretion ranging from 59% to 63%; Figure 23B) than octreotide (reduction ranging from 21% to 37%; Figure 23A). Among the test compounds, SMTR-001 (reduction ranging from 53% to 65%, $p \leq 0.001$; Figure 23C) and SMTR-004 (reduction ranging from 59% to 62%, $p \leq 0.0001$; Figure 24F) showed a significant suppressive effect on ACTH secretion, comparable to that of pasireotide. A milder effect was observed for SMTR-002 (11–38% reduction, $p \leq 0.01$; Figure 23D) and SMTR-003 (20–32% reduction, $p \leq 0.05$; Figure 23E). No significant effect was detected for SMTR-005 (Figure 23G).

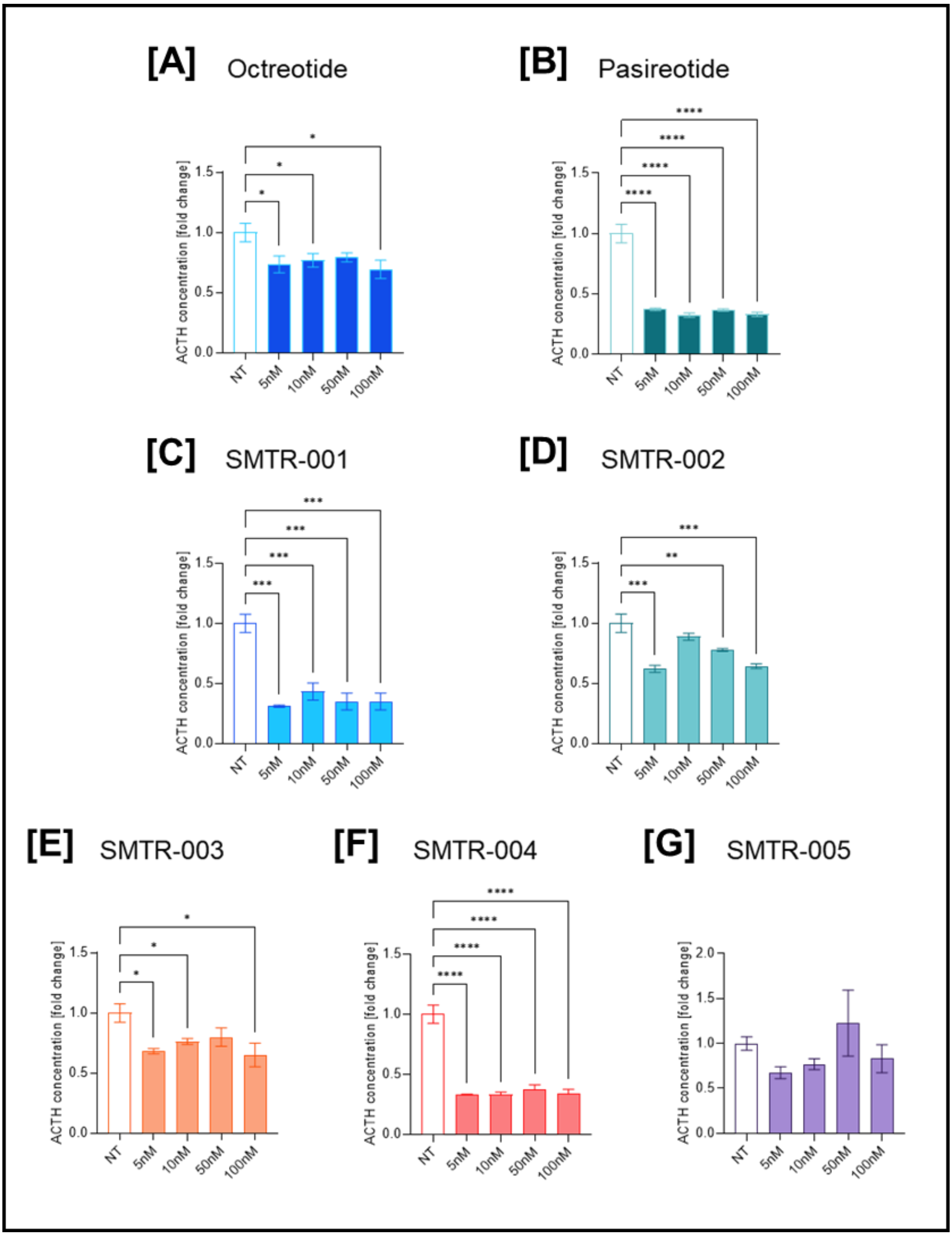
[A] Octreotide
*
*
*
ACTH concentration [fold change]
1.5
1.0
0.5
0.0
NT
5nM
10nM
50nM
100nM
[B] Pasireotide
****
****
****
****
ACTH concentration [fold change]
1.5
1.0
0.5
0.0
NT
5nM
10nM
50nM
100nM
[C] SMTR-001
***
***
***
***
ACTH concentration [fold change]
1.5
1.0
0.5
0.0
NT
5nM
10nM
50nM
100nM
[D] SMTR-002
***
**
***
ACTH concentration [fold change]
1.5
1.0
0.5
0.0
NT
5nM
10nM
50nM
100nM
[E] SMTR-003
*
*
*
ACTH concentration [fold change]
1.5
1.0
0.5
0.0
NT
5nM
10nM
50nM
100nM
[F] SMTR-004
****
****
****
****
ACTH concentration [fold change]
1.5
1.0
0.5
0.0
NT
5nM
10nM
50nM
100nM
[G] SMTR-005
ACTH concentration [fold change]
2.0
1.5
1.0
0.5
0.0
NT
5nM
10nM
50nM
100nM

Figure 23. *ACTH ELISA results on 2D cultures of AtT-20 cells. Among reference compounds, pasireotide (****B****) showed the strongest effect, reducing ACTH secretion by 59–63%, compared to octreotide (****A****), which induced a 21–37% reduction. Among test compounds, significant effects were observed for SMTR-001 (53–65% reduction,* ***C****) and SMTR-004 (59–62% reduction,* ***F****). SMTR-002 (11–38% reduction,* ***D****) and SMTR-003 (20–32% reduction,* ***E****) showed a weaker effect, while SMTR-005 (****G****) did not produce significant results. Data are presented as mean ± standard deviation (SD); * $p \leq 0.05$; ** $p \leq 0.01$; *** $p \leq 0.001$; *** $p \leq 0.0001$.*

Subsequent statistical analysis performed using one-way ANOVA followed by Dunnett's multiple comparison test was conducted to assess the significance of the effects observed at the lower concentrations (5 and 10 nM) of the test compounds in comparison to the reference drugs. SMTR-001 and SMTR-004 showed a highly significant effect relative to octreotide at both tested concentrations (Figure 24B). While no statistical significance was detected when compared to pasireotide, the observed effects of the two test compounds were closely comparable (Figure 24A).

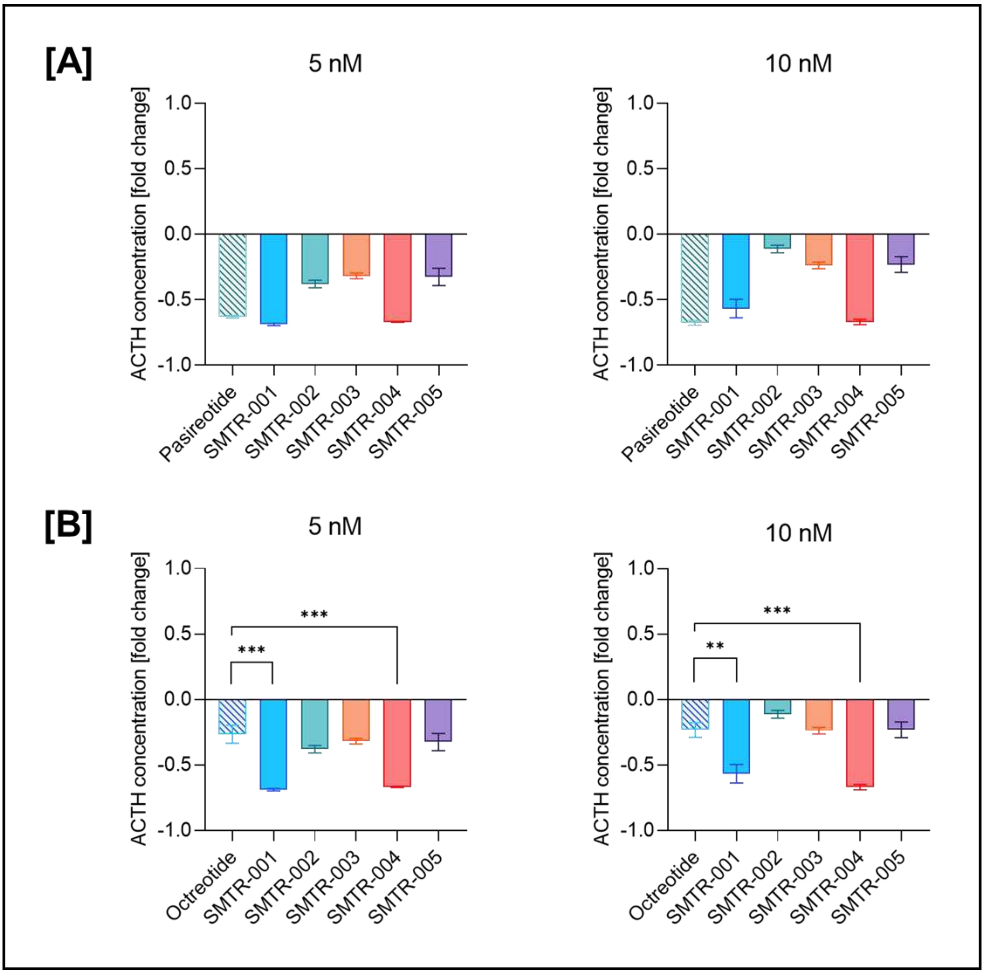

*Figure 24. Direct comparisons between test and reference compounds for their efficacy on ACTH secretion at the lowest concentrations (5 nM, 10 nM). Compared to pasireotide (**A**), no test compound showed significantly greater effects, although SMTR-001 and SMTR-004 displayed very similar levels of ACTH reduction. In contrast, SMTR-001 and SMTR-004 showed significantly stronger effects than octreotide (**B**) at both 5 nM* ($p \leq 0.001$) *and 10 nM* ($p \leq 0.01$ *and* $p \leq 0.001$*, respectively). Data are presented as mean ± standard deviation (SD); *** $p \leq 0.01$*; **** $p \leq 0.001$*; ***** $p \leq 0.0001$.

Modulation of Insulin Secretion in NT-3 Cells

Similarly to the AtT-20 cells, preliminary tests on NT-3 cells confirmed their ability to secrete measurable levels of insulin. The ability of the novel SSAs to suppress hormone secretion was therefore tested in 2D cell cultures under the same treatment conditions used for AtT-20 cells. Since NT-3 cells exhibit a significantly longer doubling time compared to AtT-20 cells, a post-treatment time point of 5 days was selected.

In this case, octreotide exhibited a more pronounced antisecretory effect (reduction ranging from 78% to 99%, $p \leq 0.0001$; Figure 25A) compared to pasireotide (reduction ranging from 52% to 57%, $p \leq 0.0001$; Figure 25B). Among the test compounds, SMTR-001 (78-88% reduction, $p \leq 0.0001$; Figure 25C), SMTR-002 (65-89% reduction, $p \leq 0.0001$; Figure 25D), SMTR-004 (86-99% reduction, $p \leq 0.0001$; Figure 25F), and SMTR-005 (78-99% reduction, $p \leq 0.0001$; Figure 25G) demonstrated antisecretory effects comparable to those of octreotide. In contrast, SMTR-003 (Figure 25E) displayed a lower efficacy (reduction ranging from 45% to 65%, $p \leq 0.0001$), similar to that of pasireotide.

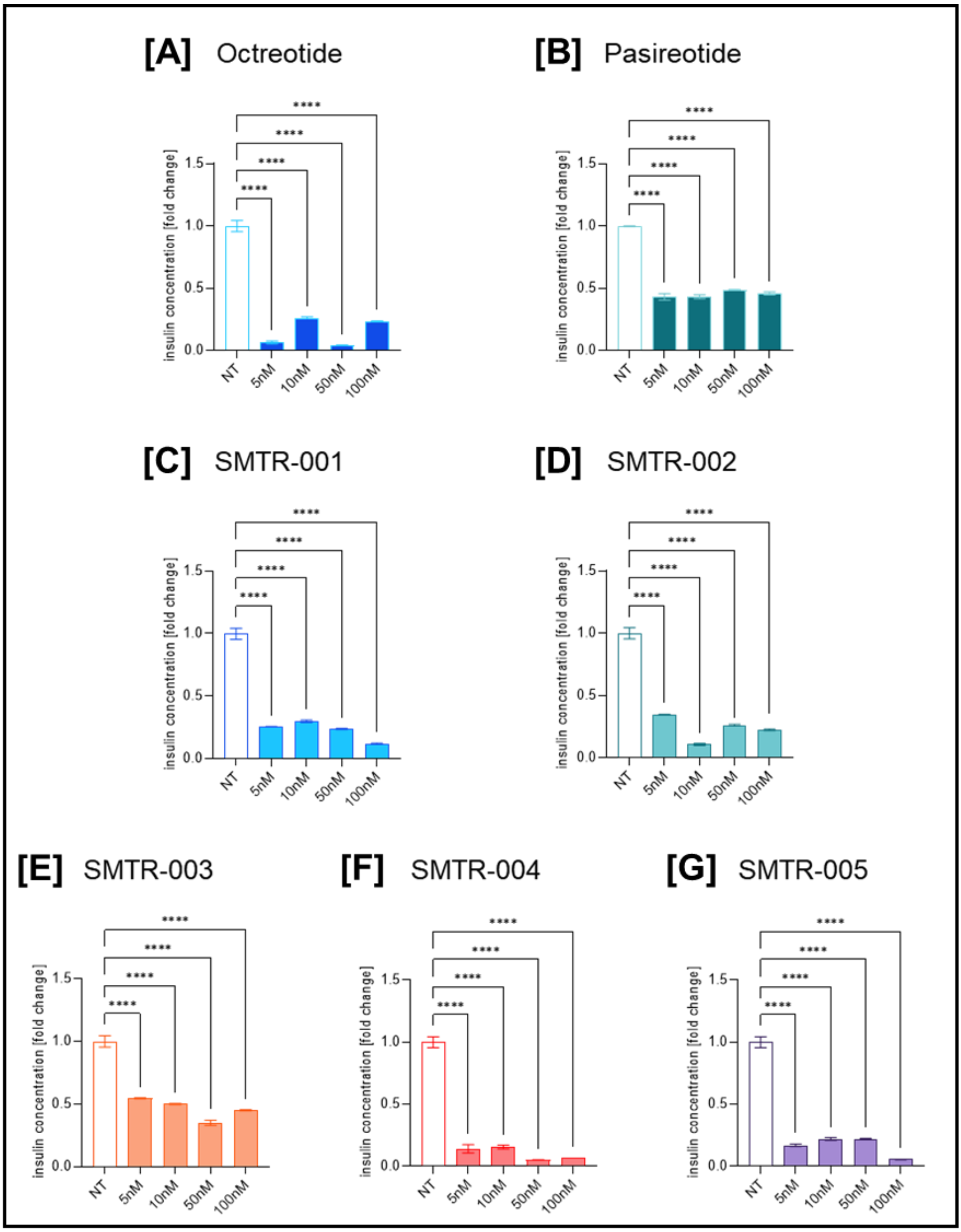

Figure 25. *Insulin ELISA results on 2D cultures of NT-3 cells. Among reference compounds, octreotide showed a stronger antisecretory effect (78–99% reduction,* ***A****) compared to pasireotide (52–57% reduction,* ***B****). Among test compounds, SMTR-001 (78–88%,* ***C****), SMTR-002 (65–89%,* ***D****), SMTR-004 (86–99%,* ***F****), and SMTR-005 (78–99%,* ***G****) demonstrated high efficacy, comparable to octreotide. SMTR-003 showed a more limited effect (45–65% reduction,* ***E****), closer to that of pasireotide. Data are presented as mean ± standard deviation (SD); **** $p \leq 0.0001$.*

As done previously, a statistical analysis performed using one-way ANOVA followed by Dunnett’s multiple comparison test was conducted to compare the effects of the test compounds at the lowest concentrations with those of the reference peptides. A significantly greater reduction in insulin secretion was observed for most experimental peptides (SMTR-001, SMTR-002, SMTR-004, and SMTR-005) at both concentrations when compared to pasireotide (Figure 26A). Notably, SMTR-002, SMTR-004, and SMTR-005 exhibited a superior effect also in comparison to octreotide (Figure 26B) at the concentration of 10 nM.

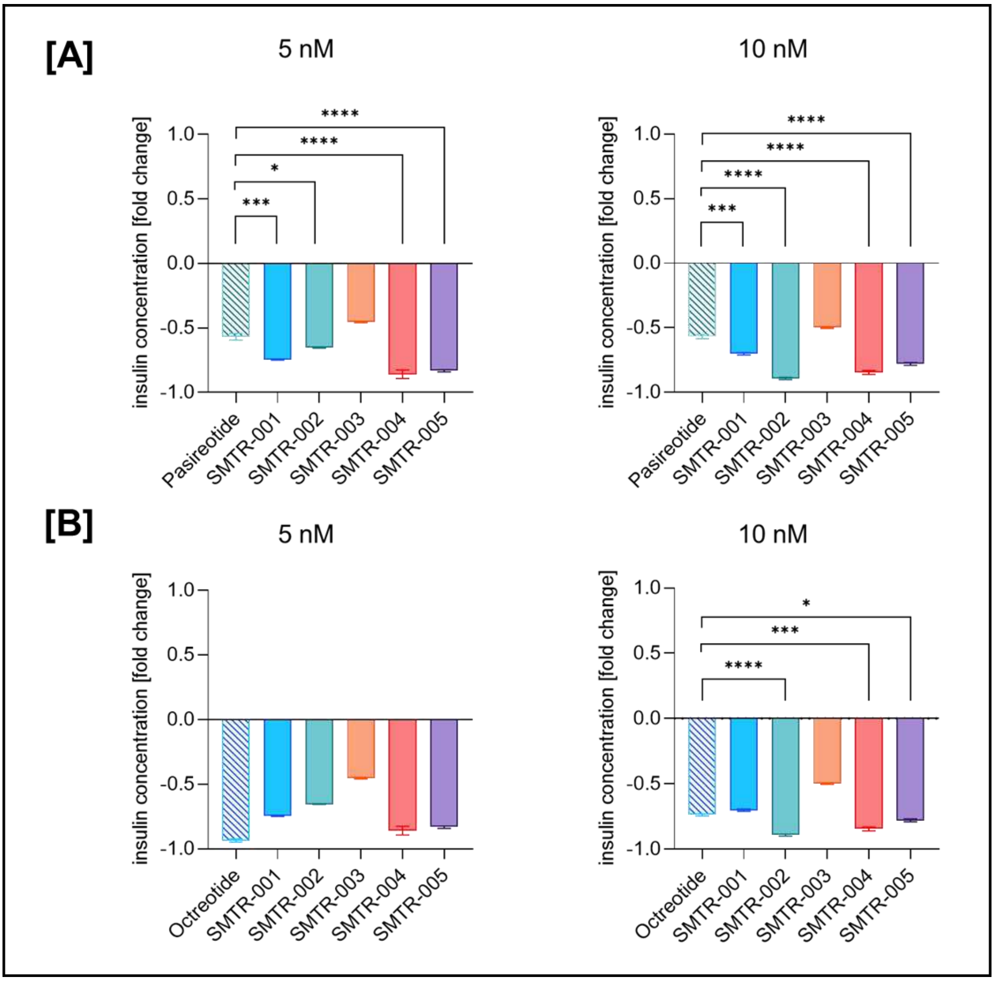

Figure 26. *Direct comparisons between test and reference compounds for their efficacy in inhibiting insulin secretion at the lowest concentrations (5 nM, 10 nM). Compared to pasireotide (**A**), SMTR-001, SMTR-002, SMTR-004, and SMTR-005 showed significantly greater antisecretory effects at both concentrations. In comparison to octreotide (**B**), SMTR-002, SMTR-004, and SMTR-005 exhibited higher efficacy at 10 nM. Data are presented as mean ± standard deviation (SD); * $p \leq 0.05$; ** $p \leq 0.01$; *** $p \leq 0.001$; **** $p \leq 0.0001$.*

4.1.3 Effect of Novel Somatostatin Analogs on Cell Proliferation in 2D Cell Cultures

The effect on cell proliferation represents another important parameter for evaluating the efficacy of novel somatostatin analogs. For this reason, the cytostatic effect of our test compounds was assessed in 2D cultures of our NET cell models, using clinically relevant pharmacological concentrations.

Effects of SSAs on the proliferation of AtT-20 in 2D cultures

2D cell cultures of AtT-20 cells were incubated with increasing concentrations (1 nM, 2.5 nM, 5 nM, 10 nM, and 50 nM) of both the test compounds and the reference peptides. Cell proliferation levels were then assessed using the WST-1 colorimetric assay at a 72-hour post-treatment time point.
Among the reference compounds, pasireotide exhibited a greater reduction in WST-1 signal, consistent with reduced cell proliferation, although only at the highest concentrations (maximum reduction in WST-1 signal ranging from 20% to 27%, $p \leq 0.01$; Figure 27B), compared to octreotide (maximum reduction between 23% and 24%, $p \leq 0.01$; Figure 27A). Among the test compounds, SMTR-002 (maximum reduction in WST-1 signal between 27% and 53%, $p \leq 0.0001$; Figure 27D), SMTR-003 (30% to 48%, $p \leq 0.0001$; Figure 27E), and SMTR-004 (24% to 27%, $p \leq 0.0001$; Figure 27F) showed a significant and consistent reduction in WST-1 signal across different concentrations, comparable to or greater than that of pasireotide. A weaker effect was observed for SMTR-001, which induced a notable reduction only at the 10 nM concentration (37% reduction, $p \leq 0.0001$; Figure 27C), and for SMTR-005, which showed a relevant effect at 10 and 50 nM (36% and 28% reduction, respectively; $p \leq 0.0001$; Figure 27G). No visible cytotoxicity or cell detachment was observed for any of the tested compounds.

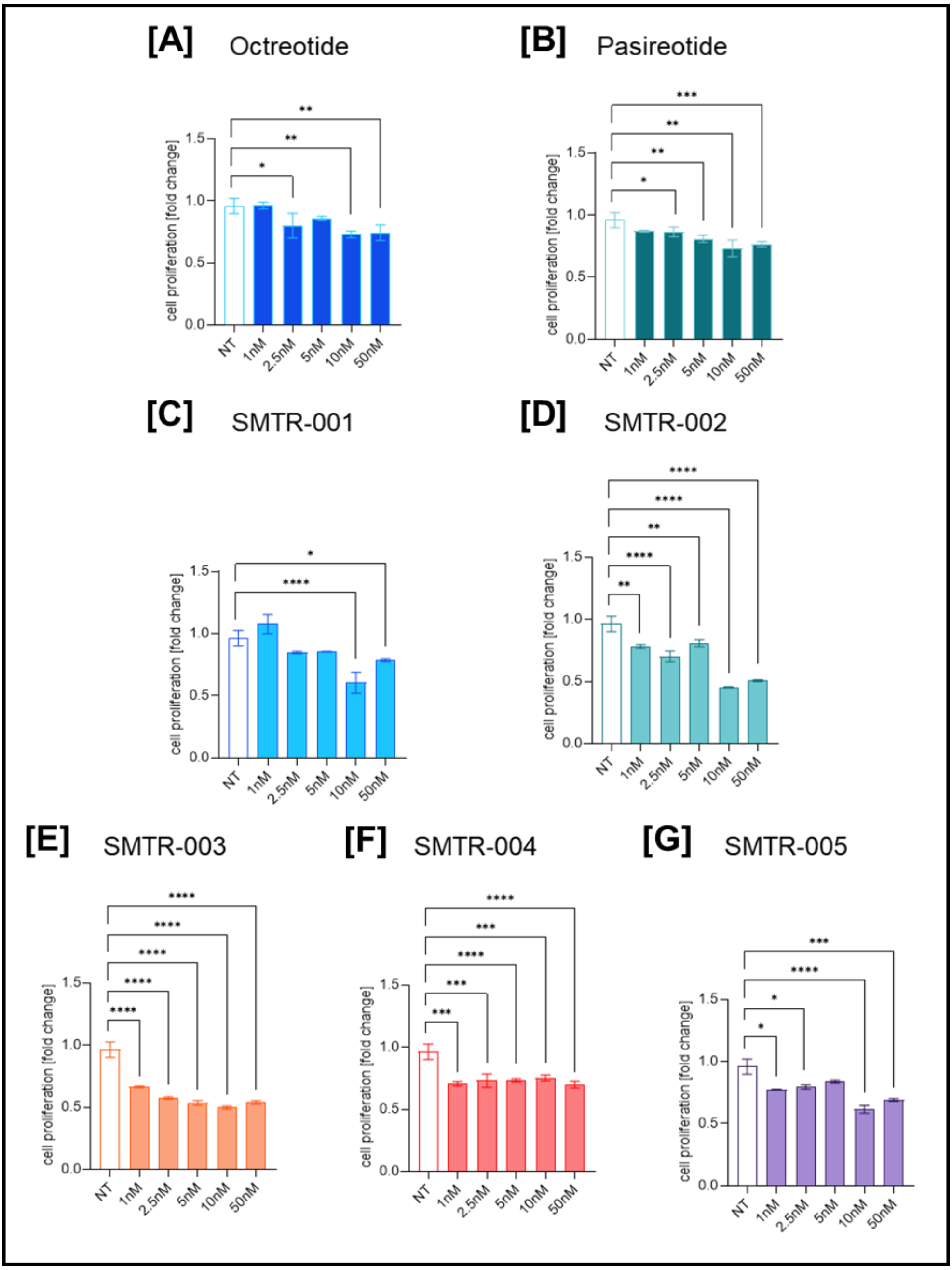
[A]
Octreotide
cell proliferation [fold change]
0.0
0.5
1.0
1.5
NT
1nM
2.5nM
5nM
10nM
50nM
*
**
**
[B]
Pasireotide
cell proliferation [fold change]
0.0
0.5
1.0
1.5
NT
1nM
2.5nM
5nM
10nM
50nM
*
**
**
***
[C]
SMTR-001
cell proliferation [fold change]
0.0
0.5
1.0
1.5
NT
1nM
2.5nM
5nM
10nM
50nM
****
*
[D]
SMTR-002
cell proliferation [fold change]
0.0
0.5
1.0
1.5
NT
1nM
2.5nM
5nM
10nM
50nM
**
****
**
****
****
[E]
SMTR-003
cell proliferation [fold change]
0.0
0.5
1.0
1.5
NT
1nM
2.5nM
5nM
10nM
50nM
****
****
****
****
****
[F]
SMTR-004
cell proliferation [fold change]
0.0
0.5
1.0
1.5
NT
1nM
2.5nM
5nM
10nM
50nM
***
***
****
***
****
[G]
SMTR-005
cell proliferation [fold change]
0.0
0.5
1.0
1.5
NT
1nM
2.5nM
5nM
10nM
50nM
*
*
****
***

Figure 27. *WST-1 cell proliferation assay results on 2D cultures of AtT-20 cells. Among the reference compounds, pasireotide showed a stronger antiproliferative effect (maximum reduction of 20–27%,* ***B****) compared to octreotide (maximum reduction of 23–24%,* ***A****). Among the test compounds, a significant antiproliferative effect at various concentrations was observed for SMTR-002 (maximum reduction of 27–53%,* ***D****), SMTR-003 (30–48%,* ***E****), and SMTR-004 (24–27%,* ***F****). SMTR-001 (37% reduction at 10 nM,* ***C****) and SMTR-005 (36% at 10 nM and 28% at 50 nM,* ***G****) showed lower efficacy. Data are presented as mean ± standard deviation (SD); * $p \leq 0.05$; ** $p \leq 0.01$; *** $p \leq 0.001$; **** $p \leq 0.0001$.*

We performed a statistical analysis using one-way ANOVA followed by Dunnett's multiple comparison test comparing some of the lowest concentrations (1 nM, 5 nM, and 10 nM) of the test compounds with those of the reference peptides.

Compared to pasireotide (Figure 28A), a significantly greater effect was observed particularly for SMTR-003 at all tested concentrations, and for SMTR-004 at 1 nM and 5 nM. SMTR-002 exhibited a stronger antiproliferative effect at 10 nM.

Compared to octreotide (Figure 28B), SMTR-002 and SMTR-003 showed the strongest effect with a high level of statistical significance at all concentrations, while SMTR-004 was more effective at 1 nM and 5 nM. SMTR-001 was more effective only at 10 nM, and SMTR-005 only at 1 nM.

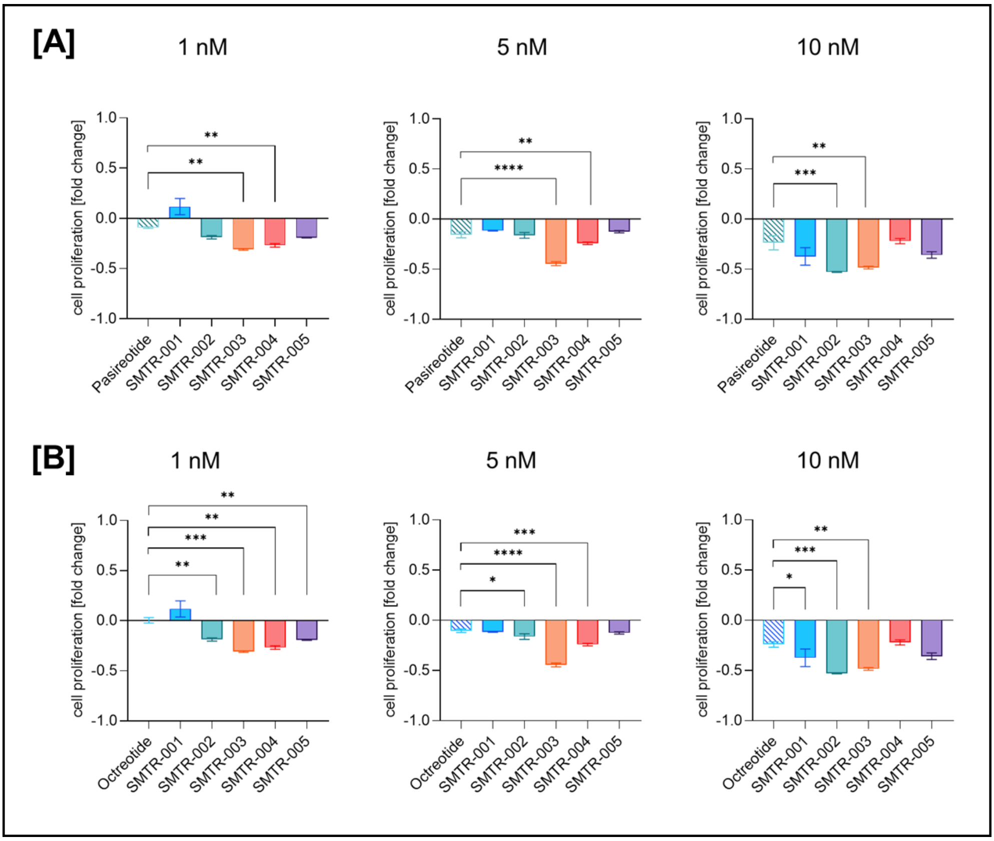

*Figure 28. Direct comparisons between test and reference compounds for their efficacy in inhibiting cell proliferation on AtT-20 cells at the lowest concentrations (1 nM, 5 nM, 10 nM). Compared to pasireotide (**A**), SMTR-003 showed a significantly greater antiproliferative effect at all concentrations; SMTR-004 at 1 nM, and 5 nM; and SMTR-002 at 10 nM. Compared to octreotide (**B**), SMTR-002 and SMTR-003 showed greater efficacy at all concentrations, while SMTR-004 was more effective at 1 nM and 5 nM. SMTR-001 showed greater efficacy only at 10 nM, and SMTR-005 only at 1 nM. Data are presented as mean ± standard deviation (SD); * $p \leq 0.05$; ** $p \leq 0.01$; *** $p \leq 0.001$; **** $p \leq 0.0001$.*

Effects of SSAs on the proliferation of NT-3 cells in 2D cultures

The same analysis was performed on NT-3 cells, using increasing concentrations (1 nM, 2.5 nM, 5 nM, 10 nM, and 50 nM) of the compounds. The WST-1 assay was carried out at a 5-day post-treatment time point.

In this case, all test compounds demonstrated a similar efficacy when compared to the untreated control, with a significant reduction in WST-1 signal observed at all concentrations evaluated (from 25% to 38% for SMTR-001; from 27% to 39% for

SMTR-002; from 30% to 35% for SMTR-003; from 23% to 39% for SMTR-004; from 24% to 36% for SMTR-005; $p \leq 0.0001$; Figure 29C-G). These patterns closely resembled those observed for octreotide (from 22% to 26%, $p \leq 0.0001$; Figure 29A) and pasireotide (from 17% to 33%, $p \leq 0.0001$; Figure 29B). No visible cytotoxicity or cell detachment was observed for any of the tested compounds.

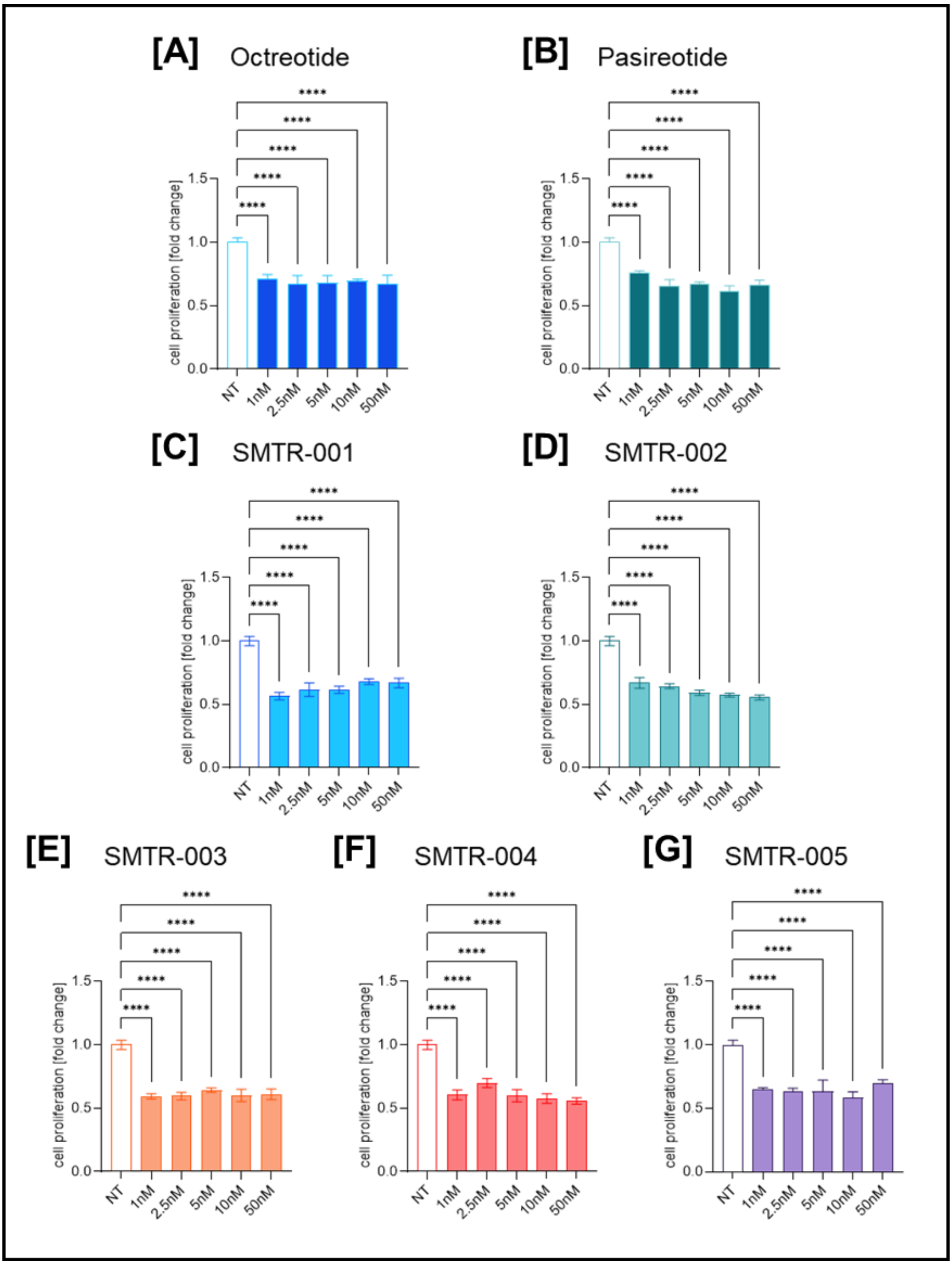
[A] Octreotide
[B] Pasireotide
[C] SMTR-001
[D] SMTR-002
[E] SMTR-003
[F] SMTR-004
[G] SMTR-005
cell proliferation [fold change]
0.0
0.5
1.0
1.5
NT
1nM
2.5nM
5nM
10nM
50nM
****

Figure 29*. WST-1 cell proliferation assay results on 2D cultures of NT-3 cells. The reference compounds octreotide (22–26% reduction in cell proliferation,* ***A****) and pasireotide (17–33% reduction,* ***B****) showed similar levels of efficacy. A comparable trend was observed for all test compounds: SMTR-001 (25–38% reduction,* ***C****), SMTR-002 (27–39%,* ***D****), SMTR-003 (30–35%,* ***E****), SMTR-004 (23–39%,* ***F****), and SMTR-005 (24–36%,* ***G****). Data are presented as mean ± standard deviation (SD); **** $p \leq 0.0001$.*

The multiple comparisons statistical analysis performed using one-way ANOVA followed by Dunnett's multiple comparison test at some of the lowest concentrations (1 nM, 5 nM, and 10 nM), in comparison with the reference peptides, revealed significant differences at specific concentrations. Notably, all five test compounds demonstrated a significantly stronger effect than pasireotide (Figure 30A) at the 1 nM concentration. At 1 nM, SMTR-001, SMTR-003, and SMTR-004 induced a significantly stronger antiproliferative effect than octreotide (Figure 30B), while at 10 nM, SMTR-002, SMTR-003, SMTR-004, and SMTR-005 showed a more pronounced effect.

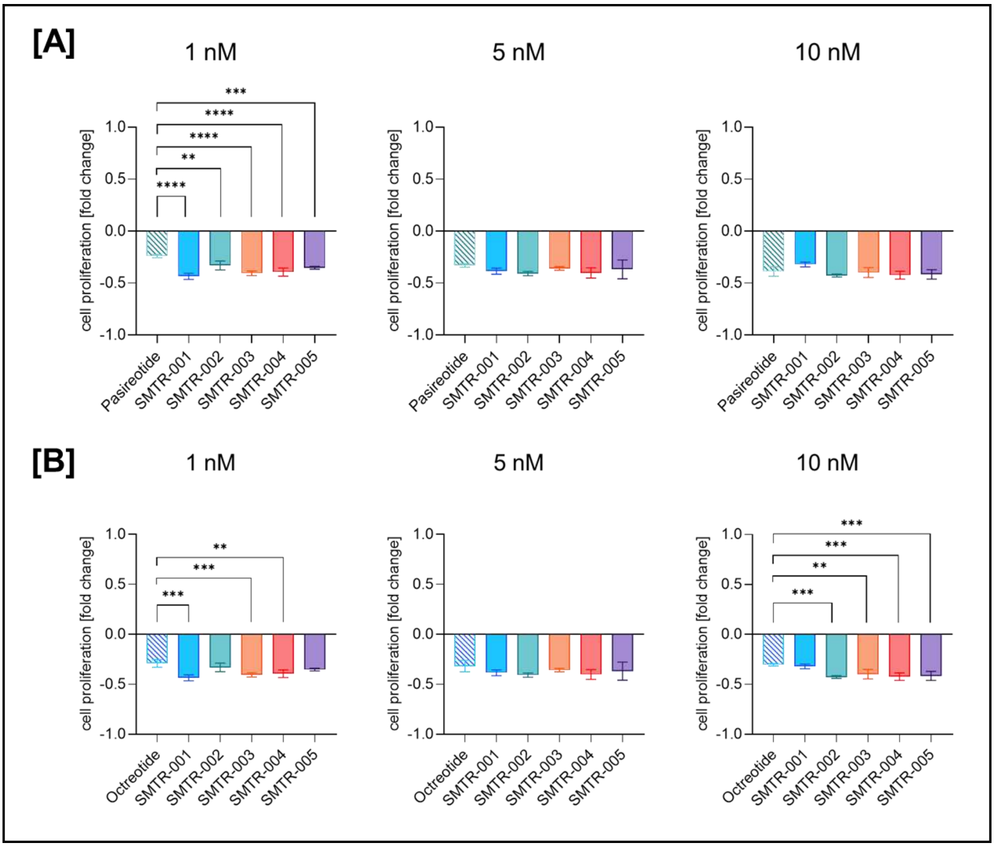

Figure 30. *Direct comparisons between test and reference compounds for their efficacy in inhibiting cell proliferation on NT-3 cells at the lowest concentrations (1 nM, 5 nM, 10 nM). At the concentration of 1 nM, all five test compounds showed a significantly greater antiproliferative effect compared to pasireotide (**A**). In comparison to octreotide (**B**), SMTR-001, SMTR-003, and SMTR-004 were more effective at 1 nM, while at 10 nM, SMTR-002, SMTR-003, SMTR-004, and SMTR-005 demonstrated superior efficacy. Data are presented as mean ± standard deviation (SD); *** $p \leq 0.01$; *** $p \leq 0.001$; **** $p \leq 0.0001$.

4.1.4 Effect of Novel Somatostatin Analogs on Hormone Secretion in Organotypic 3D Cultures

The investigation of the efficacy of our experimental compounds was further extended to organotypic 3D cultures (spheroids) derived from our cellular models. Organotypic 3D cultures represent a highly valuable *in vitro* model, as they better recapitulate cell density, cellular interactions, and the physiological characteristics of native tissues (Guan and Huang, 2022). Due to all these features, they represent a robust platform for determining drug efficacy in preclinical studies.

For these studies, based on the results obtained from analyses performed on 2D cultures and the structural characteristics, SMTR-002 was selected as the peptide of greatest interest (lead peptide). This selection was motivated by the compound’s strong efficacy in both cellular models, AtT-20 and NT-3, particularly at low concentrations (5 nM and 10 nM), where it often outperformed the other tested compounds, including the reference compounds octreotide and pasireotide.

Modulation of ACTH secretion in AtT-20 Cell Spheroids

Preliminary studies were carried out to determine the ability of AtT-20 cells to generate viable spheroids using the Akura Hanging Drop System. These assays also allowed the detection of the capacity of these 3D cultures to secrete high levels of ACTH.

The experimental design involved treating the cells with octreotide, pasireotide, and the selected lead peptide SMTR-002 at concentrations of 5 nM, 10 nM, and 50 nM. Hormone secretion levels were analyzed at a 72-hour post-treatment time point.

The results indicated an overall limited efficacy. A modest yet statistically significant effect was observed for octreotide at 10 nM (32% reduction in ACTH secretion: $p \leq 0.001$; Figure 31A) and for pasireotide at 5 nM (13% reduction; $p \leq 0.05$) and 10 nM (14% reduction; $p \leq 0.01$; Figure 31B) when compared with untreated control. In contrast, treatment with the lead peptide SMTR-002 did not produce any detectable effect (Figure 31C).

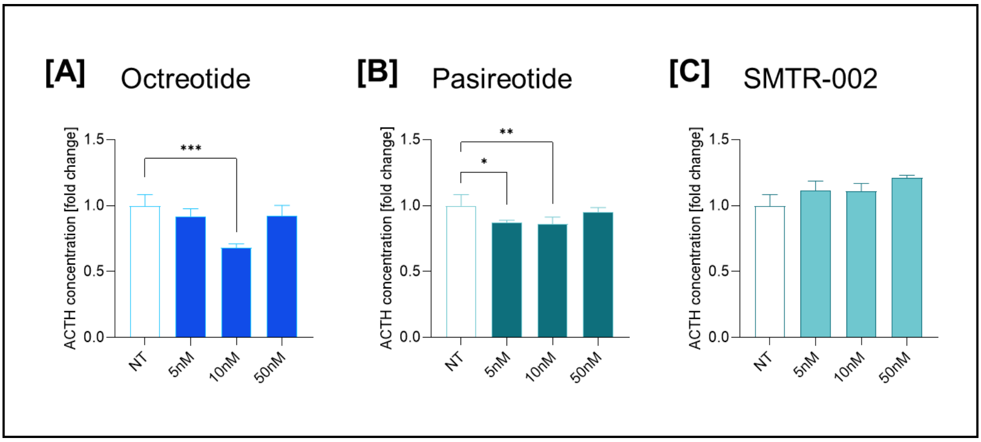

Figure 31. *ACTH ELISA assay results on 3D organotypic cultures of AtT-20 cells. The reference compound octreotide showed a reduction in ACTH secretion at a concentration of 10 nM (32% reduction), while pasireotide was effective at 5 nM (13% reduction) and 10 nM (14% reduction). The lead peptide SMTR-002 did not display a relevant effect. Data are presented as mean ± standard deviation (SD);* $^{*}p \leq 0.05$; $^{**}p \leq 0.01$; $^{***}p \leq 0.001$.

Modulation of Insulin Secretion in NT-3 Cell Spheroids

Similarly to the AtT-20 cells, we performed pilot studies in which we determined that NT-3 cells consistently form viable 3D floating spheroids in Ultra Low Attachment plates and secrete higher levels of insulin compared to 2D cultures.

In this case, the investigation focused on octreotide, used as the sole reference peptide, and on the lead peptide SMTR-002, both administered at concentrations of 5 nM, 10 nM, and 50 nM. Since this cell line exhibits an extended doubling time, a post-treatment time point of 14 days was selected.

The analysis revealed a moderate yet significant efficacy for both compounds. Octreotide demonstrated activity at concentrations of 5 nM (5% reduction in insulin secretion; $p \leq 0.05$) and 50 nM (11% reduction; $p \leq 0.0001$; Figure 32A), whereas the lead peptide SMTR-002 exhibited an effect at 10 nM (9% reduction; $p \leq 0.001$) and 50 nM (15% reduction, $p \leq 0.0001$; Figure 32B).

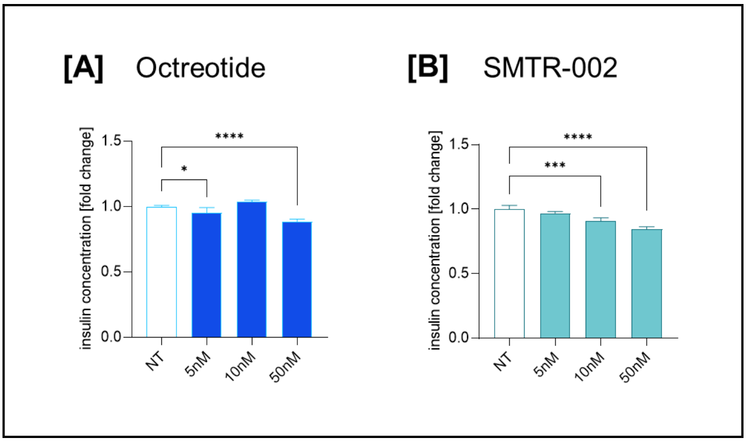

Figure 32. *Insulin ELISA assay results on 3D organotypic cultures of NT-3 cells. The reference compound octreotide was effective at concentrations of 5 nM (5% reduction in insulin secretion) and 50 nM (11% reduction). The lead peptide SMTR-002 showed a comparable effect at all tested concentrations, with significant results at 10 nM (9% reduction) and 50 nM (15% reduction). Data are presented as mean ± standard deviation (SD); * $p \leq 0.05$; *** $p \leq 0.001$; **** $p \leq 0.0001$.*

4.1.5 Effect of Novel Somatostatin Analogs on Cell Proliferation in Organotypic 3D Cultures

The antiproliferative effect of our test compounds was also evaluated on 3D organotypic cultures of our cellular models.

Effects of SSAs on the proliferation of AtT-20 cells 3D spheroids

AtT-20 cells showed a good ability to form viable 3D cultures, while maintaining a rapid growth rate. The formed spheroids were subsequently treated with the reference compounds octreotide and pasireotide, and the lead peptide SMTR-002 at concentrations of 5 nM, 10 nM, and 50 nM. The effect on cell proliferation was assessed using the CellTiter-Glo 3D viability assay at a 72-hour post-treatment time point.

Overall, when assessing the antiproliferative effect of the compounds, the 3D cultures derived from this cell line demonstrated marked resistance to pharmacological treatment. Regarding the reference compounds, a significant antiproliferative effect was observed following the administration of octreotide at a concentration of 10 nM, resulting in a 40% reduction in cellular proliferation ($p \leq 0.05$; Figure 33A). Conversely, pasireotide did not exhibit appreciable efficacy (Figure 33B), a finding that aligns with the results obtained with the novel lead peptide, SMTR-002 (Figure 33C).

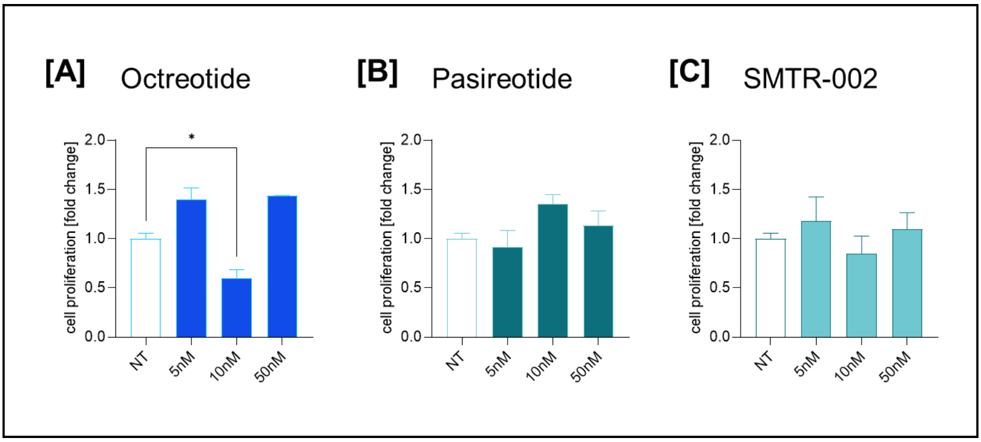

Figure 33. *CellTiter-Glo 3D proliferation assay results on 3D organotypic cultures of AtT-20 cells. The results showed a limited treatment effect on cell proliferation, with detectable efficacy for octreotide at a concentration of 50 nM (40% reduction). No significant reduction was observed for pasireotide or the lead peptide SMTR-002. Data are presented as mean ± standard deviation (SD); * $p \leq 0.05$.*

Effects of SSAs on the proliferation of NT-3 cells 3D spheroids

In this experiment as well, the compounds were administered to the cells at concentrations of 5 nM, 10 nM, and 50 nM. 14 days after treatment, cell proliferation in NT-3 floating spheroids was evaluated using the CellTiter-Glo 3D viability assay. Treatment with the reference compound octreotide did not yield a substantial effect and was characterized by a considerable degree of variability across the different conditions (Figure 34A). In contrast, the lead peptide SMTR-002 exhibited a markedly higher level of efficacy at all concentrations tested (30% reduction in cell proliferation at 5 nM and 10 nM, $p \leq 0.0001$; 14% reduction at 50 nM, $p \leq 0.01$; Figure 34B).

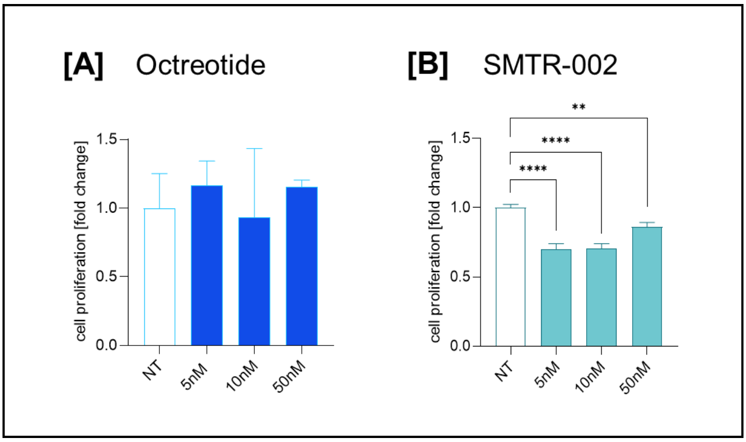

*Figure 34. CellTiter-Glo 3D cell proliferation assay results on 3D organotypic cultures of NT-3 cells. The reference compound octreotide showed a high level of variability without a substantial effect. The lead peptide SMTR-002 demonstrated a greater reduction in cell proliferation at all concentrations (30% reduction at 5 nM and 10 nM; 14% reduction at 50 nM). Data are presented as mean ± standard deviation (SD); *** $p \leq 0.01$*; ***** $p \leq 0.0001$.

4.1.6 Effect of Novel Somatostatin Analogs on Intracellular Cyclic AMP (cAMP) Levels

Under physiological conditions, the binding of SST to its receptors leads to the inhibition of the enzyme adenylyl cyclase (AC), resulting in a decreased cytoplasmic concentration of the second messenger cyclic AMP (cAMP). This, in turn, lowers intracellular Ca^{2+} levels, ultimately inhibiting hormone secretion.

This study evaluated the ability of our test compounds to engage this SSTR-mediated signaling pathway by measuring the reduction in intracellular cAMP levels in treated 2D cell cultures. Given that cAMP is the principal functional second messenger mediating the regulation of hormone secretion in pituitary cells (Ben-Shlomo et al., 2009), AtT-20 cells were selected to analyze the modulation of intracellular cAMP levels induced by the novel somatostatin analogs.

The analysis was performed at a 72-hour post-treatment time point. According to the experimental protocol, both treated and untreated samples were stimulated with 10 µM forskolin three hours prior to the assay.

Compared to a non-treated induced control (forskolin alone), octreotide demonstrated a strong ability to reduce intracellular cAMP levels at all concentrations (reduction in cAMP concentration equal to 43% at 10 nM, $p \leq 0.01$; 55% at 50 nM, $p \leq 0.001$; and 78% at 100 nM, $p \leq 0.0001$; Figure 35A). Similarly, pasireotide likewise demonstrated a good level of efficacy across all the conditions evaluated compared to forskolin alone (60% reduction at 10 nM, $p \leq 0.001$; 76% at 50 nM, $p \leq 0.0001$; 53% at 100 nM, $p \leq 0.001$; Figure 35B).

Among the test compounds, SMTR-005 proved to be the most effective, showing a significant reduction in intracellular cAMP levels compared to forskolin alone at all concentrations (71% reduction at 10 nM, $p \leq 0.0001$; 61% at 50 nM, $p \leq 0.0001$; 58% at 100 nM, $p \leq 0.0001$; Figure 35G). A less pronounced yet significant effect was observed for SMTR-002 (25% reduction at 50 nM, $p \leq 0.05$; 41% at 100 nM, $p \leq 0.01$; Figure 35B) and SMTR-004 (34% reduction at both 50 nM and 100 nM, $p \leq 0.01$; Figure 35F). SMTR-001 (Figure 35C) and SMTR-003 (Figure 35E) did not exhibit significant efficacy.

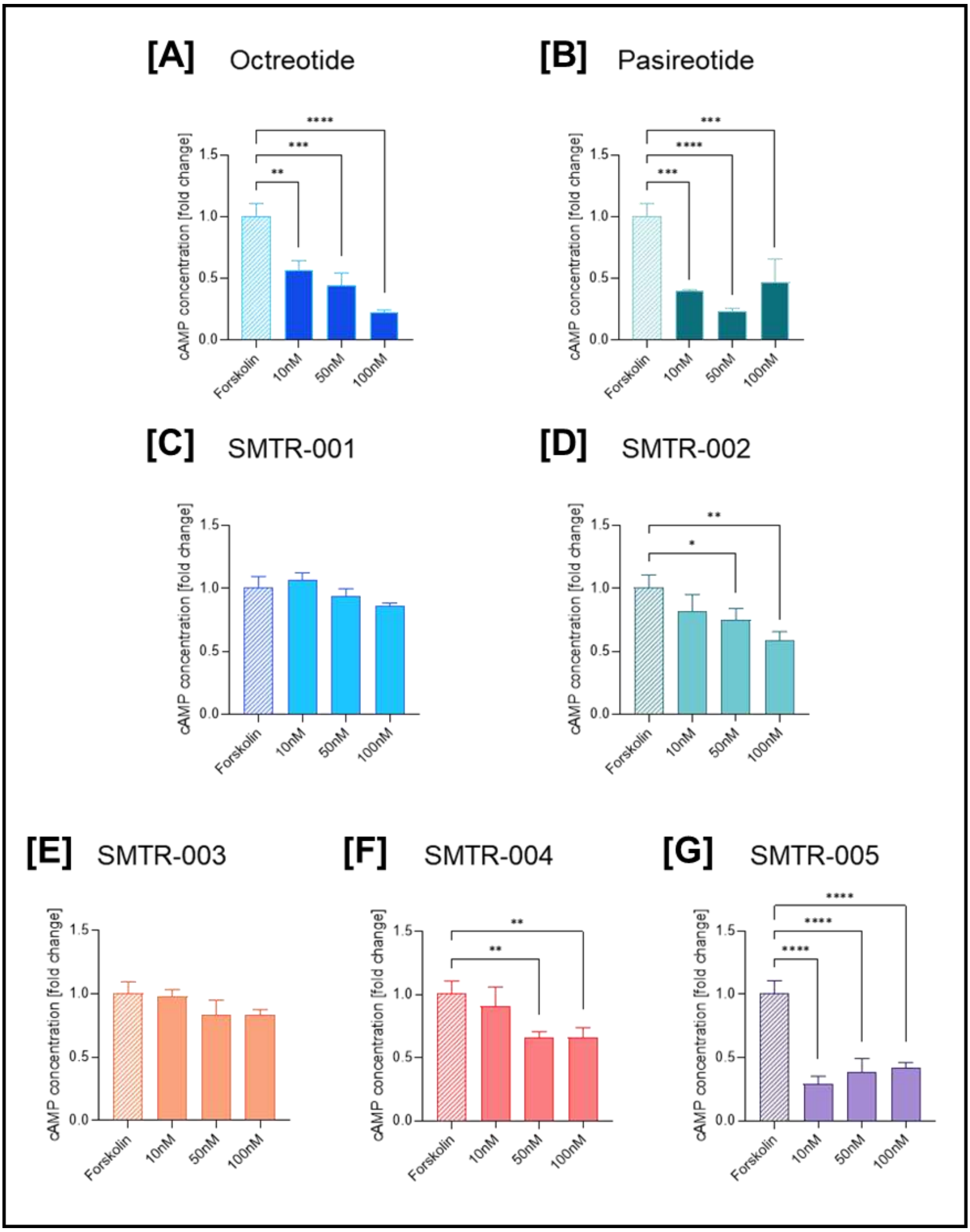
[A] Octreotide
[B] Pasireotide
[C] SMTR-001
[D] SMTR-002
[E] SMTR-003
[F] SMTR-004
[G] SMTR-005
cAMP concentration [fold change]
0.0
0.5
1.0
1.5
Forskolin
10nM
50nM
100nM
**
***
****
*

Figure 35. *Results of the cAMP-Glo assay performed on 2D cultures of AtT-20 cells. Compared to forskolin alone, octreotide (43% reduction at 10 nM, 55% at 50 nM, 78% at 100 nM;* ***A****) and pasireotide (60% reduction at 10 nM, 76% at 50 nM, 53% at 100 nM;* ***B****) showed a good ability to reduce intracellular cAMP levels at all concentrations tested. Among the test compounds, SMTR-005 (****G****) was the most effective at all concentrations (71% reduction at 10 nM, 61% at 50 nM, 58% at 100 nM). A less pronounced effect was observed for SMTR-002 (25% reduction at 50 nM, 41% at 100 nM;* ***D****) and SMTR-004 (34% reduction at both 50 nM and 100 nM;* ***F****), while SMTR-001 (****C****) and SMTR-003 (****E****) showed no significant efficacy. Data are presented as mean ± standard deviation (SD); * $p \leq 0.05$; ** $p \leq 0.01$; *** $p \leq 0.001$; **** $p \leq 0.0001$.*

Subsequent experiments were conducted to further investigate and evaluate the efficacy of the lead peptide SMTR-002. Lower concentrations (5 nM, 10 nM, 50 nM) were included in the analysis, with octreotide and pasireotide used as reference compounds. No additional experimental variations were introduced compared with the previous experiments.

The analyses revealed a favorable efficacy profile for SMTR-002 (reduction in cAMP concentration equal to 52% at 5 nM, $p \leq 0.0001$; 53% at 10 nM, $p \leq 0.0001$; 61% at 50 nM, $p \leq 0.0001$; Figure 36C), comparable to that of octreotide (37% reduction at 5 nM, $p \leq 0.001$; 44% at 10 nM, $p \leq 0.001$; 52% at 50 nM, $p \leq 0.0001$; Figure 36A) and pasireotide (49% reduction at 5 nM, $p \leq 0.0001$; 48% at 10 nM, $p \leq 0.0001$; 61% at 50 nM, $p \leq 0.0001$; Figure 36B).

These findings are consistent with the positive effects observed in the inhibition of hormone secretion and further underscore the high efficacy of the novel compounds on this specific pathway.

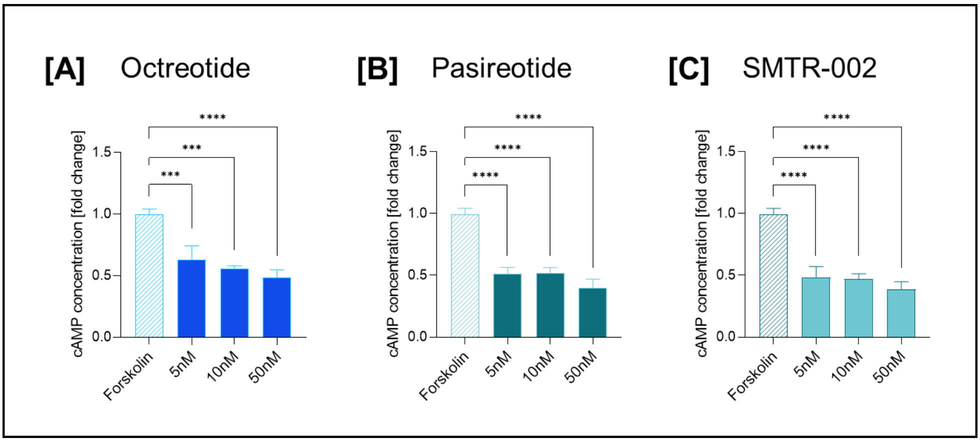

*Figure 36. Results of the cAMP-Glo assay performed on 2D cultures of AtT-20 cells focused on the lead peptide SMTR-002. The lead peptide displayed a robust efficacy profile at all tested concentrations (52% reduction in cAMP concentration at 5 nM; 53% at 10 nM; 61% at 50 nM), comparable to that of the reference compounds octreotide (37% reduction at 5 nM; 44% at 10 nM; 52% at 50 nM) and pasireotide (49% reduction at 5 nM; 48% at 10 nM; 61% at 50 nM). Data are presented as mean ± standard deviation (SD); *** $p \leq 0.001$; **** $p \leq 0.0001$.*

Section 4.2: Detection of ALT Activity in Pancreatic Neuroendocrine Tumors

4.2.1 Genomic DNA Extraction and Quantification

The initial tests of this study were conducted on genomic DNA extracted from our cellular models, following the protocol described by NJ Robinson and WP Schiemann (Robinson and Schiemann, 2023).

For each cell line, pellets of approximately 2×10^5 cells were prepared. DNA extraction was performed using the QCP lysis buffer, resulting in a crude cell lysate. The use of this buffer allows for the recovery not only of genomic DNA but also of circulating extrachromosomal DNA that has not yet been released. The extracted DNA was quantified using the QuantiFluor ONE dsDNA kit, which is based on the use of a highly selective fluorescent dye that binds to double-stranded DNA. DNA quantification was performed by constructing a calibration curve based on the analysis of internal standards with known DNA concentrations (Figure 37). This step was essential for the subsequent PCR analyses.

The DNA quantification results for each cell line are presented in Table 3.

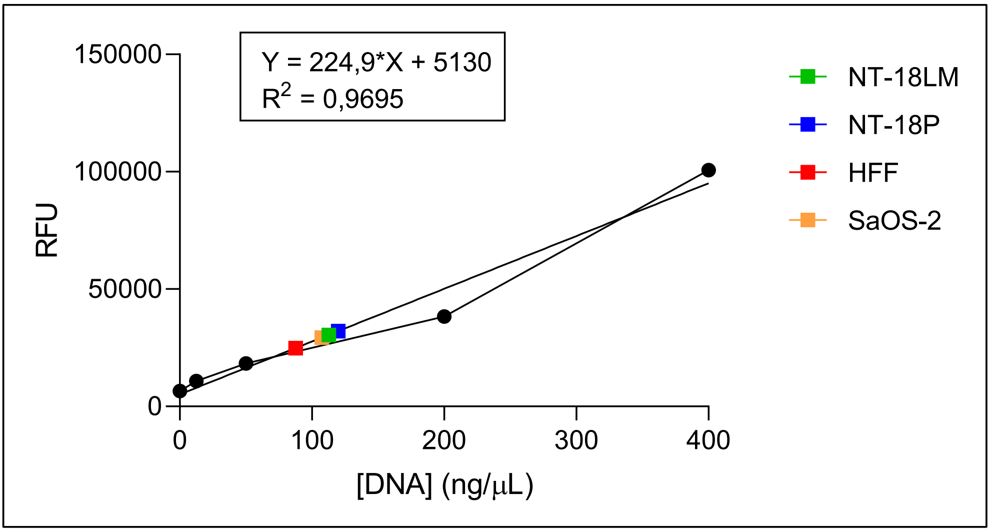

Figure 37. DNA quantification using the QuantiFluor ONE dsDNA assay. The calibration curve and the interpolated values calculated for the experimental models NT-18LM, NT-18P, SaOS-2, and HFF are shown.

	NT-18LM	NT-18P	SaOS-2	HFF
[DNA] (ng/µL)	112.77	119.84	107.49	87.63

Table 3. *Results of DNA quantification extracted from cell pellets of the NT-18LM, NT-18P, SaOS-2, and HFF cell models. The analysis was performed using the QuantiFluor ONE dsDNA kit.*

4.2.2 The RCA Assay Is Effective in Amplifying C-Circles

A preliminary analysis was conducted to evaluate the efficiency of the RCA reaction. This analysis was conducted on genomic DNA obtained from our ALT+ cell model, the SaOS-2 cell line, which is positive for C-circle synthesis. The amplification was performed using Φ29 DNA polymerase under isothermal conditions. Two experimental conditions were tested: one in the presence (Φ29+) and one in the absence (Φ29–) of the polymerase. Following the RCA assay, the amplification products were further amplified by standard qPCR using C-circle–specific primers.

The analysis showed significantly greater amplification in the Φ29+ sample (Ct = 16.56) compared to the Φ29– sample (Ct = 18.45), corresponding to an approximate 3.7-fold enrichment, indicating good efficiency of the RCA reaction in enriching the initial C-circle content (Figure 38).

This validation allowed the analysis to be extended to our PanNET cell lines for their characterization for the presence of ALT activity.

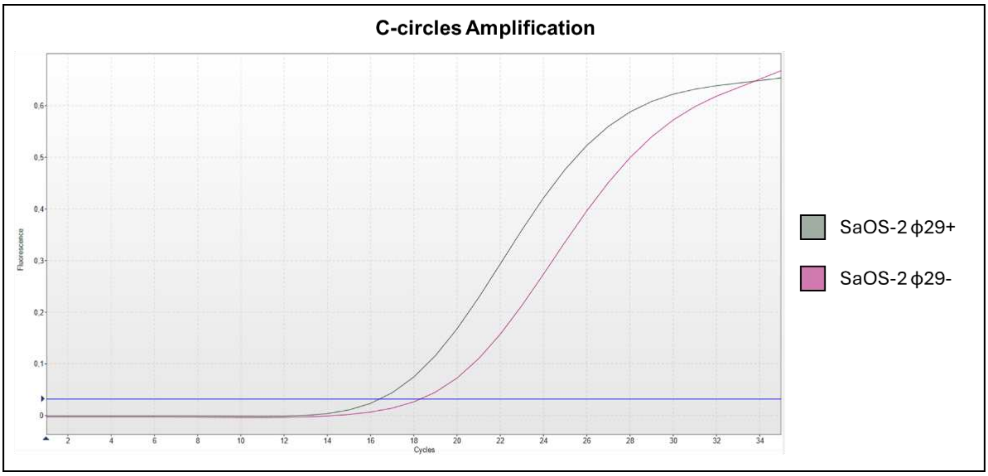

Figure 38. *qPCR analysis of SaOS-2 DNA samples subjected to RCA. Two conditions were analyzed: in the presence (Φ29+) and absence (Φ29−) of Φ29 polymerase. The Φ29+ sample showed greater amplification (Ct = 16.56) compared to the Φ29− sample (Ct = 18.45), indicating the effectiveness of the RCA reaction in enriching the input DNA.*

4.2.3 Detection of C-Circles in Genomic DNA

To characterize our PanNET cell models (NT-18P and NT-18LM) for the presence of ALT activity, the extracted genomic DNA samples were subjected to the RCA assay, followed by qPCR amplification. SaOS-2 and HFF cell lines were included in the analysis as positive and negative controls, respectively.

The analysis revealed a strong amplification of C-circles in both PanNET cell lines. The amplification profiles of NT-18P (Ct = 21.21) and NT-18LM (Ct = 21.52) were even more pronounced than that of the ALT+ control SaOS-2 (Ct = 23.29). These results suggest a higher initial content of C-circles in our PanNET models, that is indicative of ALT-associated activity. Amplification in the ALT– control HFF was minimal, indicating negligible ALT activity (Figure 39A).

Amplification of the housekeeping gene *GNAT3* was detected with high efficiency in all cell lines, as expected (Figure 39B).

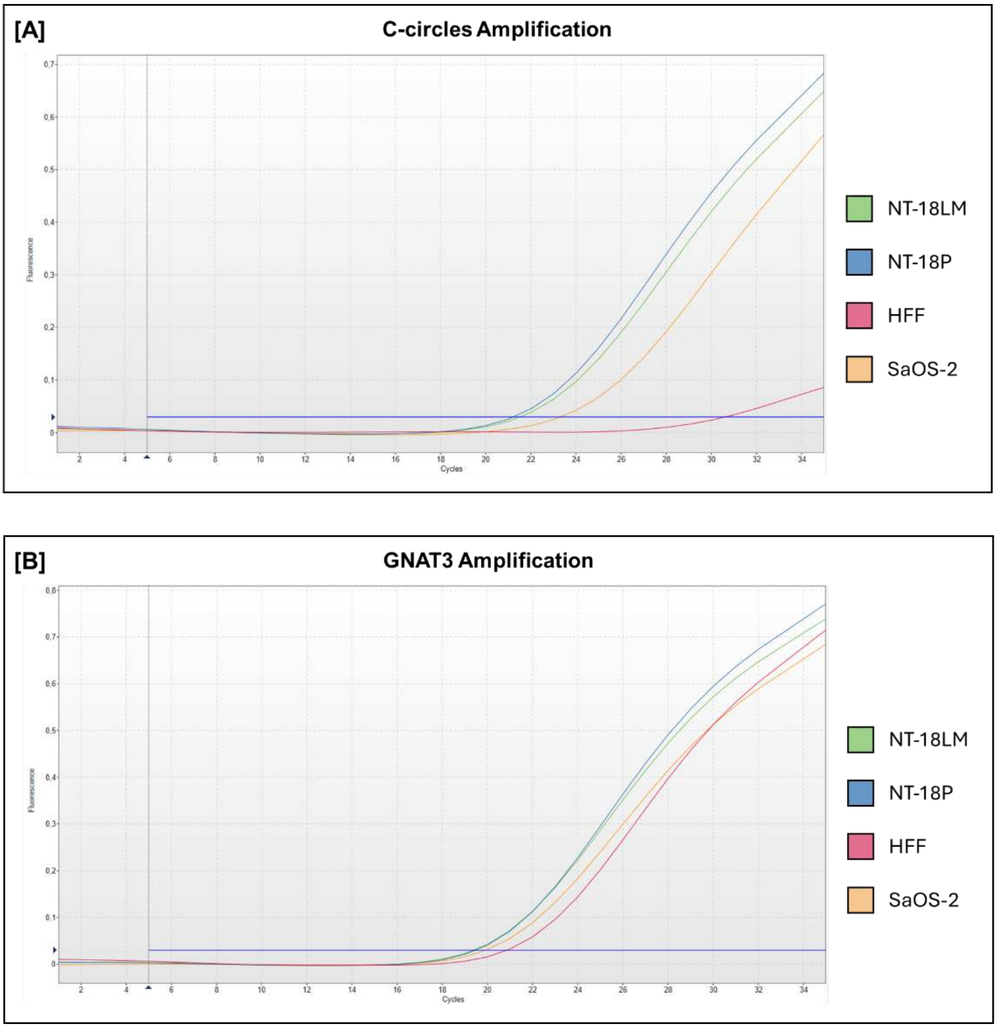

Figure 39. *qPCR analysis of genomic DNA samples from NT-18LM, NT-18P, HFF, and SaOS-2 cells subjected to RCA. (**A**) Amplification curves of C-circles. The analysis revealed strong amplification for the NT-18LM and NT-18P cell lines, exceeding that of the ALT+ control SaOS-2. The HFF line showed no significant amplification. (**B**) Amplification curves of the housekeeping gene* GNAT3*. Consistent amplification was observed across all cell lines.*

Subsequent quantification of relative C-circle levels, performed using the $2^{(-\Delta Ct)}$ method, confirmed a high abundance of C-circles in the PanNET cell lines. Specifically, the normalized values were higher in both lines compared to the ALT+ control SaOS-2, with a relative C-circle signal normalized to the reference locus equal to 0.21 for NT-18LM and 0.26 for NT-18P, versus 0.10 for SaOS-2 (Figure 40).

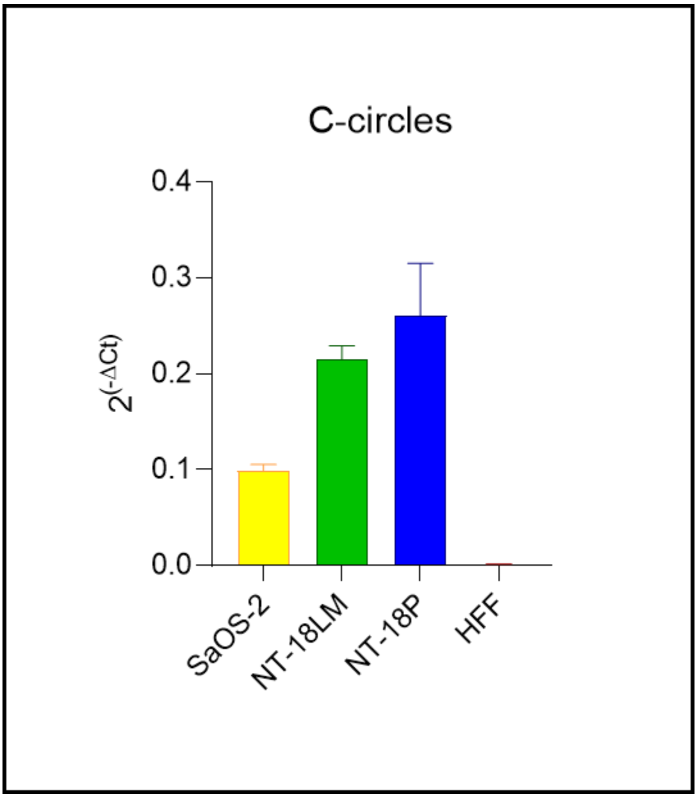

Figure 40. *Analysis of relative normalized C-circle abundance in NT-18LM, NT-18P, SaOS-2, and HFF cell lines using the* $2^{(-\Delta Ct)}$ *method. High levels of C-circles were detected in the NT-18LM (relative C-circle abundance = 0.21) and NT-18P (relative C-circle abundance = 0.26) lines, exceeding those of the ALT+ control SaOS-2 (relative C-circle abundance = 0.10). The ALT− HFF line showed negligible levels. Data are presented as mean ± standard deviation (SD).*

Furthermore, to support and validate the experimental results, the amplification products were analyzed by electrophoresis on a 2% agarose gel and subsequently visualized under UV light.

As expected, similar banding patterns were observed in both the ALT+ SaOS-2 control and the PanNET cell lines, displaying a characteristic smear pattern typical of concatemers resulting from C-circle amplification. Specifically, band intensity was higher in the NT-18P and NT-18LM cell lines compared to the SaOS-2 control, confirming the results obtained from qPCR data analysis. In contrast, no amplification product was observed in the ALT– HFF cell line. Amplicons corresponding to the housekeeping gene *GNAT3* were detected in all the cell lines analyzed (Figure 41).

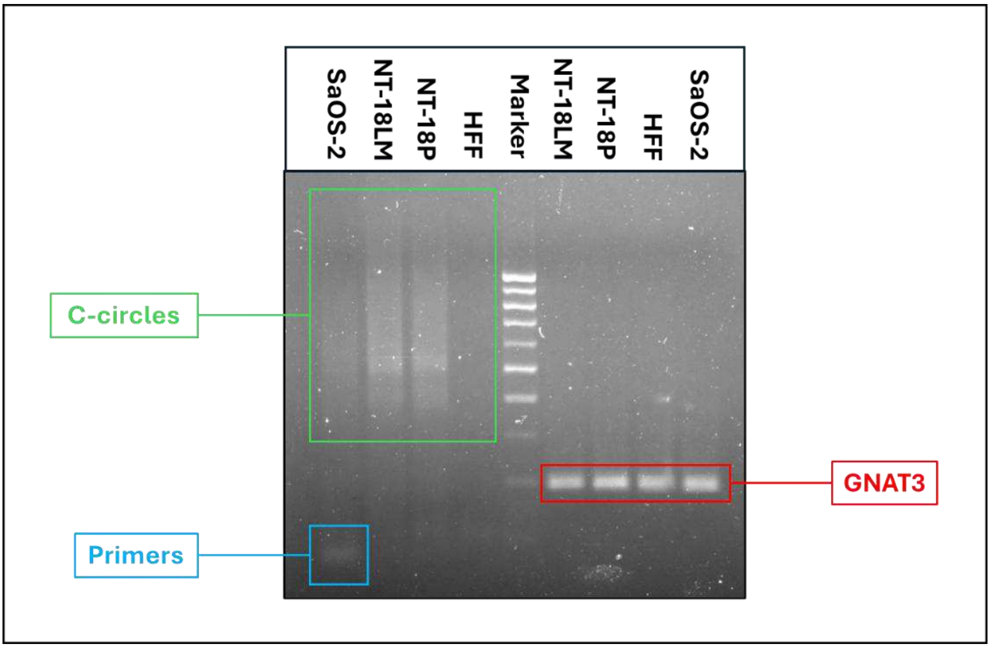

Figure 41. *Analysis by 2% agarose gel electrophoresis of amplification products from the NT-18LM, NT-18P, SaOS-2, and HFF cell lines obtained by qPCR. Bands corresponding to C-circles (left, green box) and the housekeeping gene* GNAT3 *(right, red box) are shown.*

In conclusion, the analyses performed enabled the characterization of the PanNET cell lines NT-18P and NT-18LM for the presence of C-circles at the cellular level. This feature, together with the presence of inactivating *DAXX* mutations in both lines, as already reported in literature, represents a specific marker of ALT activity, confirming the ALT+ phenotype of these cell lines.

4.2.4 Detection of C-Circles in Cell Culture Supernatants

After confirming the presence of C-circles in genomic DNA samples from our PanNET cell models, the analysis was extended to cell culture supernatant samples. Samples were collected from 2D cell cultures of all our cell models at a 48-hour time point after seeding. Extraction and purification of circulating cell-free DNA were performed using the QIAamp ccfDNA/RNA kit. In this case, since the previously used protocol was not suitable for this type of sample, the samples were not subjected to RCA and were instead directly analyzed by qPCR.

The analysis showed strong amplification for our PanNET cell lines, with an increase in fluorescence signal at very low amplification cycles (Ct = 8.08 for NT-18P; Ct = 9.46 for NT-18LM), lower than the amplification threshold cycle of the ALT+ control SaOS-2 (Ct = 11.70) (Figure 42A). This result, in agreement with the analysis of genomic DNA samples, further confirms the high presence of C-circles in the PanNET cell lines of interest, highlighting the presence of an ALT+ phenotype in these lines.

However, in this analysis, amplification was also observed in the ALT− control HFF, although the corresponding amplification threshold cycle was significantly higher (Ct = 16.67) compared to the other samples (Figure 44). This phenomenon is likely due to two main factors. First, the primers used for C-circle amplification have a strong tendency to form dimers, owing to their length and the repetitive nature of their sequences. This is highlighted by the melting profiles of the C-circle amplicons (Figure 43), which show a low-temperature shoulder consistent with primer-dimer formation. Second, residual genomic DNA released into the culture medium as a result of cell death may contribute to the observed amplification. This hypothesis is further supported by the amplification of the *GNAT3* gene in most of the analyzed samples (NT-18LM, NT-18P, SaOS-2), although in this case, amplification also occurred at later cycles (Figure 42B).

It is therefore clear that the technique applied in this case still presents methodological limitations. Further analyses will be necessary to refine the procedure and optimize the detection of C-circles in cell culture supernatants.

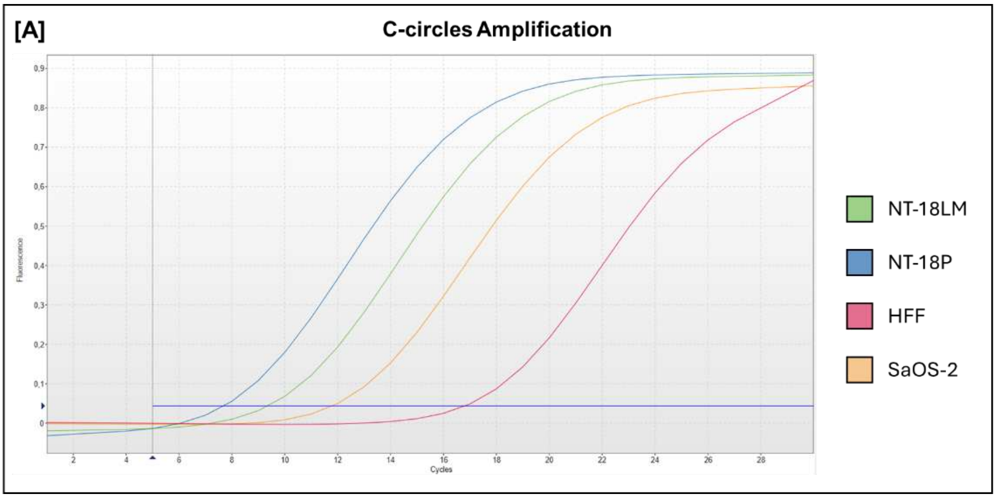

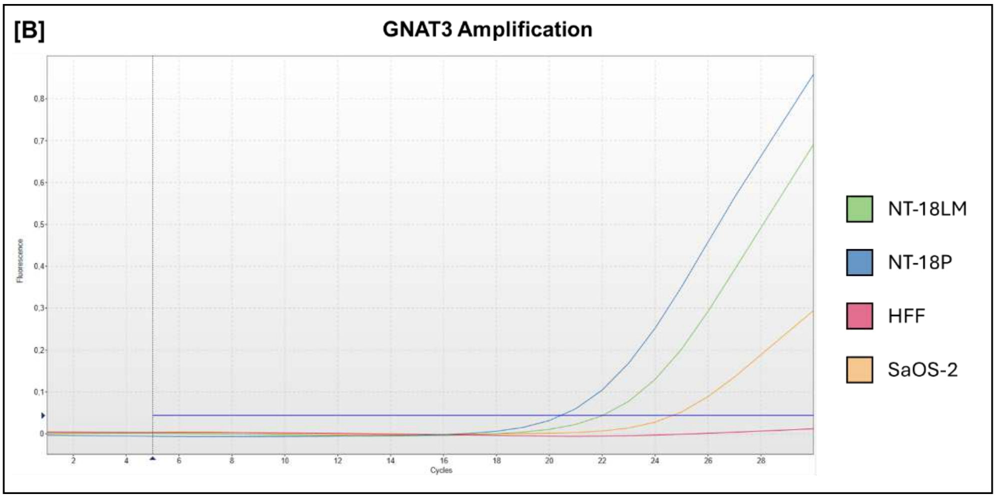

Figure 42. *qPCR analysis of cell-free DNA samples from NT-18LM, NT-18P, HFF, and SaOS-2 cells. (**A**) Amplification curves of C-circles. The analysis showed strong amplification in NT-18LM and NT-18P lines, exceeding that of the ALT+ control SaOS-2. Amplification was also detected in the ALT− control HFF, likely due to primer dimerization and/or the presence of residual genomic DNA. (**B**) Amplification curves of the* GNAT3 *gene. The observed amplification is likely due to the presence of residual genomic DNA.*

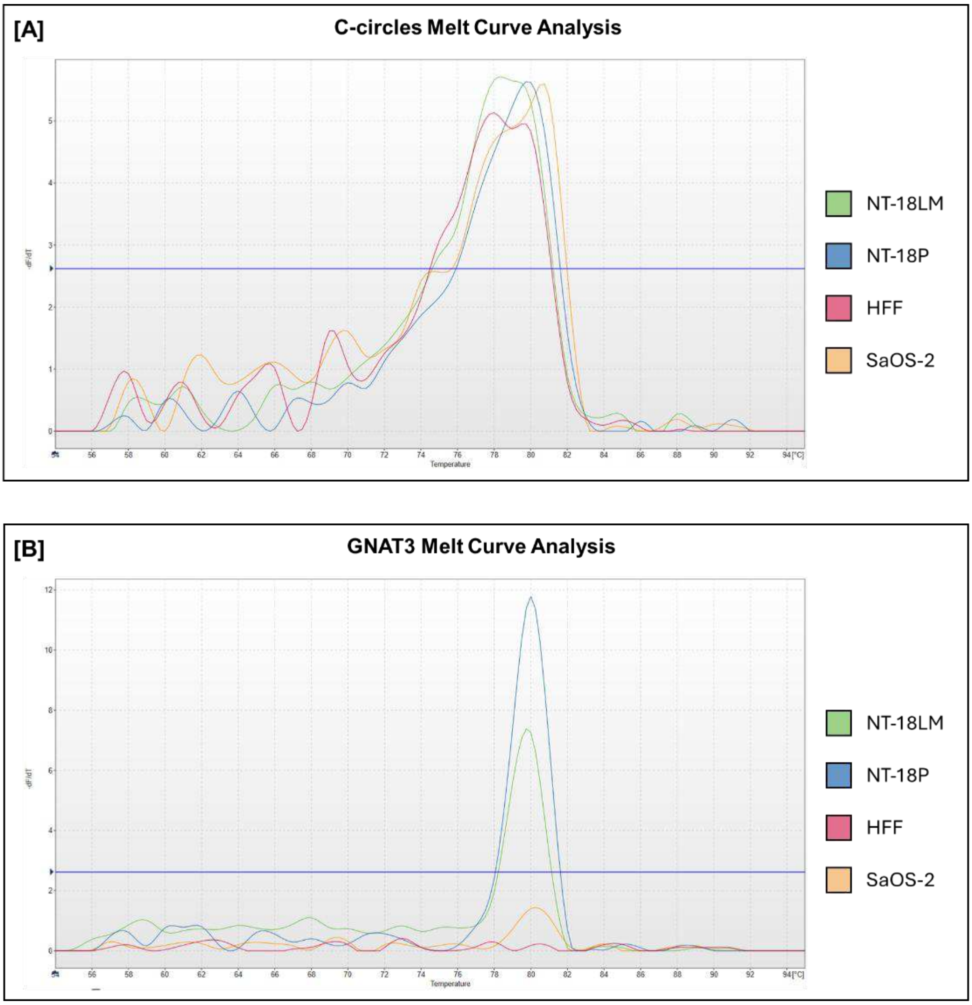

Figure 43. *Melting curve analysis of qPCR products from NT-18LM, NT-18P, HFF, and SaOS-2 cell culture supernatants. (**A**) Specific melting profiles of C-circles amplicons. (**B**) Specific melting profiles of* GNAT3 *amplicons.*

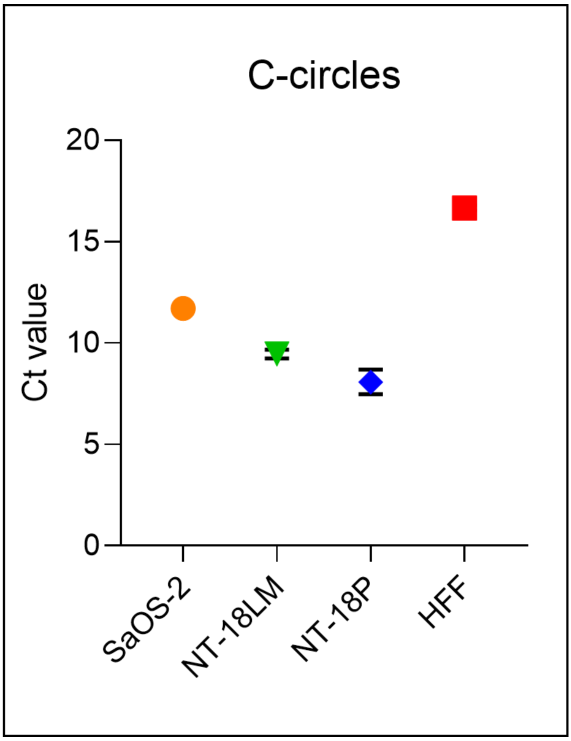

Figure 44. *Threshold cycle (Ct) values for C-circle amplification in cell-free DNA samples from SaOS-2, NT-18LM, NT-18P, and HFF cells. Lower Ct values indicate higher amplification efficiency. Data are presented as mean ± standard deviation (SD).*

In conclusion, the analyses conducted revealed the presence of C-circles in the PanNET cell lines NT-18LM and NT-18P, indicating active ALT mechanisms in these models. These findings suggest that such characteristics could serve as potential markers for the diagnosis and treatment of neuroendocrine tumors with phenotypic similarities to the studied cell lines.

4.2.5 Drug Treatments

Following the characterization of our PanNET cell models for the presence of C-circles and ALT activity, their sensitivity to targeted therapies for ALT+ tumors was assessed. Specifically, two experimental compounds, Adavosertib and Ceralasertib, currently undergoing clinical evaluation, were tested.

Our PanNET cell models, NT-18LM and NT-18P, along with the ALT+ control cell line SaOS-2 and the ALT− line HFF, were treated with increasing concentrations of the selected compounds, administered as monotherapies. Specifically, a total of 11 increasing concentrations (12.2 nM, 24.4 nM, 48.8 nM, 97.5 nM, 195 nM, 390 nM, 780 nM, 1.56 µM, 3.12 µM, 6.25 µM, and 12.5 µM) of the selected compounds were tested. The aim was to generate dose–response curves for each model and to determine the corresponding half-maximal inhibitory concentration (IC50).

Treatment with Adavosertib

Pharmacological treatment with Adavosertib demonstrated differential efficacy profiles across the analyzed cell lines. In the ALT+ control line SaOS-2, a strong dose-dependent response was observed, with an IC50 value of 0.459 µM and a reduction in cell viability exceeding 99% at the highest concentrations tested (6.25 µM and 12.5 µM; Figure 45A). In the ALT− HFF cell line, although the observed IC50 value (0.436 µM) was very similar to that of the SaOS-2 cells, a higher resistance to treatment was noted (Figure 45B). Specifically, the reduction in cell proliferation reached a plateau between 60–70%, indicating a limited response at higher drug concentrations.

The NT-18P cell line exhibited the strongest response to the treatment, with an IC50 value of 0.144 µM (Figure 46B), which was significantly lower than that observed in the ALT+ control SaOS-2. In contrast, the NT-18LM cell line exhibited a more resistant profile, with an IC50 value of 1.66 µM (Figure 46A) and an efficacy profile comparable to that of the ALT− HFF line.

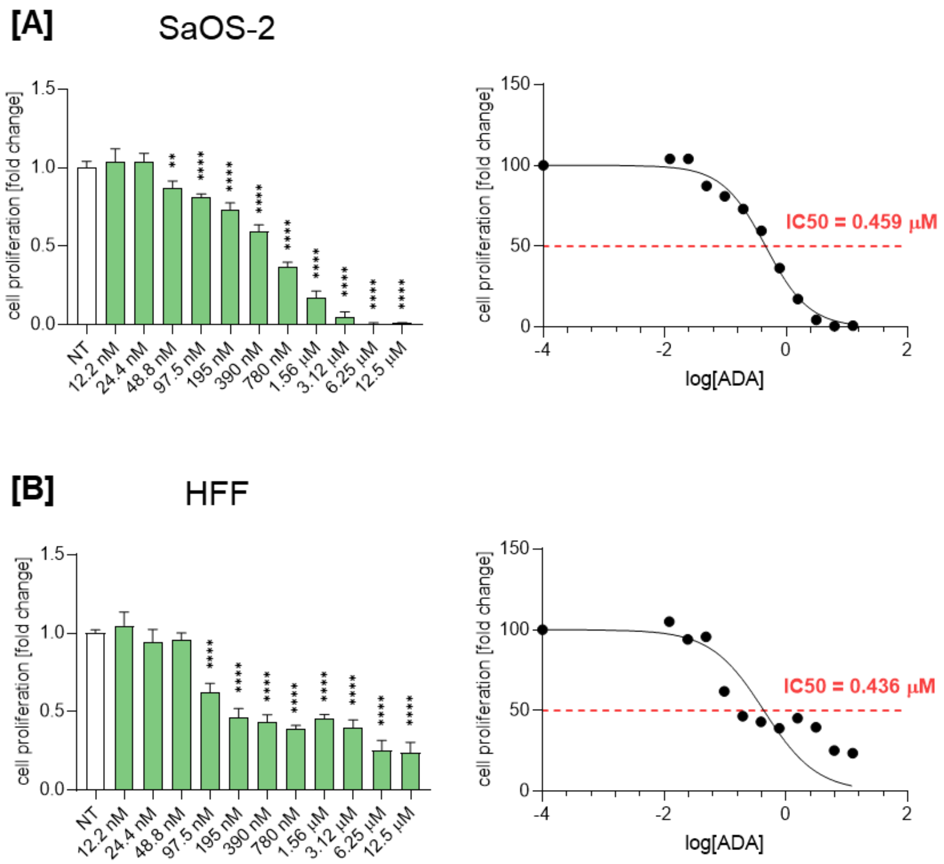

Figure 45. *Dose-response curves of SaOS-2 and HFF cell lines treated with increasing concentrations of Adavosertib. The ALT+ SaOS-2 control line showed high sensitivity to treatment (IC50 = 0.459 µM;* ***A****). The ALT– HFF line had a similar IC50 (0.436 µM;* ***B****) but was more resistant at higher drug concentrations. Statistical analysis was performed by comparing treated samples to the untreated control (NT); ** $p \leq 0.01$; **** $p \leq 0.0001$.*

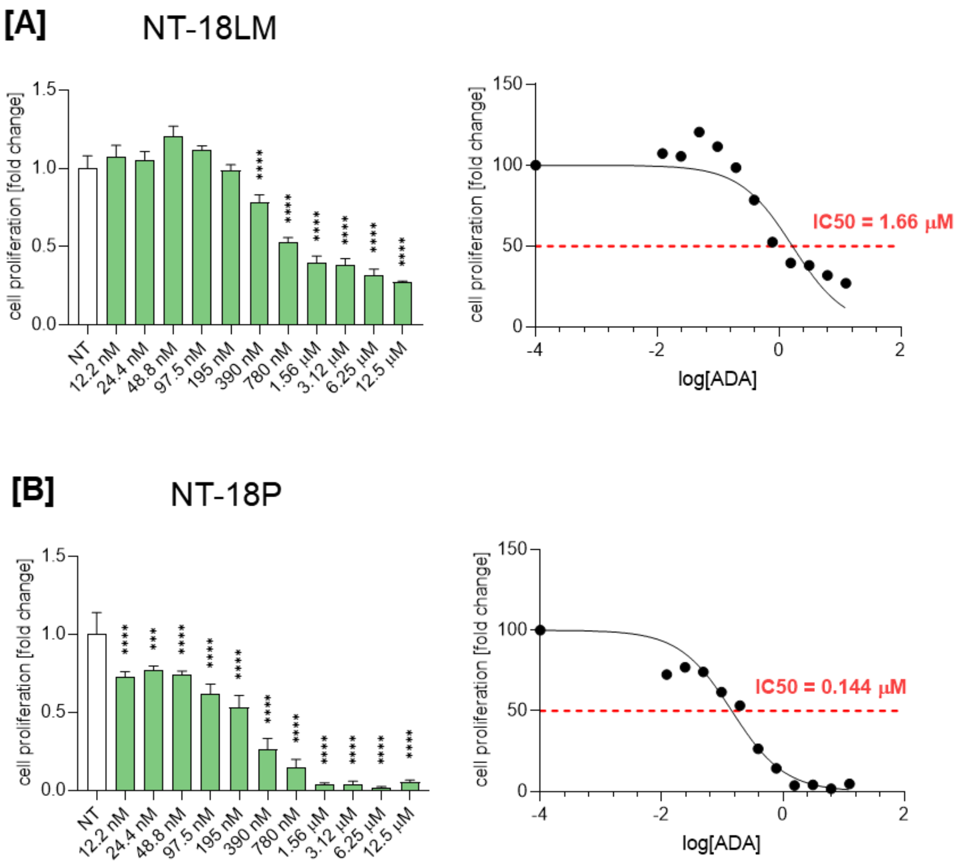

*Figure 46. Dose-response curves of NT-18LM, and NT-18P cell lines treated with increasing concentrations of Adavosertib. NT-18P cells were highly sensitive (IC50 = 0.144 µM; **B**), while NT-18LM cells showed greater resistance (IC50 = 1.66 µM; **A**), comparable to the ALT− HFF line. Data are presented as mean ± standard deviation (SD). Statistical analysis was performed by comparing treated samples to the untreated control (NT); *** $p \leq 0.001$; **** $p \leq 0.0001$.*

Treatment with Ceralasertib

The administration of Ceralasertib resulted in a detectable cytotoxic effect across all our cellular models; however, this effect was significantly less pronounced compared to that induced by Adavosertib.

In the ALT+ cell line SaOS-2, a dose-dependent response was observed; however, it was associated with a relatively high IC50 value (4.07 µM) (Figure 47A). The efficacy of the pharmacological treatment was even more limited in the ALT− HFF cell line, where a cytotoxic effect was evident only at higher concentrations (3.12 µM and above), with an IC50 value of 5.42 µM (Figure 47B).

The PanNET cell lines generally exhibited greater sensitivity to the treatment compared to the control lines. In NT-18LM cells, a slightly increased cytotoxic effect was observed, with an IC50 value of 3.47 µM (Figure 48A). In contrast, the NT-18P cell line displayed a marked dose-dependent response, with cell death exceeding 90% at the highest concentrations tested (6.25 µM and 12.5 µM), and an IC50 value of 0.61 µM (Figure 48B).

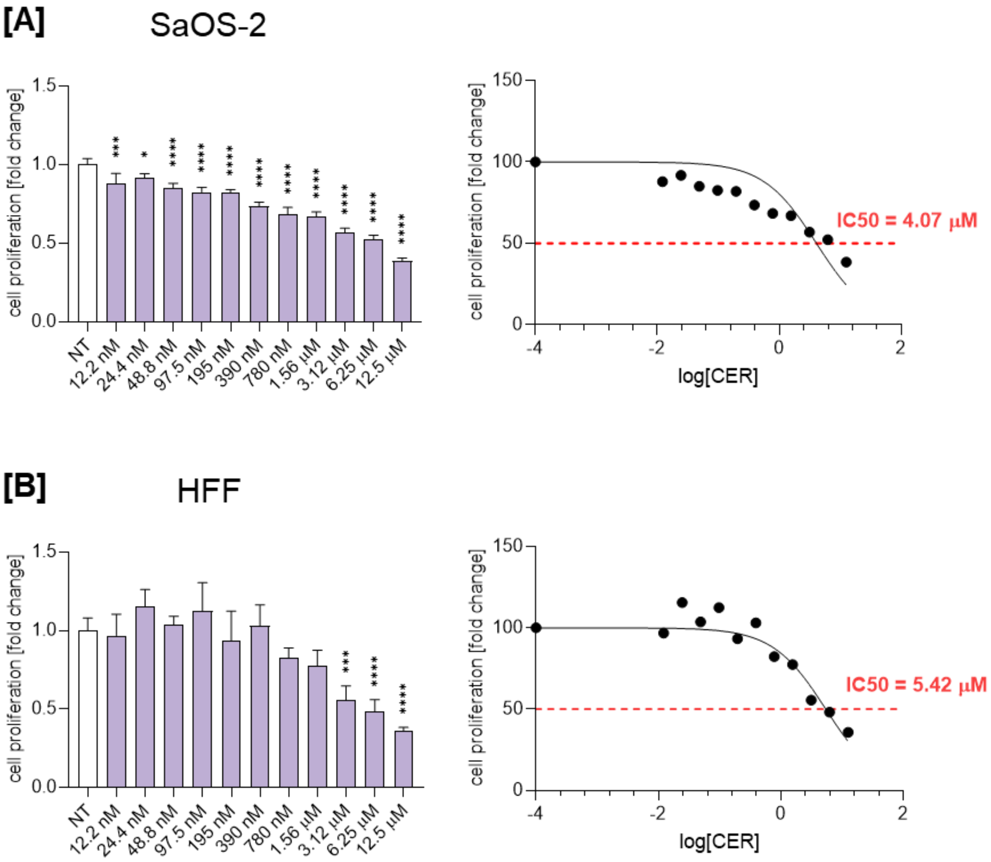

Figure 47. *Dose-response curves of SaOS-2 and HFF cell lines treated with increasing concentrations of Ceralasertib. The ALT+ SaOS-2 control line showed a dose-dependent response but with a relatively high IC50 (4.07 µM;* ***A****), while the ALT– HFF line exhibited a much more limited response (IC50 = 5.42 µM;* ***B****). Data are presented as mean ± standard deviation (SD). Statistical analysis was performed by comparing treated samples to the untreated control (NT); * $p \leq 0.05$; *** $p \leq 0.001$; **** $p \leq 0.0001$.*

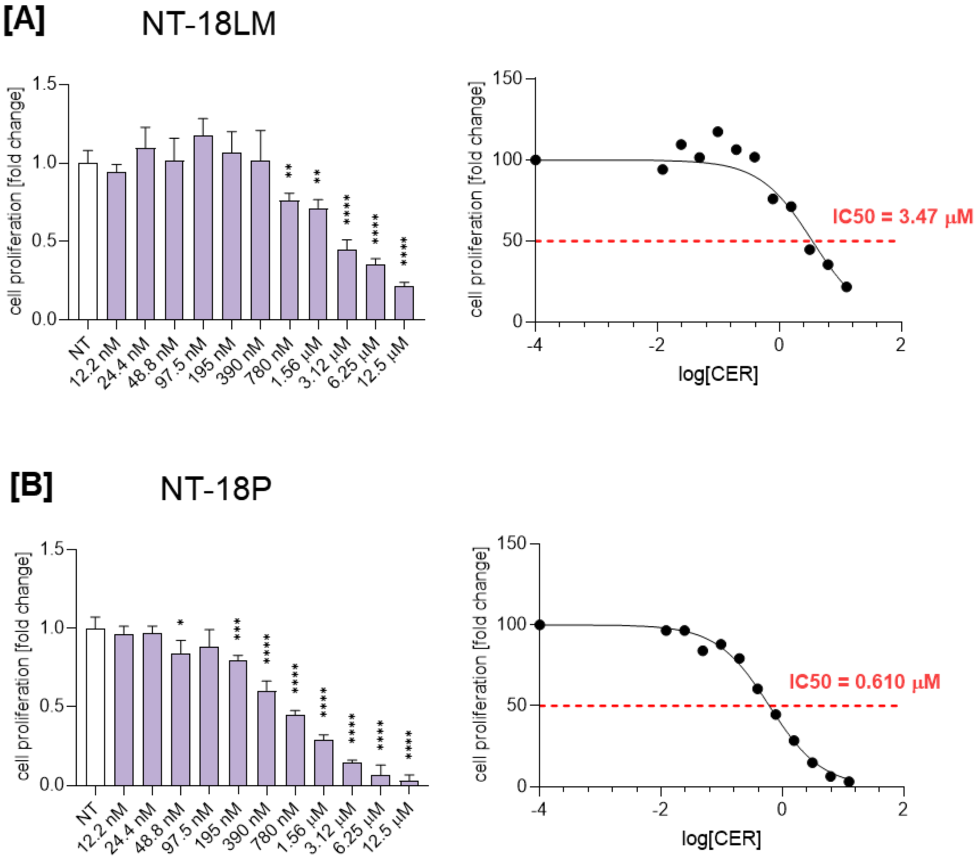

Figure 48. *Dose-response curves of NT-18LM, and NT-18P cell lines treated with increasing concentrations of Ceralasertib. The NT-18LM line responded significantly only at higher concentrations (IC50 = 3.47 µM;* ***A****), whereas the NT-18P line demonstrated the greatest efficacy among all models tested (IC50 = 0.61 µM;* ***B****). Data are presented as mean ± standard deviation (SD). Statistical analysis was performed by comparing treated samples to the untreated control (NT);* * $p \leq 0.05$; ** $p \leq 0.01$; *** $p \leq 0.001$; **** $p \leq 0.0001$.

These analyses allowed us to draw two important conclusions: first, that in our cellular models, the cytotoxic effect of Adavosertib is more pronounced compared to that of Ceralasertib; second, that the primary tumor cell line NT-18P appears to be more sensitive to treatment with both compounds than the metastatic NT-18LM line, suggesting the potential involvement of additional phenotypic features – beyond ALT activity – that may influence treatment response.

6. Discussion

Neuroendocrine tumors (NETs) continue to gain attention as an important clinical problem. Although they are relatively uncommon, their reported incidence has increased over the years. This rise likely reflects both improvements in diagnostic imaging and registry coding, as well as a potential true increase in tumor occurrence (Rogoza et al., 2022). NETs are highly heterogeneous: they can arise in many organs, show different levels of differentiation, and carry diverse molecular alterations (Cakir et al., 2010; Basu et al., 2010), which complicates the identification of reliable biological markers and the development of effective targeted therapies. Among NETs, pituitary NETs (PitNETs/pituitary adenomas) and pancreatic NETs (PanNETs) represent clinically relevant subsets (WHO, 2022; Rogoza et al., 2022), exemplifying the challenges associated with tumor heterogeneity and treatment stratification. Among the few established targets in NETs, somatostatin receptors (SSTRs) are especially important. Their frequent overexpression has allowed the development of somatostatin analogs (SSAs), used both for therapy and imaging (Rogoza et al., 2022; Eychenne et al., 2020). However, currently available SSAs still have clear limitations, such as dependence on specific SSTR subtypes and relevant side effects (for example, pasireotide-induced diabetes). This highlights the need for improved SSAs with better activity and fewer complications, which was the aim of the first part of this thesis.

NETs carry mutations in a variety of genes and some of these mutations are invariably associated with poor prognosis and aggressive tumor behavior. Among these are inactivating mutations in *ATRX* and *DAXX*, genes that encode two chromatin-remodeling factors functioning as a complex and playing a particularly critical role in the maintenance of telomeric structure and integrity (Clatterbuck Soper and Meltzer, 2023; Heaphy et al., 2011). Loss of function of either of these factors is associated with a cascade of molecular alterations linked to genomic instability and tumorigenesis. In particular, activation of the alternative lengthening of telomeres (ALT) mechanism represents one of the major consequences observed in this condition (Hou et al., 2022; van ´t Veld et al., 2025). Reliable biomarkers are required for the early diagnosis of these aggressive NETs and for the monitoring of the efficacy of currently available ALT-targeting therapies. This shortcoming was addressed by the second part of the thesis.

PART 1

The first aim of this thesis was to test five novel SSAs (SMTR-001 to SMTR-005) and compare them to octreotide and pasireotide. We specifically assessed their effect on important features of SSTR signaling, e.g., hormone secretion regulation and cell proliferation. Before testing the compounds, we confirmed the expression of SSTR2 and SSTR5 in our cell models (AtT-20 and NT-3). The results obtained by RT-qPCR and Western blot matched previous reports (Cervia et al., 2003; Benten et al., 2018), supporting the use of these lines as suitable NET models for SSA testing.

Antisecretory and Antiproliferative Effects in 2D Culture

Because functioning NETs release excessive amounts of hormones, assessing the ability of the compounds to reduce secretion was an essential first step. The reference SSAs behaved as expected: pasireotide was more effective in AtT-20 cells, and octreotide in NT-3 cells, in agreement with other studies (Gentilin et al., 2023; Bistika et al., 2024). Importantly, several of the new peptides performed very well. In AtT-20 cells, SMTR-001 and SMTR-004 reached antisecretory values close to those of pasireotide. In NT-3 cells, an even broader group of peptides (SMTR-001, -002, -004, and -005) achieved reductions in hormone secretion similar to, or higher, than the reference compounds.

These findings show that many of the new peptides have strong antisecretory properties, although their efficacy depends on the specific NET model, reflecting the known variability in SSTR expression and signaling. It should be noted that secretion levels were not normalized to cell number or viability, as no reliable normalization method could be established; consequently, potential changes in cell viability during the assay may have influenced the measured hormone release, representing a possible confounding factor.

SSAs are also valued for their ability to slow tumor growth, as shown in clinical and preclinical studies (Sidéris et al., 2012; Merola et al., 2017). WST-1 measurements were used to assess cell metabolic activity, and reductions in WST-1 signal are interpreted cautiously as being consistent with decreased cell viability and/or proliferation. Our results confirmed the expected antiproliferative effects. In AtT-20 cells, SMTR-002, SMTR-003, and SMTR-004 showed effects equal to or greater than those of octreotide and pasireotide, even at low concentrations. In NT-3 cells, all new peptides displayed activity similar to that of the reference drugs, and several of them performed better at lower doses.

Another notable point is that we did not always observe a clear concentration-dependent effect. This phenomenon has already been described for first-generation SSAs (Danila et al., 2001; Gunn et al., 2006; Dicitore et al., 2022), and likely depends on receptor internalization, saturation, or other cellular mechanisms.

Activity in 3D Spheroid Models

Because 3D cultures better reproduce tumor behavior than standard 2D models, we extended the analysis to spheroids, focusing on the lead compound SMTR-002 which was selected due to its equal and sub-nanomolar affinities at both SSTR2 and SSTR5, as well as its consistent inhibitory effects on hormone secretion and cell proliferation across the tested NET models. As widely reported (Lv et al., 2017; Hsieh et al., 2015;

Kapałczyńska et al., 2018), 3D systems were generally less sensitive to treatment. In AtT-20 spheroids, both reference SSAs showed only weak activity, and SMTR-002 did not significantly reduce ACTH secretion or proliferation. In NT-3 spheroids, SMTR-002 showed modest but detectable activity on both insulin secretion and proliferation, sometimes comparable to or slightly better than the reference drug.

Overall, the 3D results confirm that NET spheroids are more resistant to SSAs than 2D cultures, probably due to limited penetration of the drug into the spheroid and differences in cell-cell interactions and growth conditions. Under the tested conditions, AtT-20 spheroids showed limited responsiveness to SSAs, suggesting that further optimization such as adjustments to drug penetration, dosing schedule, spheroid size standardization, or receptor profiling in 3D may be required to fully assess their pharmacological effects.

Analysis of SSTR Signaling

In pituitary cells, the second messenger cyclic AMP (cAMP) represents the main factor involved in the regulation of hormone secretion (Ben-Shlomo et al., 2009). Its function is therefore crucial in the mechanisms of hormone hypersecretion observed in pituitary adenomas. Activation of SSTRs leads to negative regulation of adenylate cyclase (AC), resulting in a reduction of intracellular cAMP levels and inhibition of hormone secretion (Theodoropoulou and Stalla, 2013). Consequently, the ability to modulate intracellular cAMP levels represents a parameter of major importance for the pharmacological profiling of novel SSAs.

Thus, to further understand how the new compounds act at the signaling level, we measured intracellular cAMP levels in AtT-20 cells. As expected, octreotide and pasireotide strongly reduced forskolin-induced intracellular cAMP levels. Among the new compounds, SMTR-005 showed a particularly high ability to inhibit cAMP, while SMTR-002 also achieved strong reductions, even at low concentrations. These data confirm that the new peptides engage SSTR signaling pathways in a manner comparable to standard SSAs. The fact that different peptides performed differently across assays suggests that they may interact with SSTR subtypes in specific ways, which could be useful in designing improved SSAs in the future.

PART 2

The second objective of this study was to optimize methods to detect molecular markers associated with aggressive NET behavior that may have diagnostic or therapeutic relevance. Activation of the ALT mechanism is a well-established hallmark of progressive and malignant PanNETs and is strongly associated with inactivating mutations in *DAXX* or *ATRX* (Singhi et al., 2017; Kim et al., 2017; Konukiewitz et al., 2021). Based on these findings, we focused on this marker. We selected two PanNET cell models, NT-18P and NT-18LM, both carrying a *DAXX* mutation, to investigate DNA C-circles as a specific molecular marker of ALT+ tumors. SaOS-2 and HFF cell lines were included as ALT-positive and ALT-negative controls, respectively.

Genomic DNA extracted from cell pellets was analyzed using rolling-circle amplification (RCA) followed by qPCR. Both PanNET models showed strong C-circle amplification, with Ct values lower than those observed in the ALT-positive control SaOS-2. Quantitative analysis confirmed high C-circle levels in NT-18P and NT-18LM cells, further supported by agarose gel visualization of the PCR products. Since C-circles can be released into the extracellular space via exosomes (Chen et al., 2021), we also analyzed total cell-free DNA extracted from culture supernatants. Consistent with intracellular data, high levels of C-circles were detected in the supernatants of both PanNET models, exceeding those of SaOS-2. Low-level amplification in the ALT-negative HFF control likely reflects technical background signals or DNA released during cell death. Overall, these findings confirm that both PanNET models display robust ALT activity and are suitable for studying ALT-associated tumor behavior. Thus, these cells represent a good model to optimize the detection of C-circles from extracellular vesicles obtained from the cell supernatant, a necessary step before moving to advanced *in vitro* models (e.g., patient-derived organoids) and ultimately patients' plasma.

We next evaluated the sensitivity of these models to pharmacological agents targeting ALT-positive tumors. Cells were treated with Adavosertib (WEE1 inhibitor) and Ceralasertib (ATR inhibitor), both currently under clinical investigation (Foote et al., 2018; Zhang et al., 2024). NT-18P cells were highly sensitive to both compounds, showing low IC50 values and marked reductions in cell viability, exceeding the response observed in the ALT-positive SaOS-2 control. In contrast, NT-18LM cells were more resistant, with higher IC50 values and response patterns closer to those of the ALT-negative HFF line. For both PanNET models, Adavosertib was more effective than Ceralasertib at lower concentrations.

These results indicate that, although both PanNET cell lines share ALT activity, they differ in their response to ALT-targeted treatments. The increased resistance observed in the metastatic-derived NT-18LM cells suggests that factors beyond ALT status, possibly related to tumor progression or adaptation, contribute to treatment response and should be considered when developing targeted therapeutic strategies for aggressive PanNETs.

POTENTIAL RELATIONSHIP BETWEEN ALT STATUS AND SOMATOSTATIN RECEPTOR–TARGETED THERAPIES IN NETs

ALT-positive PanNETs are frequently associated with *ATRX* or *DAXX* mutations, which define a subset of tumors characterized by aggressive clinical behavior and poor prognosis. Given the marked biological heterogeneity of NETs and the variability in SSTR expression across tumor subtypes, it is conceivable that ALT-positive tumors may display distinct SSTR expression patterns compared to ALT-negative counterparts, potentially influencing their responsiveness to somatostatin analogs or peptide receptor radionuclide therapy (PRRT). Notably, Mapelli et al. reported that quantitative parameters derived from [^{68}Ga]-DOTATOC PET imaging, reflecting somatostatin receptor expression, were associated with *ATRX/DAXX* status in PanNETs, suggesting a possible link between molecular alterations involved in telomere maintenance and receptor-targeted imaging phenotypes (Mapelli et al., 2023).

Although this study did not directly investigate the association between ALT status and SSTR expression, the hypothesis that ALT-positive PanNETs may differ in their sensitivity to receptor-targeted therapies represents a relevant area for future research. In particular, evaluating whether *ATRX/DAXX* mutations and ALT activation correlate with specific SSTR subtype profiles or with differential response to SSAs and PRRT could provide clinically meaningful insights. The integration of molecular characterization of telomere maintenance mechanisms with pharmacological profiling may contribute to a more stratified therapeutic approach in aggressive PanNETs, improving patient selection and treatment outcomes.
In this context, the two lines of investigation presented in this thesis can be viewed as complementary strategies to address NET heterogeneity: on one side, the development of improved receptor-targeted pharmacological agents; on the other, the molecular stratification of aggressive tumors based on *ATRX/DAXX* alterations and ALT activation. Together, these approaches may contribute to a more precise selection of therapeutic options in NET patients.

CONCLUSIONS

Overall, the results of these studies successfully addressed the two main objectives of our work. First, the characterization of the novel SSAs demonstrated that several of them possess a favorable pharmacological profile, exerting significant antisecretory and antiproliferative effects in representative NET models and showing efficacy comparable to that of clinically used SSAs.
Second, the molecular analyses confirmed that the PanNET models NT-18P and NT-18LM exhibit ALT activity, validating their suitability for investigating this aggressive tumor phenotype. Their differential sensitivity to ALT-targeting treatments further underscores the presence of phenotypic features that may influence therapeutic response. Together, these findings meet the aims of the study and provide a solid foundation for future research aimed at optimizing SSA-based therapies and developing improved diagnostic and therapeutic strategies for aggressive NETs.

7. References

- 2022 WHO Classification of Endocrine and Neuroendocrine Tumors (Endocrine 5th Ed.).

- Ambrosini V, Zanoni L, Filice A, Lamberti G, Argalia G, Fortunati E, Campana D, Versari A, Fanti S. Radiolabeled Somatostatin Analogues for Diagnosis and Treatment of Neuroendocrine Tumors. Cancers (Basel). 2022 Feb 19;14(4):1055. doi: 10.3390/cancers14041055. PMID: 35205805; PMCID: PMC8870358.

- Amit M, Margulets V, Segev H, Shariki K, Laevsky I, Coleman R, Itskovitz-Eldor J. Human feeder layers for human embryonic stem cells. Biol Reprod. 2003 Jun;68(6):2150-6. doi: 10.1095/biolreprod.102.012583. Epub 2003 Jan 22. PMID: 12606388.

- Araya VA, Liberman C, Munizaga C, Pineda P, Barberán M, Cordero F, Lanas A, Toro L. Combination of High Prevalence Sign/Symptom Pairs: An Approach to the Diagnosis of Cushing’s Syndrome. IntechOpen. 2024. doi: 10.5772/intechopen.106521

- Asa SL, Ezzat S. The pathogenesis of pituitary tumors. Annu Rev Pathol. 2009;4:97-126. doi: 10.1146/annurev.pathol.4.110807.092259. PMID: 19400692.

- Bailey SM, Brenneman MA, Goodwin EH. Frequent recombination in telomeric DNA may extend the proliferative life of telomerase-negative cells. Nucleic Acids Res. 2004 Jul 16;32(12):3743-51. doi: 10.1093/nar/gkh691. PMID: 15258249; PMCID: PMC484178.

- Bakker WH, Krenning EP, Breeman WA, Kooij PP, Reubi JC, Koper JW, de Jong M, Laméris JS, Visser TJ, Lamberts SW. In vivo use of a radioiodinated somatostatin analogue: dynamics, metabolism, and binding to somatostatin receptor-positive tumors in man. J Nucl Med. 1991 Jun;32(6):1184-9. Erratum in: J Nucl Med 1991 Oct;32(10):1999. PMID: 1646302.

- Bakker WH, Krenning EP, Reubi JC, Breeman WA, Setyono-Han B, de Jong M, Kooij PP, Bruns C, van Hagen PM, Marbach P, et al. In vivo application of [111In-DTPA-D-Phe1]-octreotide for detection of somatostatin receptor-positive tumors in rats. Life Sci. 1991;49(22):1593-601. doi: 10.1016/0024-3205(91)90053-e. PMID: 1658516.

- Barbieri F, Bajetto A, Pattarozzi A, Gatti M, Würth R, Thellung S, Corsaro A, Villa V, Nizzari M, Florio T. Peptide receptor targeting in cancer: the somatostatin paradigm. Int J Pept. 2013;2013:926295. doi: 10.1155/2013/926295. Epub 2013 Feb 7. PMID: 23476673; PMCID: PMC3582104.

- Basu B, Sirohi B, Corrie P. Systemic therapy for neuroendocrine tumours of gastroenteropancreatic origin. Endocr Relat Cancer. 2010 Jan 29;17(1):R75-90. doi: 10.1677/ERC-09-0108. PMID: 20008097.

- Beck-Peccoz P, Giavoli C, Lania A. A 2019 update on TSH-secreting pituitary adenomas. J Endocrinol Invest. 2019 Dec;42(12):1401-1406. doi: 10.1007/s40618-019-01066-x. Epub 2019 Jun 7. PMID: 31175617.

- Ben-Shlomo A, Schmid H, Wawrowsky K, Pichurin O, Hubina E, Chesnokova V, Liu NA, Culler M, Melmed S. Differential Ligand-Mediated Pituitary Somatostatin Receptor Subtype Signaling: Implications for Corticotroph Tumor Therapy. Endocr Rev. 2009 Dec 1;30(7):933. doi: 10.1210/edrv.30.7.9983. PMID: 28199544.

- Benten D, Behrang Y, Unrau L, Weissmann V, Wolters-Eisfeld G, Burdak-Rothkamm S, Stahl FR, Anlauf M, Grabowski P, Möbs M, Dieckhoff J, Sipos B, Fahl M, Eggers C, Perez D, Bockhorn M, Izbicki JR, Lohse AW, Schrader J. Establishment of the First Well-differentiated Human Pancreatic Neuroendocrine Tumor Model. Mol Cancer Res. 2018 Mar;16(3):496-507. doi: 10.1158/1541-7786.MCR-17-0163. Epub 2018 Jan 12. PMID: 29330294.

- Bertagna X, Guignat L, Groussin L, Bertherat J. Cushing's disease. Best Pract Res Clin Endocrinol Metab. 2009 Oct;23(5):607-23. doi: 10.1016/j.beem.2009.06.001. PMID: 19945026.

- Bistika M, Marangelo A, Ascione F, Valentini N, Fedeli F, Schrader J, Modena D, Steinkühler C, Pellegata NS. The Novel SSTR3 Full Agonist ITF2984 Shows Antitumor Properties against Pancreatic Neuroendocrine Tumors. Neuroendocrinology. 2025;115(5):446-459. doi: 10.1159/000543136. Epub 2024 Dec 28. PMID: 39733775.

- Bodei L, Cremonesi M, Grana CM, Chinol M, Baio SM, Severi S, Paganelli G. Yttrium-labelled peptides for therapy of NET. Eur J Nucl Med Mol Imaging. 2012 Feb;39 Suppl 1:S93-102. doi: 10.1007/s00259-011-2002-y. PMID: 22388625.

- Buonassisi V, Sato G, Cohen AI. Hormone-producing cultures of adrenal and pituitary tumor origin. Proc Natl Acad Sci U S A. 1962 Jul 15;48(7):1184-90. doi: 10.1073/pnas.48.7.1184. PMID: 13874682; PMCID: PMC220930.

- Cakir M, Dworakowska D, Grossman A. Somatostatin receptor biology in neuroendocrine and pituitary tumours: part 1--molecular pathways. J Cell Mol Med. 2010 Nov;14(11):2570-84. doi: 10.1111/j.1582-4934.2010.01125.x. PMID: 20629989; PMCID: PMC4373477.

- Cakir M, Dworakowska D, Grossman A. Somatostatin receptor biology in neuroendocrine and pituitary tumours: part 2--clinical implications. J Cell Mol Med. 2010 Nov;14(11):2585-91. doi: 10.1111/j.1582-4934.2010.01125_1.x. PMID: 20629988; PMCID: PMC4373478.

- Castro PG, de León AM, Trancón JG, Martínez PA, Alvarez Pérez JA, Fernández Fernández JC, García Bernardo CM, Serra LB, González González JJ. Glucagonoma syndrome: a case report. J Med Case Rep. 2011 Aug 22;5:402. doi: 10.1186/1752-1947-5-402. PMID: 21859461; PMCID: PMC3171381.

- Cervia D, Nunn C, Fehlmann D, Langenegger D, Schuepbach E, Hoyer D. Pharmacological characterisation of native somatostatin receptors in AtT-20 mouse tumour corticotrophs. Br J Pharmacol. 2003 May;139(1):109-21. doi: 10.1038/sj.bjp.0705235. PMID: 12746229; PMCID: PMC1573832.

- Cesare AJ, Reddel RR. Alternative lengthening of telomeres: models, mechanisms and implications. Nat Rev Genet. 2010 May;11(5):319-30. doi: 10.1038/nrg2763. Epub 2010 Mar 30. PMID: 20351727.

- Cescato R, Schulz S, Waser B, Eltschinger V, Rivier JE, Wester HJ, Culler M, Ginj M, Liu Q, Schonbrunn A, Reubi JC. Internalization of sst2, sst3, and sst5 receptors: effects of somatostatin agonists and antagonists. J Nucl Med. 2006 Mar;47(3):502-11. PMID: 16513620.

- Chaidarun SS, Klibanski A. Gonadotropinomas. Semin Reprod Med. 2002 Nov;20(4):339-48. doi: 10.1055/s-2002-36708. PMID: 12536357.

- Chen YY, Dagg R, Zhang Y, Lee JHY, Lu R, Martin La Rotta N, Sampl S, Korkut-Demirbaş M, Holzmann K, Lau LMS, Reddel RR, Henson JD. The C-Circle Biomarker Is Secreted by Alternative-Lengthening-of-Telomeres Positive Cancer Cells inside Exosomes and Provides a Blood-Based

Diagnostic for ALT Activity. Cancers (Basel). 2021 Oct 26;13(21):5369. doi: 10.3390/cancers13215369. PMID: 34771533; PMCID: PMC8582556.

- Cho NW, Dilley RL, Lampson MA, Greenberg RA. Interchromosomal homology searches drive directional ALT telomere movement and synapsis. Cell. 2014 Sep 25;159(1):108-121. doi: 10.1016/j.cell.2014.08.030. PMID: 25259924; PMCID: PMC4177039.

- Clatterbuck Soper SF, Meltzer PS. ATRX/DAXX: Guarding the Genome against the Hazards of ALT. Genes (Basel). 2023 Mar 24;14(4):790. doi: 10.3390/genes14040790. PMID: 37107548; PMCID: PMC10137841.

- Claude E, Decottignies A. Telomere maintenance mechanisms in cancer: telomerase, ALT or lack thereof. Curr Opin Genet Dev. 2020 Feb;60:1-8. doi: 10.1016/j.gde.2020.01.002. Epub 2020 Feb 27. PMID: 32114293.

- Cleveland Clinic (2024). Neuroendocrine Tumors. Available on: https://my.clevelandclinic.org/health/diseases/22006-neuroendocrine-tumors-net.

- Clynes D, Jelinska C, Xella B, Ayyub H, Scott C, Mitson M, Taylor S, Higgs DR, Gibbons RJ. Suppression of the alternative lengthening of telomere pathway by the chromatin remodelling factor ATRX. Nat Commun. 2015 Jul 6;6:7538. doi: 10.1038/ncomms8538. PMID: 26143912; PMCID: PMC4501375.

- Danila DC, Haidar JN, Zhang X, Katznelson L, Culler MD, Klibanski A. Somatostatin receptor-specific analogs: effects on cell proliferation and growth hormone secretion in human somatotroph tumors. J Clin Endocrinol Metab. 2001 Jul;86(7):2976-81. doi: 10.1210/jcem.86.7.7620. PMID: 11443154.

- de Jong M, Breeman WA, Kwekkeboom DJ, Valkema R, Krenning EP. Tumor imaging and therapy using radiolabeled somatostatin analogues. Acc Chem Res. 2009 Jul 21;42(7):873-80. doi: 10.1021/ar800188e. PMID: 19445476.

- Dean FB, Nelson JR, Giesler TL, Lasken RS. Rapid amplification of plasmid and phage DNA using Phi 29 DNA polymerase and multiply-primed rolling circle amplification. Genome Res. 2001 Jun;11(6):1095-9. doi: 10.1101/gr.180501. PMID: 11381035; PMCID: PMC311129.

- Deng Y, Guo X, Ferguson DO, Chang S. Multiple roles for MRE11 at uncapped telomeres. Nature. 2009 Aug 13;460(7257):914-8. doi: 10.1038/nature08196. Epub 2009 Jul 26. PMID: 19633651; PMCID: PMC2760383.

- Dicitore A, Saronni D, Gaudenzi G, Carra S, Cantone MC, Borghi MO, Persani L, Vitale G. Long-term effects of somatostatin analogues in rat GH-secreting pituitary tumor cell lines. J Endocrinol Invest. 2022 Jan;45(1):29-41. doi: 10.1007/s40618-021-01609-1. Epub 2021 Jun 14. PMID: 34128215; PMCID: PMC8741688.

- Dilley RL, Greenberg RA. ALTernative Telomere Maintenance and Cancer. Trends Cancer. 2015 Oct 1;1(2):145-156. doi: 10.1016/j.trecan.2015.07.007. PMID: 26645051; PMCID: PMC4669901.

- Dilley RL, Verma P, Cho NW, Winters HD, Wondisford AR, Greenberg RA. Break-induced telomere synthesis underlies alternative telomere maintenance. Nature. 2016 Nov 3;539(7627):54-58. doi: 10.1038/nature20099. Epub 2016 Oct 19. PMID: 27760120; PMCID: PMC5384111.

- Dimitrova N, de Lange T. Cell cycle-dependent role of MRN at dysfunctional telomeres: ATM signaling-dependent induction of nonhomologous end joining (NHEJ) in G1 and resection-mediated inhibition of NHEJ in G2. Mol Cell Biol. 2009 Oct;29(20):5552-63. doi: 10.1128/MCB.00476-09. Epub 2009 Aug 10. PMID: 19667071; PMCID: PMC2756883.

- Durma AD, Saracyn M, Kołodziej M, Jóźwik-Plebanek K, Dmochowska B, Kapusta W, Żmudzki W, Mróz A, Kos-Kudła B, Kamiński G. Epidemiology of Neuroendocrine Neoplasms and Results of Their Treatment with [177Lu]Lu-DOTA-TATE or [177Lu]Lu-DOTA-TATE and [90Y]Y-DOTA-TATE-A Six-Year Experience in High-Reference Polish Neuroendocrine Neoplasm Center. Cancers (Basel). 2023 Nov 18;15(22):5466. doi: 10.3390/cancers15225466. PMID: 38001726; PMCID: PMC10670106.

- Eychenne R, Bouvry C, Bourgeois M, Loyer P, Benoist E, Lepareur N. Overview of Radiolabeled Somatostatin Analogs for Cancer Imaging and Therapy. Molecules. 2020 Sep 2;25(17):4012. doi: 10.3390/molecules25174012. PMID: 32887456; PMCID: PMC7504749.

- Ezzat S, Asa SL, Couldwell WT, Barr CE, Dodge WE, Vance ML, McCutcheon IE. The prevalence of pituitary adenomas: a systematic review.

Cancer. 2004 Aug 1;101(3):613-9. doi: 10.1002/cncr.20412. PMID: 15274075.

- Fan Q, Zhang F, Barrett B, Ren K, Andreassen PR. A role for monoubiquitinated FANCD2 at telomeres in ALT cells. Nucleic Acids Res. 2009 Apr;37(6):1740-54. doi: 10.1093/nar/gkn995. Epub 2009 Jan 7. PMID: 19129235; PMCID: PMC2665210.

- Fleseriu M, Langlois F, Lim DST, Varlamov EV, Melmed S. Acromegaly: pathogenesis, diagnosis, and management. Lancet Diabetes Endocrinol. 2022 Nov;10(11):804-826. doi: 10.1016/S2213-8587(22)00244-3. Epub 2022 Oct 6. PMID: 36209758.

- Fogh J, Fogh JM, Orfeo T. One hundred and twenty-seven cultured human tumor cell lines producing tumors in nude mice. J Natl Cancer Inst. 1977 Jul;59(1):221-6. doi: 10.1093/jnci/59.1.221. PMID: 327080.

- Foote KM, Nissink JWM, McGuire T, Turner P, Guichard S, Yates JWT, Lau A, Blades K, Heathcote D, Odedra R, Wilkinson G, Wilson Z, Wood CM, Jewsbury PJ. Discovery and Characterization of AZD6738, a Potent Inhibitor of Ataxia Telangiectasia Mutated and Rad3 Related (ATR) Kinase with Application as an Anticancer Agent. J Med Chem. 2018 Nov 21;61(22):9889-9907. doi: 10.1021/acs.jmedchem.8b01187. Epub 2018 Nov 10. PMID: 30346772.

- Forment JV, O'Connor MJ. Targeting the replication stress response in cancer. Pharmacol Ther. 2018 Aug;188:155-167. doi: 10.1016/j.pharmthera.2018.03.005. Epub 2018 Mar 24. PMID: 29580942.

- Forrer F, Uusijärvi H, Waldherr C, Cremonesi M, Bernhardt P, Mueller-Brand J, Maecke HR. A comparison of (111)In-DOTATOC and (111)In-DOTATATE: biodistribution and dosimetry in the same patients with metastatic neuroendocrine tumours. Eur J Nucl Med Mol Imaging. 2004 Sep;31(9):1257-62. doi: 10.1007/s00259-004-1553-6. Epub 2004 Jun 10. PMID: 15197500.

- Freda PU, Katznelson L, van der Lely AJ, Reyes CM, Zhao S, Rabinowitz D. Long-acting somatostatin analog therapy of acromegaly: a meta-analysis. J Clin Endocrinol Metab. 2005 Aug;90(8):4465-73. doi: 10.1210/jc.2005-0260. Epub 2005 May 10. PMID: 15886238.

- Gentilin E, Borges De Souza P, Ambrosio MR, Bondanelli M, Gagliardi I, Zatelli MC. Protein kinase C delta mediates Pasireotide effects in an ACTH-secreting pituitary tumor cell line. J Endocrinol Invest. 2023 Dec;46(12):2609-2616. doi: 10.1007/s40618-023-02117-0. Epub 2023 May 26. PMID: 37233978; PMCID: PMC10632222.

- Gomes-Porras M, Cárdenas-Salas J, Álvarez-Escolá C. Somatostatin Analogs in Clinical Practice: a Review. Int J Mol Sci. 2020 Feb 29;21(5):1682. doi: 10.3390/ijms21051682. PMID: 32121432; PMCID: PMC7084228.

- Greenman Y, Stern N. Non-functioning pituitary adenomas. Best Pract Res Clin Endocrinol Metab. 2009 Oct;23(5):625-38. doi: 10.1016/j.beem.2009.05.005. PMID: 19945027.

- Guan X, Huang S. Advances in the application of 3D tumor models in precision oncology and drug screening. Front Bioeng Biotechnol. 2022 Sep 28;10:1021966. doi: 10.3389/fbioe.2022.1021966. PMID: 36246388; PMCID: PMC9555934.

- Gunn SH, Schwimer JE, Cox M, Anthony CT, O'Dorisio MS, Woltering EA. In vitro modeling of the clinical interactions between octreotide and 111In-pentetreotide: is there evidence of somatostatin receptor downregulation? J Nucl Med. 2006 Feb;47(2):354-9. PMID: 16455643.

- Gupta N, Huang TT, Horibata S, Lee JM. Cell cycle checkpoints and beyond: Exploiting the ATR/CHK1/WEE1 pathway for the treatment of PARP inhibitor-resistant cancer. Pharmacol Res. 2022 Apr;178:106162. doi: 10.1016/j.phrs.2022.106162. Epub 2022 Mar 5. PMID: 35259479; PMCID: PMC9026671.

- Guterres AN, Villanueva J. Targeting telomerase for cancer therapy. Oncogene. 2020 Sep;39(36):5811-5824. doi: 10.1038/s41388-020-01405-w. Epub 2020 Jul 30. PMID: 32733068; PMCID: PMC7678952.

- Hanahan D, Weinberg RA. Hallmarks of cancer: the next generation. Cell. 2011 Mar 4;144(5):646-74. doi: 10.1016/j.cell.2011.02.013. PMID: 21376230.

- Heaphy CM, de Wilde RF, Jiao Y, Klein AP, Edil BH, Shi C, Bettegowda C, Rodriguez FJ, Eberhart CG, Hebbar S, Offerhaus GJ, McLendon R, Rasheed BA, He Y, Yan H, Bigner DD, Oba-Shinjo SM, Marie SK, Riggins GJ, Kinzler KW, Vogelstein B, Hruban RH, Maitra A, Papadopoulos N, Meeker AK. Altered telomeres in tumors with ATRX and DAXX mutations. Science. 2011 Jul 22;333(6041):425. doi: 10.1126/science.1207313. Epub 2011 Jun 30. PMID: 21719641; PMCID: PMC3174141.

- Henson JD, Cao Y, Huschtscha LI, Chang AC, Au AY, Pickett HA, Reddel RR. DNA C-circles are specific and quantifiable markers of alternative-lengthening-of-telomeres activity. Nat Biotechnol. 2009 Dec;27(12):1181-5. doi: 10.1038/nbt.1587. PMID: 19935656.

- Henson JD, Neumann AA, Yeager TR, Reddel RR. Alternative lengthening of telomeres in mammalian cells. Oncogene. 2002 Jan 21;21(4):598-610. doi: 10.1038/sj.onc.1205058. PMID: 11850785.

- Henson JD, Reddel RR. Assaying and investigating Alternative Lengthening of Telomeres activity in human cells and cancers. FEBS Lett. 2010 Sep 10;584(17):3800-11. doi: 10.1016/j.febslet.2010.06.009. Epub 2010 Jun 11. PMID: 20542034.

- Heppeler A, Froidevaux S, Eberle AN, Maecke HR. Receptor targeting for tumor localisation and therapy with radiopeptides. Curr Med Chem. 2000 Sep;7(9):971-94. doi: 10.2174/0929867003374516. PMID: 10911025.

- Holt EH, Lupsa B, Lee GS, Bassyouni H, Peery HE. Goodman's Basic Medical Endocrinology (Fifth Edition). Chapter 7 - The pancreatic islets. Elsevier. 2022;203-237. https://doi.org/10.1016/B978-0-12-815844-9.00007-5.

- Hou K, Yu Y, Li D, Zhang Y, Zhang K, Tong J, Yang K, Jia S. Alternative Lengthening of Telomeres and Mediated Telomere Synthesis. Cancers (Basel). 2022 Apr 27;14(9):2194. doi: 10.3390/cancers14092194. PMID: 35565323; PMCID: PMC9105334.

- Hsieh CH, Chen YD, Huang SF, Wang HM, Wu MH. The effect of primary cancer cell culture models on the results of drug chemosensitivity assays: the application of perfusion microbioreactor system as cell culture vessel. Biomed Res Int. 2015;2015:470283. doi: 10.1155/2015/470283. Epub 2015 Jan 14. PMID: 25654105; PMCID: PMC4310262.

- Jiang WQ, Zhong ZH, Henson JD, Neumann AA, Chang AC, Reddel RR. Suppression of alternative lengthening of telomeres by Sp100-mediated sequestration of the MRE11/RAD50/NBS1 complex. Mol Cell Biol. 2005

Apr;25(7):2708-21. doi: 10.1128/MCB.25.7.2708-2721.2005. Erratum in: Mol Cell Biol. 2005 May;25(10):4334. PMID: 15767676; PMCID: PMC1061646.

- Jiao Y, Shi C, Edil BH, de Wilde RF, Klimstra DS, Maitra A, Schulick RD, Tang LH, Wolfgang CL, Choti MA, Velculescu VE, Diaz LA Jr, Vogelstein B, Kinzler KW, Hruban RH, Papadopoulos N. DAXX/ATRX, MEN1, and mTOR pathway genes are frequently altered in pancreatic neuroendocrine tumors. Science. 2011 Mar 4;331(6021):1199-203. doi: 10.1126/science.1200609. Epub 2011 Jan 20. PMID: 21252315; PMCID: PMC3144496.

- Kapałczyńska M, Kolenda T, Przybyła W, Zajączkowska M, Teresiak A, Filas V, Ibbs M, Bliźniak R, Łuczewski Ł, Lamperska K. 2D and 3D cell cultures - a comparison of different types of cancer cell cultures. Arch Med Sci. 2018 Jun;14(4):910-919. doi: 10.5114/aoms.2016.63743. Epub 2016 Nov 18. PMID: 30002710; PMCID: PMC6040128.

- Kim JY, Brosnan-Cashman JA, An S, Kim SJ, Song KB, Kim MS, Kim MJ, Hwang DW, Meeker AK, Yu E, Kim SC, Hruban RH, Heaphy CM, Hong SM. Alternative Lengthening of Telomeres in Primary Pancreatic Neuroendocrine Tumors Is Associated with Aggressive Clinical Behavior and Poor Survival. Clin Cancer Res. 2017 Mar 15;23(6):1598-1606. doi: 10.1158/1078-0432.CCR-16-1147. Epub 2016 Sep 23. PMID: 27663587; PMCID: PMC5354973.

- Konukiewitz B, Jesinghaus M, Kasajima A, Klöppel G. Neuroendocrine neoplasms of the pancreas: diagnosis and pitfalls. Virchows Arch. 2022 Feb;480(2):247-257. doi: 10.1007/s00428-021-03211-5. Epub 2021 Oct 13. PMID: 34647171; PMCID: PMC8986719.

- Kramara J, Osia B, Malkova A. Break-Induced Replication: The Where, The Why, and The How. Trends Genet. 2018 Jul;34(7):518-531. doi: 10.1016/j.tig.2018.04.002. Epub 2018 May 4. PMID: 29735283; PMCID: PMC6469874.

- Krejs GJ. VIPoma syndrome. Am J Med. 1987 May 29;82(5B):37-48. doi: 10.1016/0002-9343(87)90425-6. PMID: 3035922.

- Kulke MH, Benson AB 3rd, Bergsland E, Berlin JD, Blaszkowsky LS, Choti MA, Clark OH, Doherty GM, Eason J, Emerson L, Engstrom PF, Goldner WS, Heslin MJ, Kandeel F, Kunz PL, Kuvshinoff BW 2nd, Moley JF, Pillarisetty VG, Saltz L, Schteingart DE, Shah MH, Shibata S, Strosberg JR, Vauthey JN, White R, Yao JC, Freedman-Cass DA, Dwyer MA; National Comprehensive Cancer Networks. Neuroendocrine tumors. J Natl Compr Canc Netw. 2012 Jun 1;10(6):724-64. doi: 10.6004/jnccn.2012.0075. PMID: 22679117.

- Kunz PL, Reidy-Lagunes D, Anthony LB, Bertino EM, Brendtro K, Chan JA, Chen H, Jensen RT, Kim MK, Klimstra DS, Kulke MH, Liu EH, Metz DC, Phan AT, Sippel RS, Strosberg JR, Yao JC; North American Neuroendocrine Tumor Society. Consensus guidelines for the management and treatment of neuroendocrine tumors. Pancreas. 2013 May;42(4):557-77. doi: 10.1097/MPA.0b013e31828e34a4. PMID: 23591432; PMCID: PMC4304762.

- Kunz PL. Carcinoid and neuroendocrine tumors: building on success. J Clin Oncol. 2015 Jun 1;33(16):1855-63. doi: 10.1200/JCO.2014.60.2532. Epub 2015 Apr 27. PMID: 25918282.

- Lee JH, Paull TT. Activation and regulation of ATM kinase activity in response to DNA double-strand breaks. Oncogene. 2007 Dec 10;26(56):7741-8. doi: 10.1038/sj.onc.1210872. PMID: 18066086.

- Lee JJ, Lee J, Lee H. Alternative paths to telomere elongation. Semin Cell Dev Biol. 2021 May;113:88-96. doi: 10.1016/j.semcdb.2020.11.003. Epub 2020 Dec 5. PMID: 33293233.

- Lee M, Pellegata NS. Multiple endocrine neoplasia syndromes associated with mutation of p27. J Endocrinol Invest. 2013 Oct;36(9):781-7. doi: 10.3275/9021. Epub 2013 Jun 26. PMID: 23800691.

- Lonser RR, Nieman L, Oldfield EH. Cushing's disease: pathobiology, diagnosis, and management. J Neurosurg. 2017 Feb;126(2):404-417. doi: 10.3171/2016.1.JNS152119. Epub 2016 Apr 22. PMID: 27104844.

- Lovejoy CA, Takai K, Huh MS, Picketts DJ, de Lange T. ATRX affects the repair of telomeric DSBs by promoting cohesion and a DAXX-dependent activity. PLoS Biol. 2020 Jan 2;18(1):e3000594. doi: 10.1371/journal.pbio.3000594. PMID: 31895940; PMCID: PMC6959610.

- Lv D, Hu Z, Lu L, Lu H, Xu X. Three-dimensional cell culture: A powerful tool in tumor research and drug discovery. Oncol Lett. 2017 Dec;14(6):6999-

7010. doi: 10.3892/ol.2017.7134. Epub 2017 Oct 3. PMID: 29344128; PMCID: PMC5754907.

- Ma ZY, Gong YF, Zhuang HK, Zhou ZX, Huang SZ, Zou YP, Huang BW, Sun ZH, Zhang CZ, Tang YQ, Hou BH. Pancreatic neuroendocrine tumors: A review of serum biomarkers, staging, and management. World J Gastroenterol. 2020 May 21;26(19):2305-2322. doi: 10.3748/wjg.v26.i19.2305. PMID: 32476795; PMCID: PMC7243647.

- MacKenzie D Jr, Watters AK, To JT, Young MW, Muratori J, Wilkoff MH, Abraham RG, Plummer MM, Zhang D. ALT Positivity in Human Cancers: Prevalence and Clinical Insights. Cancers (Basel). 2021 May 14;13(10):2384. doi: 10.3390/cancers13102384. PMID: 34069193; PMCID: PMC8156225.

- Mapelli P, Bezzi C, Muffatti F, Ghezzo S, Baldassi F, Schiavo Lena M, Andreasi V, Canevari C, Magnani P, De Cobelli F, Gianolli L, Partelli S, Falconi M, Picchio M. Somatostatin receptor activity assessed by 68Ga-DOTATOC PET can preoperatively predict DAXX/ATRX loss of expression in well-differentiated pancreatic neuroendocrine tumors. Eur J Nucl Med Mol Imaging. 2023 Jul;50(9):2818-2829. doi: 10.1007/s00259-023-06210-7. Epub 2023 Apr 3. PMID: 37010579.

- Melmed S. Acromegaly pathogenesis and treatment. J Clin Invest. 2009 Nov;119(11):3189-202. doi: 10.1172/JCI39375. Epub 2009 Nov 2. PMID: 19884662; PMCID: PMC2769196.

- Merola E, Panzuto F, Delle Fave G. Antiproliferative effect of somatostatin analogs in advanced gastro-entero-pancreatic neuroendocrine tumors: a systematic review and meta-analysis. Oncotarget. 2017 Jul 11;8(28):46624-46634. doi: 10.18632/oncotarget.16686. PMID: 28402955; PMCID: PMC5542298.

- Milewska-Kranc A, Ćwikła JB, Kolasinska-Ćwikła A. The Role of Receptor-Ligand Interaction in Somatostatin Signaling Pathways: Implications for Neuroendocrine Tumors. Cancers (Basel). 2023 Dec 25;16(1):116. doi: 10.3390/cancers16010116. PMID: 38201544; PMCID: PMC10778465.

- Muoio D, Laspata N, Fouquerel E. Functions of ADP-ribose transferases in the maintenance of telomere integrity. Cell Mol Life Sci. 2022 Mar 29;79(4):215. doi: 10.1007/s00018-022-04235-z. PMID: 35348914; PMCID: PMC8964661.

- Nabetani A, Ishikawa F. Unusual telomeric DNAs in human telomerase-negative immortalized cells. Mol Cell Biol. 2009 Feb;29(3):703-13. doi: 10.1128/MCB.00603-08. Epub 2008 Nov 17. PMID: 19015236; PMCID: PMC2630689.

- Ohmoto A, Rokutan H, Yachida S. Pancreatic Neuroendocrine Neoplasms: Basic Biology, Current Treatment Strategies and Prospects for the Future. Int J Mol Sci. 2017 Jan 13;18(1):143. doi: 10.3390/ijms18010143. PMID: 28098761; PMCID: PMC5297776.

- Oronsky B, Ma PC, Morgensztern D, Carter CA. Nothing But NET: A Review of Neuroendocrine Tumors and Carcinomas. Neoplasia. 2017 Dec;19(12):991-1002. doi: 10.1016/j.neo.2017.09.002. Epub 2017 Nov 5. PMID: 29091800; PMCID: PMC5678742.

- O'Sullivan RJ, Karlseder J. Telomeres: protecting chromosomes against genome instability. Nat Rev Mol Cell Biol. 2010 Mar;11(3):171-81. doi: 10.1038/nrm2848. Epub 2010 Feb 3. PMID: 20125188; PMCID: PMC2842081.

- Otte A, Herrmann R, Heppeler A, Behe M, Jermann E, Powell P, Maecke HR, Muller J. Yttrium-90 DOTATOC: first clinical results. Eur J Nucl Med. 1999 Nov;26(11):1439-47. PMID: 10552085.

- Potts PR, Yu H. The SMC5/6 complex maintains telomere length in ALT cancer cells through SUMOylation of telomere-binding proteins. Nat Struct Mol Biol. 2007 Jul;14(7):581-90. doi: 10.1038/nsmb1259. Epub 2007 Jun 24. PMID: 17589526.

- Potts PR. The Yin and Yang of the MMS21-SMC5/6 SUMO ligase complex in homologous recombination. DNA Repair (Amst). 2009 Apr 5;8(4):499-506. doi: 10.1016/j.dnarep.2009.01.009. Epub 2009 Feb 13. PMID: 19217832.

- Poullot AG, Chevalier N. New options in the treatment of Cushing’s disease: a focus on pasireotide. Research and Reports in Endocrine Disorders. 2013;3:31–38. https://doi.org/10.2147/RRED.S30972

- Robinson NJ, Schiemann WP. Amplification and Quantitation of Telomeric Extrachromosomal Circles. Bio Protoc. 2023 Mar 5;13(5):e4627. doi: 10.21769/BioProtoc.4627. PMID: 36908640; PMCID: PMC9993076.

- Rogoza O, Megnis K, Kudrjavceva M, Gerina-Berzina A, Rovite V. Role of Somatostatin Signalling in Neuroendocrine Tumours. Int J Mol Sci. 2022 Jan 27;23(3):1447. doi: 10.3390/ijms23031447. PMID: 35163374; PMCID: PMC8836266.

- Saharia A, Stewart SA. FEN1 contributes to telomere stability in ALT-positive tumor cells. Oncogene. 2009 Feb 26;28(8):1162-7. doi: 10.1038/onc.2008.458. Epub 2009 Jan 12. PMID: 19137021.

- Shay JW, Wright WE. Telomerase: a target for cancer therapeutics. Cancer Cell. 2002 Oct;2(4):257-65. doi: 10.1016/s1535-6108(02)00159-9. PMID: 12398889.

- Shen LP, Rutter WJ. Sequence of the human somatostatin I gene. Science. 1984 Apr 13;224(4645):168-71. doi: 10.1126/science.6142531. PMID: 6142531.

- Sidéris L, Dubé P, Rinke A. Antitumor effects of somatostatin analogs in neuroendocrine tumors. Oncologist. 2012;17(6):747-55. doi: 10.1634/theoncologist.2011-0458. Epub 2012 May 24. PMID: 22628056; PMCID: PMC3380872.

- Singhi AD, Liu TC, Roncaioli JL, Cao D, Zeh HJ, Zureikat AH, Tsung A, Marsh JW, Lee KK, Hogg ME, Bahary N, Brand RE, McGrath KM, Slivka A, Cressman KL, Fuhrer K, O'Sullivan RJ. Alternative Lengthening of Telomeres and Loss of DAXX/ATRX Expression Predicts Metastatic Disease and Poor Survival in Patients with Pancreatic Neuroendocrine Tumors. Clin Cancer Res. 2017 Jan 15;23(2):600-609. doi: 10.1158/1078-0432.CCR-16-1113. Epub 2016 Jul 12. PMID: 27407094; PMCID: PMC6560642.

- Sobinoff AP, Pickett HA. Alternative Lengthening of Telomeres: DNA Repair Pathways Converge. Trends Genet. 2017 Dec;33(12):921-932. doi: 10.1016/j.tig.2017.09.003. Epub 2017 Sep 29. PMID: 28969871.

- Soga J, Yakuwa Y. Somatostatinoma/inhibitory syndrome: a statistical evaluation of 173 reported cases as compared to other pancreatic endocrinomas. J Exp Clin Cancer Res. 1999 Mar;18(1):13-22. PMID: 10374671.

- Solari D, Pivonello R, Caggiano C, Guadagno E, Chiaramonte C, Miccoli G, Cavallo LM, Del Basso De Caro M, Colao A, Cappabianca P. Pituitary Adenomas: What Are the Key Features? What Are the Current Treatments? Where Is the Future Taking Us? World Neurosurg. 2019 Jul;127:695-709. doi: 10.1016/j.wneu.2019.03.049. PMID: 31266132.

- Theodoropoulou M, Stalla GK. Somatostatin receptors: from signaling to clinical practice. Front Neuroendocrinol. 2013 Aug;34(3):228-52. doi: 10.1016/j.yfrne.2013.07.005. Epub 2013 Jul 18. PMID: 23872332.

- Uccelli L, Martini P, Cittanti C, Carnevale A, Missiroli L, Giganti M, Bartolomei M, Boschi A. Therapeutic Radiometals: Worldwide Scientific Literature Trend Analysis (2008⁻2018). Molecules. 2019 Feb 12;24(3):640. doi: 10.3390/molecules24030640. Erratum in: Molecules. 2019 Apr 03;24(7):E1308. doi: 10.3390/molecules24071308. PMID: 30759753; PMCID: PMC6385165.

- van T Veld BR, Hackeng WM, Luchini C, Brosens LAA, Dreijerink KMA. Clinical Relevance of ATRX/DAXX Gene Mutations and ALT in Functioning Pancreatic Neuroendocrine Tumors. Endocr Pathol. 2025 Feb 15;36(1):3. doi: 10.1007/s12022-025-09848-1. PMID: 39954168; PMCID: PMC11829919.

- Veenstra MJ, de Herder WW, Feelders RA, Hofland LJ. Targeting the somatostatin receptor in pituitary and neuroendocrine tumors. Expert Opin Ther Targets. 2013 Nov;17(11):1329-43. doi: 10.1517/14728222.2013.830711. Epub 2013 Aug 31. PMID: 23991721.

- Verdun RE, Crabbe L, Haggblom C, Karlseder J. Functional human telomeres are recognized as DNA damage in G2 of the cell cycle. Mol Cell. 2005 Nov 23;20(4):551-61. doi: 10.1016/j.molcel.2005.09.024. PMID: 16307919.

- Viol F, Sipos B, Fahl M, Clauditz TS, Amin T, Kriegs M, Nieser M, Izbicki JR, Huber S, Lohse AW, Schrader J. Novel preclinical gastroenteropancreatic neuroendocrine neoplasia models demonstrate the feasibility of mutation-based targeted therapy. Cell Oncol (Dordr). 2022 Dec;45(6):1401-1419. doi: 10.1007/s13402-022-00727-z. Epub 2022 Oct 21. PMID: 36269546; PMCID: PMC9747820.

- Virgolini I, Patri P, Novotny C, Traub T, Leimer M, Füger B, Li SR, Angelberger P, Raderer M, Wogritsch S, Kurtaran A, Kletter K, Dudczak R.

Comparative somatostatin receptor scintigraphy using in-111-DOTA-lanreotide and in-111-DOTA-Tyr3-octreotide versus F-18-FDG-PET for evaluation of somatostatin receptor-mediated radionuclide therapy. Ann Oncol. 2001;12 Suppl 2:S41-5. doi: 10.1093/annonc/12.suppl_2.s41. PMID: 11762351.

- Wild D, Schmitt JS, Ginj M, Mäcke HR, Bernard BF, Krenning E, De Jong M, Wenger S, Reubi JC. DOTA-NOC, a high-affinity ligand of somatostatin receptor subtypes 2, 3 and 5 for labelling with various radiometals. Eur J Nucl Med Mol Imaging. 2003 Oct;30(10):1338-47. doi: 10.1007/s00259-003-1255-5. Epub 2003 Aug 21. PMID: 12937948.

- Wildemberg LE, Fialho C, Gadelha MR. Prolactinomas. Presse Med. 2021 Dec;50(4):104080. doi: 10.1016/j.lpm.2021.104080. Epub 2021 Oct 21. PMID: 34687915.

- Wolf P, Winhofer Y, Smajis S, Anderwald CH, Scheuba C, Niederle B, Gessl A, Luger A, Krebs M, Koperek O. Clinical presentation in insulinoma predicts histopathological tumour characteristics. Clin Endocrinol (Oxf). 2015 Jul;83(1):67-71. doi: 10.1111/cen.12777. Epub 2015 Apr 16. PMID: 25817061.

- Yang RH, Chu YK. Zollinger-Ellison syndrome: Revelation of the gastrinoma triangle. Radiol Case Rep. 2015 Dec 3;10(1):827. doi: 10.2484/rcr.v10i1.827. PMID: 27408649; PMCID: PMC4921170.

- Yao JC, Hassan M, Phan A, Dagohoy C, Leary C, Mares JE, Abdalla EK, Fleming JB, Vauthey JN, Rashid A, Evans DB. One hundred years after "carcinoid": epidemiology of and prognostic factors for neuroendocrine tumors in 35,825 cases in the United States. J Clin Oncol. 2008 Jun 20;26(18):3063-72. doi: 10.1200/JCO.2007.15.4377. PMID: 18565894.

- Zellinger B, Akimcheva S, Puizina J, Schirato M, Riha K. Ku suppresses formation of telomeric circles and alternative telomere lengthening in Arabidopsis. Mol Cell. 2007 Jul 6;27(1):163-9. doi: 10.1016/j.molcel.2007.05.025. PMID: 17612498.

- Zeng S, Xiang T, Pandita TK, Gonzalez-Suarez I, Gonzalo S, Harris CC, Yang Q. Telomere recombination requires the MUS81 endonuclease. Nat Cell Biol. 2009 May;11(5):616-23. doi: 10.1038/ncb1867. Epub 2009 Apr 12. PMID: 19363487; PMCID: PMC2675667.

- Zhang C, Peng K, Liu Q, Huang Q, Liu T. Adavosertib and beyond: Biomarkers, drug combination and toxicity of WEE1 inhibitors. Crit Rev Oncol Hematol. 2024 Jan;193:104233. doi: 10.1016/j.critrevonc.2023.104233. Epub 2023 Dec 14. PMID: 38103761.

- Zhang JM, Yadav T, Ouyang J, Lan L, Zou L. Alternative Lengthening of Telomeres through Two Distinct Break-Induced Replication Pathways. Cell Rep. 2019 Jan 22;26(4):955-968.e3. doi: 10.1016/j.celrep.2018.12.102. PMID: 30673617; PMCID: PMC6366628.

- Zhong ZH, Jiang WQ, Cesare AJ, Neumann AA, Wadhwa R, Reddel RR. Disruption of telomere maintenance by depletion of the MRE11/RAD50/NBS1 complex in cells that use alternative lengthening of telomeres. J Biol Chem. 2007 Oct 5;282(40):29314-22. doi: 10.1074/jbc.M701413200. Epub 2007 Aug 9. PMID: 17693401.

- Zhu XD, Küster B, Mann M, Petrini JH, de Lange T. Cell-cycle-regulated association of RAD50/MRE11/NBS1 with TRF2 and human telomeres. Nat Genet. 2000 Jul;25(3):347-52. doi: 10.1038/77139. PMID: 10888888.

List of Original Manuscripts

- Bistika M, Marangelo A, Ascione F, Valentini N, **Fedeli F**, Schrader J, Modena D, Steinkühler C, Pellegata NS. The Novel SSTR3 Full Agonist ITF2984 Shows Antitumor Properties against Pancreatic Neuroendocrine Tumors. Neuroendocrinology. 2025;115(5):446-459. doi: 10.1159/000543136. Epub 2024 Dec 28. PMID: 39733775. *PDF of this paper is included.*

- **Fedeli F**, Pellegata NS. MEN4: l'ultima e meno nota sindrome MEN. L'Endocrinologo. 2025;26:370-372. https://doi.org/10.1007/s40619-025-01630-z. *PDF of this paper is included.*

- **Fedeli F***, Bistika M*, Ascione F, Marangelo A, Guzzi FL, Schrader J, Harris AG, Pellegata NS. Anti-Secretory and Anti-Proliferative Actions of Next-Generation Dual Subtype 2 and 5 Somatostatin Receptor Ligands in Neuroendocrine Tumor Models. *In revision in Frontiers in Oncology. *Contributed equally.*

Acknowledgements

I would like to express my deepest gratitude to my supervisor, Professor Natalia Simona Pellegata, for her rigorous guidance, constant support, and for being an invaluable source of scientific expertise and intellectual inspiration throughout the course of my research.

I wish to acknowledge my friends and colleagues from the Human and Cancer Genetics research laboratory of the University of Pavia for their constant support and for being invaluable companions throughout this academic journey.

Finally, I would like to express my heartfelt gratitude to my family for their constant encouragement, unwavering support, and for always expressing unconditional trust in me.